Immune consequences and therapeutic targeting of disrupted mRNA splicing in cancer

Emma J. De Neef

A dissertation

submitted in partial fulfillment of the

requirements for the degree of

Doctor of Philosophy

University of Washington

2022

Reading Committee:

Robert K. Bradley, Chair

Evan Newell

Judit Villén

Program Authorized to Offer Degree:

Genome Sciences

University of Washington

Abstract

Immune consequences and therapeutic targeting of disrupted RNA splicing in cancer

Emma J. De Neef

Chair of the Supervisory Committee:
Robert K. Bradley
Department of Genome Sciences

Immunotherapies, such as checkpoint blockade, CAR-T cells, and vaccines, have proven to be a valuable tool to treat various types of cancer. This class of therapy capitalizes on the immune system's natural ability to recognize foreign antigens and kill cancer cells. Typically, many of these therapies have focused on the changes to DNA, particularly point mutations, that mark cancer cells. However, RNA dysregulation is also a frequent characteristic of cancer, and these transcriptomic changes may provide a large repertoire of new targets that previously has not been well studied. In this thesis, I address the question of whether RNA splicing changes can be immunogenic by studying disrupted splicing arising from 1) pharmacologic manipulation and 2) recurrent driver mutations in splicing factors. I demonstrate that drugs targeting splicing machinery can elicit anti-tumor immune responses dependent on splicing-derived neoantigens,

and that checkpoint blockade can be used in combination with these drugs to further improve immune response and tumor clearance. I further provide a framework for identifying splicing-derived neoepitopes and use this framework to identify potential immune targets in splicing factor-mutant cancers. I then use mass cytometry-based approaches with leukemic *SF3B1*-mutant patient samples to characterize the immune environment in *SF3B1*-mutant cancers and search for antigen-specific T cells that recognize and respond to splicing-derived neoantigens.

TABLE OF CONTENTS

LIST OF FIGURES

LIST OF TABLES

ACKNOWLEDGEMENTS

I would not have been able to complete this dissertation without the support of many people. Rob Bradley has been a kind and patient advisor and remained unwaveringly optimistic through all challenges, and I appreciate his support as I've learned an entirely new field. I've been very lucky to meet many people in the Bradley lab during my time here: Guo-Liang Chew, Jake Polaski, Joey Pangallo, Mao Pineda, Austin Gabel, James Thomas, Khrystyna North, Dylan Udy, Emma Hoppe, Andrea Belleville, Siegen McKellar, Taylor Nicholas, Toshi Banjo, Erik Kimble, and Edie Crosse have all been wonderful lab-mates and friends. This lab is full of brilliant and kind scientists, and I've very much enjoyed learning and drinking coffee and running with you all. I've also been in the unusually fortunate position to be able to work closely with a second lab, and I'd like to thank Evan Newell for being very gracious in allowing me to spend time learning immunology methods from him and his lab. The entire Newell lab, in particular Nandita Kumar, Heeju Ryu, Amy Codd, Laura Islas, and Tony Chour, have been so generous with their time, expertise, and friendship, and I've learned so much from getting to work with them. The remaining members of my committee, Judit Villén and Stephen Tapscott, the Fred Hutch and Genome Sciences administrative and core facilities teams, UW Science Explorers, my grad school cohort, and many other students, postdocs, professors, and staff have been essential to my experience and development here, and I would not have been able to complete this dissertation without them.

I owe a special shoutout to Cindy Yeh, Maddy Moore, Lexi Greenwood, Mao Pineda, and my soccer team, especially the Enchantments crew, for making Seattle feel like home. My friends across the country have also been amazingly supportive, no matter the time or distance. Amanda Lytle has ridden all the rollercoasters with me, and I'm very grateful for her friendship.

I'd also like to thank my family: my parents, Gaby and Wim; my siblings, Erica, Vincent, and Kasie; and my extended family have all been a wonderful source of comfort and encouragement, despite the physical distance. I truly appreciate their patience and steadfast support through whatever new things I decide to try. Thanks for always checking in on whether my cells are alive.

Like many other families, cancer has taken its toll on ours. In memory of my Bobonne and Pépé, Josée Scheers and Jozef Heirman, and my tante Christine Heirman. And to my tante Myriam, who is currently fighting the good fight with the help of immunotherapies.

Chapter 1. INTRODUCTION

Alternative mRNA splicing plays an important role in diversifying the proteome, but dysregulation of this process has been implicated in many diseases, including muscular dystrophy, cystic fibrosis, and cancer (Scotti & Swanson 2015). In cancer in particular, extensive dysregulation of the transcriptome is seen across many different types of cancer. The widespread failure to remove introns, known as intron retention, is seen in most cancer types (Dvinge & Bradley, 2015). Splicing factors such as SF3B1 are recurrently mutated in many cancers, including myelodysplastic syndromes, uveal melanomas, and breast cancer (Yoshida et al., 2011). These mutations alter the binding preferences and function of splicing factors, and result in the mis-splicing of hundreds of transcripts. Splicing alterations or failures often change protein sequences, which can impact the function or regulation of a protein. An outstanding question at the onset of this work, however, was whether these novel protein sequences were also able to trigger an extracellular immune response.

The adaptive immune system is responsible for the recognition of foreign invaders. In particular, cytotoxic T cells have a high diversity of antigen-binding molecules called T cell receptors (TCRs) capable of recognizing foreign antigens bound to a cell's major histocompatibility complex (MHC) proteins and killing the cells that present these threats. This response is crucial to our response to viral and bacterial antigens, and it is also a key regulator of cancer development. As cells accumulate mutations and become cancerous, the increased dissimilarity to healthy cells elevates the likelihood of introducing neoantigens and triggering an immune response. As a result, cancers must develop mechanisms of immune evasion. The crucial and dynamic nature of cancer-immune interactions has led to the development of many

immunotherapeutics that aim to strengthen a body's immune response to overcome evasive adaptions and kill the cancer. Immunotherapies can be general, such as checkpoint blockade, which blocks T cell inhibitory signals to improve their function and effectiveness, or specific, such as engineered chimeric antigen receptor (CAR) and TCR T cell therapies and peptide-based vaccines, which increase an immune response to a particular target antigen (Oiseth & Aziz, 2017, Zhang & Zhang, 2020). While these approaches vary, they all require an understanding of the immune repertoire. Typically, the search for cancer-specific neoantigens has been primarily focused on point mutation-based neoantigens. The novel protein sequences introduced by mis-splicing in cancer, however, represent an exciting pool of new targets due the public, recurrent nature of splicing changes in many patients across different types of cancer. As they also introduce entire stretches of new sequence, rather than single base-pair changes, they would also represent a significant expansion of potential targets. Here, I address the question of whether splicing changes can trigger an immune response and serve as targets to enhance immunotherapies. In Chapter 2, I show that pharmacologically disrupting splicing enhances the effectiveness of checkpoint blockade therapy in a MHC and T cell-dependent manner, work that establishes mis-splicing as a source of neoantigens. In ongoing work described in Chapter 3, I identify candidate neoantigens arising from recurrent splicing changes caused by mutations of the splicing factor SF3B1 and establish a framework to characterize genotype-dependent changes on the immune phenotype. Together, this work studies the effects of both drug-induced and endogenous mis-splicing on the immune system and highlights the clinical potential of targeting splicing dysregulation using immunotherapies.

Chapter 2. PHARMACOLOGIC MODULATION OF RNA SPLICING ENHANCES ANTI-TUMOR IMMUNITY

This research was originally published in *Cell.* Lu, S.X.*, De Neef, E.*, Thomas, J.D.*, Sabio, E., Rousseau, B., Gigoux, M., Knorr, D.A., Greenbaum, B., Elhanati, Y., Hogg, S.J., Chow, A., Ghosh, A., Xie, A., Zmarin, D., Cui, D., Erickson, C., Singer, M., Cho, H., Wang, E., Lu, B., Durham, B.H., Shah, H., Chowell, D., Gabel, A.M., Shen, Y., Liu, J., Jin, J., Rhodes, M.C., Taylor, R.E., Molina, H., Wolchok, J.D., Merghoub, T., Diaz Jr., L.A., Abdel-Wahab, O., Bradley, R.K. Pharmacologic modulation of RNA splicing enhances anti-tumor immunity. Cell 2021. 184:15 4032-4047.
*co-first authors

2.1 SUMMARY

Although mutations in DNA are the best-studied source of neoantigens that determine response to immune checkpoint blockade, alterations in RNA splicing within cancer cells could similarly result in neoepitope production. However, the endogenous antigenicity and clinical potential of such splicing-derived epitopes have not been tested. Here, we demonstrate that pharmacologic modulation of splicing via specific drug classes generates bona fide neoantigens and elicits anti-tumor immunity, augmenting checkpoint immunotherapy. Splicing modulation inhibited tumor growth and enhanced checkpoint blockade in a manner dependent on host T cells and peptides presented on tumor MHC class I. Splicing modulation induced stereotyped splicing changes across tumor types, altering the MHC I-bound immunopeptidome to yield splicing-derived neoepitopes that trigger an anti-tumor T cell response *in vivo*. These data definitively identify splicing modulation as an untapped source of immunogenic peptides and provide a means to enhance response to checkpoint blockade that is readily translatable to the clinic.

2.2 INTRODUCTION

Immune checkpoint blockade has greatly improved outcomes for several malignancies that are challenging to treat. Therapeutic benefit is associated with increased mutational burden (Marabelle et al., 2020;Sha et al., 2020) and mismatch repair deficiency (Le et al., 2017), commonly attributed to high tumor neoantigen load. Coding mutation-derived neoantigens are best studied, but neoantigens can also arise from other processes, such as altered RNA splicing. Two studies analyzing The Cancer Genome Atlas (TCGA) RNA sequencing (RNA-seq) data concluded that tumor-specific alternative splicing is abundant and may generate peptides that contribute to epitope repertoires (Jayasinghe et al., 2018;Kahles et al., 2018). Another study demonstrated that peptides

translated from retained introns arising from incomplete RNA splicing can be presented by MHC I in cancer cell lines (Smart et al., 2018). These provided proof-of-concept that splicing-derived peptides may serve as neoepitopes. However, whether splicing-derived neoepitopes elicit an endogenous immune response remains unknown, in part due to the inherent complexity of RNA processing and corresponding challenges with robustly identifying candidate splicing-derived neoantigens.

Determining whether splicing alterations can generate bona fide neoantigens is particularly important given the development of multiple clinical-grade compounds that alter RNA splicing via non-overlapping mechanisms. Many compounds, such as pladienolide B, GEX1A, E7107, and H3B-8800, inhibit the SF3b splicing complex's interactions with RNA (Lee et al., 2016;Seiler et al., 2018;Sellin et al., 2019;Yokoi et al., 2011). Recently, a series of "anti-cancer sulfonamides," including indisulam and E7820, were found to degrade the accessory splicing factor RBM39 by rendering it a neosubstrate for the Ddb1/CUL4 E3 ubiquitin ligase (Han et al., 2017). Additionally, blocking post-translational modifications of splicing factors, which are required for spliceosome assembly and effective splicing catalysis, can robustly perturb splicing. For example, RNA splicing factors are the most heavily arginine-methylated proteins (Musiani et al., 2019), thus, drugs that block asymmetric or symmetric arginine dimethylation by inhibiting type I or II protein arginine methyltransferases (PRMTs) potently perturb splicing (Fedoriw et al., 2019;Fong et al., 2019).

Here, we address the central question of whether altered RNA splicing generates immunologically meaningful neoantigens to provoke an effective anti-tumor immune response.

2.3 RESULTS

2.3.1 *Pharmacologic perturbation of splicing suppresses tumor growth* in vivo *in a manner dependent on host T cells and tumoral MHC I-presented peptides*

We hypothesized that pharmacologic splicing modulation might generate aberrant mRNAs encoding novel proteins, a subset of which could be translated and presented by MHC I as neoepitopes that provoke anti-tumor immunity. We first tested this by treating cancer cell lines with the RBM39-degrader indisulam at doses sub-inhibitory for growth (Figure 1A). This yielded graded RBM39 degradation but little effect on growth (Figures 1B, S1A, and S1B). Across cell lines, *ex vivo* treatment and drug washout yielded sustained suppression of RBM39 protein following drug removal, with minimal effects on subsequent proliferation or apoptosis (Figures 1C, 1D, S1C, and S1D). Drug treatment also did not notably change MHC I/II, PD-L1, cytokine, or death receptor expression (Figures S1E and S1F). In contrast, identical cells exhibited strikingly durable growth inhibition following engraftment into mice, despite transient drug exposure (Figures 1E, 1F, and S1G). The effect was dose dependent, with increasing drug concentrations causing increased splicing alterations (Figures S1H–S1K), reduced tumor growth (Figures S1L–S1N), and improved survival (Figure S1O).

The discrepancy between *in vitro* and *in vivo* growth suggested non-tumor cell-autonomous effects. To assess whether splicing alterations stimulated an anti-cancer immune response, we repeated our experiments but engrafted treated B16-F10 cells into Rag2-deficient C57BL/6 mice and, separately, into mice with T or natural killer (NK) cell depletion (Figure 1G). *In vivo* tumor growth inhibition was rescued in lymphocyte-deficient Rag2 recipients and by T cell depletion, but not NK depletion, suggesting a T cell and antigen-dependent mechanism (Figures 1H, 1I, and S1P–S1Y).

To test whether MHC I-bound antigens and $CD8^+$ T cells could be responsible, we evaluated the effects of indisulam versus DMSO pretreatment of isogenic B16-F10 cells with or without CRISPR-mediated knockout (KO) of *B2m*, encoding β_2-microglobulin (Figures 1J and 1K). *B2m* KO rescued the growth inhibition induced by indisulam pretreatment (Figure 1L). Overall, these results indicate that RBM39 degradation impairs cancer growth in a manner dependent on T cells and tumor MHC I expression.

We similarly observed immune-mediated suppression of tumor growth for MS-023, a splicing modulator that inhibits type I PRMT enzymes (Eram et al., 2016). *Ex vivo* MC38 treatment with MS-023 concentrations subinhibitory for *in vitro* growth resulted in globally reduced asymmetric dimethyl arginines (ADMA), but minimal effects on cell growth *in vitro* after drug washout (Figures 2A and S2A). However, identically treated cells yielded durable suppression of tumor growth in C57BL/6 mice (Figures 2B and 2C). These data suggest that splicing modulation can suppress tumor growth *in vivo* across multiple tumor types and mechanisms of splicing perturbation.

We next tested whether splicing modulation enhanced tumor immune recognition via drug-induced neoantigen production. To explore this, we compared the ability of professional antigen-presenting cells (APCs) loaded with lysates from control versus drug-treated tumors to stimulate naive, syngeneic T cells (Figure S2B). MC38 cells were treated with DMSO, indisulam, or MS-023 and used to generate lysates containing potentially immunogenic peptides, but no drug or viable tumor cells. Bone marrow-derived dendritic cells (BMDCs) from wild-type C57BL/6 or *B2m* knockout mice were pulsed with lysates and incubated with $CD45.1^+$ splenic T cells. BMDCs loaded with lysates from cells treated with indisulam or MS-023 more strongly promoted $CD8^+$ T

cell proliferation than did control BMDCs (Figures 2D and 2E). This effect was not observed with *B2m* KO BMDCs, indicating that MHC I peptide presentation was required.

2.3.2 *Drug-specific effects of splicing modulators on T cells*

Our initial studies did not address *in vivo* splicing modulator treatment, which can affect immune and hematopoietic compartments as well as tumors. To address this, we evaluated the effects of multiple classes of splicing modulators on T cell function: indisulam, MS-023, pladienolide B, GEX1A, and the PRMT5 inhibitor EPZ015666 (Chan-Penebre et al., 2015). We first assessed the effects of these drugs on the proliferation of CFSE-labeled, naive splenic T cells upon anti-CD3 and CD8 stimulation (Figure S2C). With 3 days of exposure, indisulam and the PRMT inhibitors had minimal effects on proliferation (IC_{50} ~1–10 μM), whereas pladienolide B and GEX1A were markedly inhibitory (IC_{50} of nMs) (Figures 2F, S2D, and S2E). Measurement of apoptosis and activation markers (Figure S2E) confirmed that these SF3b inhibitors were profoundly immunosuppressive.

We next assessed drug effects on T cell function. Indisulam and MS-023 minimally blunted the *in vitro* cytotoxicity of primed OT-1 T cells against ovalbumin (OVA)-expressing B16-F10 or MC38 cells (Figures 2G and S2F), with little impairment of cell killing at doses <4 μM. Exposure to higher drug concentrations did not inhibit OT-1 T cell secretion of interferon (IFN)-γ or tumor necrosis factor alpha (TNF-α) (Figures S2G and S2H) or degranulation (Figures S2I and S2J). We complemented these functional studies by determining the effects of each compound on gene expression in T cells activated with anti-CD3 and CD28 *ex vivo* (Figure S2K). Normally upregulated genes (Figure S2L) were markedly attenuated by pladienolide B, and to a lesser extent EPZ015666, whereas indisulam and MS-023 caused much milder changes (Figure S2M).

We then evaluated the effect of each drug on *in vivo* T cell function in response to antigen. Here, donor CD45.1$^+$ T cells were adoptively transferred into lethally irradiated recipients that were either syngeneic (C57BL/6), mismatched for non-MHC "minor" antigens (LP/J), or major MHC mismatched (BALB/c; H-2^b versus H-2^d) (Figure S2N) (Na et al., 2010). In BALB/c mice, donor T cells showed robust activation and proliferation in response to alloantigen (Figures 2H and S2O–S2Q). Although *in vivo* treatment with indisulam, MS-023, or EPZ015666 resulted in minimal impairment of T cell function (Figures S2P and S2Q), inhibition of both type I and II PRMTs blocked T cell proliferation (Figures 2H and 2I). Pladienolide B was similarly suppressive (Figures 2H, S2O, and S2R). These observations were recapitulated in the C56BL/6 → LP/J model (Figure 2I). Indisulam, MS-023, and EPZ015666 were permissive to the homeostatic expansion of T cells after syngeneic adoptive transfer (Figures S2R and S2S).

Last, we assessed the effects of splicing modulators on hematopoiesis in methylcellulose assays. Normal hematopoiesis was intact at even high μM doses of MS-023 and indisulam, whereas EPZ015666 suppressed hematopoiesis (Figure S2T). Pladienolide B suppressed hematopoiesis at nM concentrations (Figure S2T). These data indicate that select splicing modulators can be nontoxic at therapeutic concentrations in preclinical models.

2.3.3 *Modulating splicing enhances immune checkpoint blockade*

We next tested whether perturbing RNA splicing together with immune checkpoint blockade promoted control of established tumors. We evaluated *in vivo* RBM39 degradation alone or with anti-PD1 by engrafting C57BL/6 mice with syngeneic tumors and treated with splicing inhibitors starting on day 3 and anti-PD1 on day 7, the approximate date range at which tumors became measurable (Figure S3A). Simultaneous indisulam and anti-PD1 therapy led to significantly reduced growth of both B16-F10 and MC38 tumors, which exceeded the effects of either drug

alone (Figures 3A–3F and S3A) and yielded on-target RBM39 protein reduction (Figure 3B). We observed similar benefits in LLC tumors, which are resistant to anti-PD1 monotherapy (Bertrand et al., 2017;Lesterhuis et al., 2013) (Figures 3G and 3H).

We then evaluated MS-023 *in vivo*, finding that MS-023 treatment significantly improved response to anti-PD1 therapy (Figures 3I–3L). For mice engrafted with MC38 cells, combined MS-023 and anti-PD1 treatment resulted in 50% of mice alive and tumor-free 3 months after engraftment ($p < 0.001$) (Figure 3M). These survivors demonstrated immune memory: upon rechallenge 6 months later with MC38 cells (with or without MS-023 pretreatment *in vitro* before engraftment), they exhibited markedly improved tumor control compared to naive age-matched mice (Figures S3B–S3F).

Finally, we assessed potential toxicity in non-tumor tissues. Treatment with indisulam or MS-023 with or without anti-PD1 did not affect blood counts (Figure S4A). MC38 tumors exhibited increased $CD8^+$ T cells when indisulam or MS-023 was given with anti-PD1, consistent with intra-tumoral T cell expansion (Figure S4B). Drug-treated animals did not exhibit histologic inflammation or increased $CD8^+$ infiltrates in the skin, lung, gut, or liver (Figures S4C–S4F). Concordantly, RNA-seq analyses of lung, colon, and splenic T cells from indisulam-treated mice showed mild splicing changes (Figures S4G–S4K), and gene pathway analyses did not reveal an inflammatory signature (Figures S4L–S4O).

2.3.4 *Splicing modulators induce RNA isoforms encoding predicted neoepitopes*

We next determined the molecular mechanisms by which splicing modulation enhances anti-tumor immunity. We assessed how splicing modulation altered tumor cell transcriptomes in murine tumor cell lines treated with DMSO, indisulam, or MS-023, performed high-coverage RNA-seq, and quantified differential gene and isoform expression. Both drugs drove dramatic changes in

alternative and constitutive splicing, with differential cassette exon inclusion and constitutive intron retention the most common alterations (Figures 4A and S5A–S5C; Tables S1 and S2). Identical experiments in human tumor cell lines revealed similar changes (Figures 4B and S5D–S5F; Tables S3 and S4). A subset of mis-splicing events were consistently induced across all cell lines in a given species (Figures S5G–S5I), and 29.0% (indisulam) and 9.1% (MS-023) of mis-spliced genes were mis-spliced in both species (Figure S5J), consistent with conserved splicing mechanisms.

Indisulam and MS-023 gave rise to distinct downstream splicing alterations (Figure S5K). Indisulam-induced splicing alterations were dominated by reduced splicing efficiency: cassette exons were preferentially not included and constitutive introns were preferentially not excised (Figures 4C and 4D). MS-023, in contrast, resulted in more balanced changes (Figures S5C and S5F). Nonetheless, convergent mis-splicing between drugs was relatively common (~4%–8% of mis-spliced events) (Figures S5L and S5M). Constitutive introns preferentially retained following indisulam treatment were significantly depleted for poly(AT) (Figures 4E and 4F), consistent with RBM39 binding of poly(AT) motifs (Wang et al., 2019) and on-target RBM39 degradation. For MS-023, we observed no such obvious motif enrichment, as expected given the broad effects of type I PRMT inhibition.

We next evaluated the cytoplasmic availability of mis-spliced mRNAs for translation. Because splicing is linked to cytoplasmic mRNA export (Zhou et al., 2000), splicing alterations could fail to yield novel peptides. We separated nuclear and cytoplasmic RNA pools from DMSO- and indisulam-treated cells (focusing on indisulam because it led to global decreases in splicing efficiency) (Figure S5N) and quantified drug-induced isoforms in each subcellular compartment.

Indisulam-induced intron retention was readily apparent in the cytoplasmic fraction (Figures 4G, S5O, and S5P), where such mRNAs could be translated into potential neoepitopes (Figure 4H).

We finally estimated the potential consequences of indisulam-induced splicing alterations for neoepitope production. We enumerated all 8–14 amino acid sequences (8- to 14-mers) arising from mRNA isoforms in the transcriptome and estimated the binding affinity of each to common MHC I alleles with NetMHCPan. We restricted this list to predicted binders, then epitopes arising from differentially spliced genes, and finally epitopes from isoforms promoted by indisulam treatment. This filtering dramatically reduced the space of potential neoepitopes (Table S5), with most arising from cassette exons and constitutive introns (Figures 4I and 4J). Many predicted neoepitopes were shared within mouse (5,764) or human (24,378) cell lines (Figure S5Q), whereas fewer (1,763) were shared across species (Figure S5R), presumably reflecting non-conserved splicing alterations and differences in binding preferences of murine and human MHC.

2.3.5 *Drug-induced, splicing-derived neoepitopes are presented by MHC I on tumor cells*

We augmented transcriptomic analyses with experimental identification of splicing-derived neoepitopes. We purified H-2K^{b} and H-2D^{b} from DMSO versus indisulam-treated B16-F10 cells, eluted bound peptides, and performed liquid chromatography-tandem mass spectrometry (LC-MS/MS) (Figure 5A).

As MHC I-bound peptide identification from mass spectrometry depends critically upon the search database (proteome) (Murphy et al., 2017), we tested four distinct proteomes. These were "full-length" (i.e., all full-length protein sequences in the transcriptome) "predicted binders," restricted to 8- to 14-mers that were predicted MHC I binders; "predicted binders + spiked non-binders," augmented with decoy predicted non-binders; and "filtered predicted binders," restricted to predicted binders from differentially expressed or spliced genes (Figure 5B).

We first evaluated the full-length proteome. Approximately 80% and 86% of identified peptides were predicted binders for H-2D^b and H-2K^b versus 0.6% and 0.9% for peptides randomly sampled from the proteome (Figures 5C and S6A). Repeating this analysis with MHCflurry (O'Donnell et al., 2018) yielded similar results (not shown). Identified peptides had expected sequence preferences at anchor residues and preferential identification of 9-mers and 8- to 9-mers for H-2D^b and H-2K^b, respectively (Figures 5D, S6B, and S6C). We next varied the input proteome to maximize peptide identification. Restricting the search to predicted binders increased recovery ~2-fold relative to the full-length proteome, whereas further restricting to differentially expressed or spliced genes decreased recovery ~3.4-fold for H-2D^b (Figure 5E), with similar results for H-2K^b (Figure S6D). Restricting to predicted binders did not decrease specificity: we identified only 2 predicted non-binders, versus 2,204 predicted binders, across all six replicates when we queried the spiked non-binder proteome for H-2D^b (Figure 5F), again with similar results for H-2K^b (Figure S6E). Because the predicted binders proteome maximized yield while minimizing false-positives, we used it for subsequent analyses. The vast majority of identified peptides arose from genes expressed at moderate to high levels in B16-F10 cells (Figures 5G and S6F).

We identified 518 and 366 peptides for H-2D^b and H-2K^b that were only recovered from indisulam-treated samples (Figure 5H). We intersected these with predicted isoform-specific epitopes identified by RNA-seq (Figure 4J) to obtain 42 and 28 peptides that were bound by H-2D^b and H-2K^b, respectively, and arose from mRNA isoforms that were promoted by indisulam treatment (Figure 5I; Table S6). Due to the known limited sensitivity of mass spectrometry for the MHC I immunopeptidome (Schuster et al., 2018), we also nominated an additional 39 candidate peptides that were supported by RNA-seq alone, but predicted to be high-affinity binders to H-2D^b or H-2K^b (Figure S6G; Tables S1 and S2). We used this set of 109 (70 from mass spectrometry,

39 from RNA-seq) high-confidence, potentially antigenic peptides in subsequent functional assays.

2.3.6 *Splicing-derived neoantigens can trigger an endogenous T cell response*

We experimentally assessed binding of each of our 109 candidate neoantigenic peptides, which arose from diverse splicing changes (Figures 5I–5M), to H-2D^b or H-2K^b in the RMA-S stabilization assay (Figure S7A) (De Bruijn et al., 1991;De Silva et al., 1999). Candidate peptides had a range of abilities to stabilize H-2 molecules, with ~97% (68/70) of peptides identified from both MHC I mass spectrometry and RNA-seq exhibiting some binding, and several exhibiting very strong binding (Figures 5N–5Q, 6A , and S7B). Negative control "spike-in" peptides showed no binding.

Because MHC I binding is imperfectly correlated with immunogenicity, we experimentally tested each candidate. We immunized naive mice with each of the 109 peptides by hock injection, obtained draining lymph nodes (Figure 6B), and performed IFN-γ ELISpot with purified CD8$^+$ T cells incubated with naive, syngeneic splenocytes loaded with DMSO or cognate peptide (Table S7). ~43% (30/70) of peptides with both mass spectrometry and RNA-seq support elicited a CD8$^+$ T cell response (Figures 6C, 6D, and S7C), and several such peptides were induced by indisulam in all tested mouse cancer cell lines (Figure S6G). We further confirmed the specificity of these responses by immunizing across a range of peptide doses, revealing a dose-dependent CD8$^+$ T cell response (Figures 6E, S7D, and S7E).

All 39 candidate peptides selected based solely on RNA-seq analyses and MHC I binding predictions exhibited some H-2 binding (Figure S7F), and 28% (11/39) were immunogenic *in vivo* (Figure S7G). Our *in silico* analyses thereby identified a reasonable proportion of splicing-derived, potentially immunogenic peptides, but nonetheless a number of candidate peptides with verified

MHC I binding failed to elicit $CD8^+$ T cell activation *in vivo* (Figures S7H–S7J). To understand the basis for this differential response, we interrogated potential distinctions between immunogenic and nonimmunogenic splicing-derived peptides. Analyses of predicted binding affinity (NetMHCpan), experimental ability to stabilize MHC I (RMA-S assay), parent gene expression, type and magnitude of splicing alteration, and predicted induction of NMD revealed that only binding to MHC I (NetMHCpan or RMA-S assay) differed significantly between immunogenic and nonimmunogenic peptides (Figures 6F and 6G).

We next tested the ability of $CD8^+$ T cells from peptide-immunized mice to kill tumor cells presenting the cognate peptide. Although DMSO-immunized $CD8^+$ T cells exerted no cytotoxic activity regardless of the peptide presented, $CD8^+$ T cells from mice immunized with an immunogenic peptide selectively killed B16-F10 cells presenting that same peptide (Figures 7A and 7B).

Finally, we assessed the endogenous consequences of splicing-derived peptide production by testing whether drug-treated tumors generated neoantigenic peptides at concentrations that activated $CD8^+$ T cells. We repeated the above experiments, but used B16-F10 cells treated with indisulam as APCs (Figure 7C). This demonstrated that indisulam treatment of tumor cells indeed stimulates endogenous generation of specific splicing-derived neoantigens that trigger antigen-specific T cell activation (Figures 7D–7H). We therefore tested whether indisulam treatment drove the expansion of antigen-specific $CD8^+$ T cells that recognized neoantigenic peptides *in vivo* (Figure 7I). We generated H-$2K^b$ tetramers loaded with peptides that elicited strong IFN-γ secretion and cytotoxicity in the above experiments. These were used to stain tumor-draining lymph nodes of B16-F10 tumor-bearing mice treated with vehicle, indisulam, anti-PD1, or the combination (Figures 7J and S7K). This revealed increased frequencies of $CD8^+$ T cells capable

of recognizing splicing-derived peptides in mice receiving indisulam or the combination of indisulam and anti-PD1 (Figure 7K). Together, these data demonstrate that splicing modulation triggers the production of specific splicing-derived neoantigens at levels sufficient to drive expansion of $CD8^+$ T cells recognizing those antigens.

2.4 DISCUSSION

Mutation-derived neoantigen burden is an established determinant of response to immune checkpoint blockade. Here, we describe a distinct and abundant source of immunogenic peptides derived from novel mRNA species. We demonstrated that multiple clinical-grade compounds, acting via distinct mechanisms, can thereby enhance immune checkpoint blockade by inducing such MHC I-presented neopeptides. These studies thus identify a means to acutely and reversibly induce tumor neoantigens without genomic changes and demonstrate the antigenic potential of splicing-derived neoepitopes *in vivo*.

Splicing modulation generates many novel mRNAs derived from large-scale events, including inclusion of intronic sequence into mature mRNA, juxtaposition of exons not normally spliced together, and exons with abnormal 5′ or 3′ ends. Each can result in the production of peptides containing wholly novel sequences—confirmed by our cytoplasmic RNA sequencing and MHC I mass spectrometry—potentially contributing to the many immunogenic peptides that we identified.

Although direct comparisons of the frequencies of neoantigens derived from aberrant splicing to those derived from single-nucleotide variants is challenging due to differences in experimental methodologies, the frequency of antigenic peptides derived from splicing may be high. For example, of candidate neoantigenic peptides derived from intersecting RNA-seq and MHC I proteomics, we found that 30 of 70 (~43%) could elicit a $CD8^+$ T cell immune response in naive

C57BL/6 mice by IFN-γ ELISpot. Predicted neoantigenic peptides derived from RNA-seq alone exhibited a positivity rate of 11/39 (~28%). Of these neoantigenic peptides, we then demonstrated that four were associated with the expansion of antigen-specific $CD8^+$ T cells following splicing modulator treatment *in vivo*. In comparison, an early seminal study of MC38 cells reported that out of ~1,300 coding variations, ~13% resulted in peptides predicted to bind MHC I, 0.5% of which were identified by mass spectrometry and ~0.25% of which were immunogenic *in vivo* (Yadav et al., 2014). A recent consortium effort evaluating human melanoma and non-small cell lung cancer neoantigens predicted to bind MHC reported an immunogenicity rate of 6% (Wells et al., 2020). Overall, our results highlight the immunological relevance and clinical potential of splicing modulation.

2.4.1 *Limitations of the study*

Although we identified many splicing-derived, potentially immunogenic peptides produced upon exposure to splicing inhibitors, some of which triggered reactive T cell expansion *in vivo*, it is unclear which are most important for controlling tumor growth. However, because splicing modulation yields such diverse peptides, multiple peptides may contribute. Our work also highlights outstanding questions. For example, does splicing modulation affect $CD4^+$ T cells and MHC II-presented neoantigens? Are there MHC-independent anti-tumor B cell and antibody responses elicited by neoantigenic proteins on the cell surface? Do cancer-associated mutations in RNA splicing factors (Dvinge et al., 2016) alter the response to checkpoint immunotherapy? Finally, does pharmacologically altering RNA metabolic processes beyond splicing, such as intronic polyadenylation or NMD, affect tumor immunogenicity? Our finding that multiple modes of splicing modulation promote tumor immunogenicity will hopefully motivate further efforts to develop novel means of therapeutically modulating splicing and other RNA metabolic processes.

2.5 FIGURES

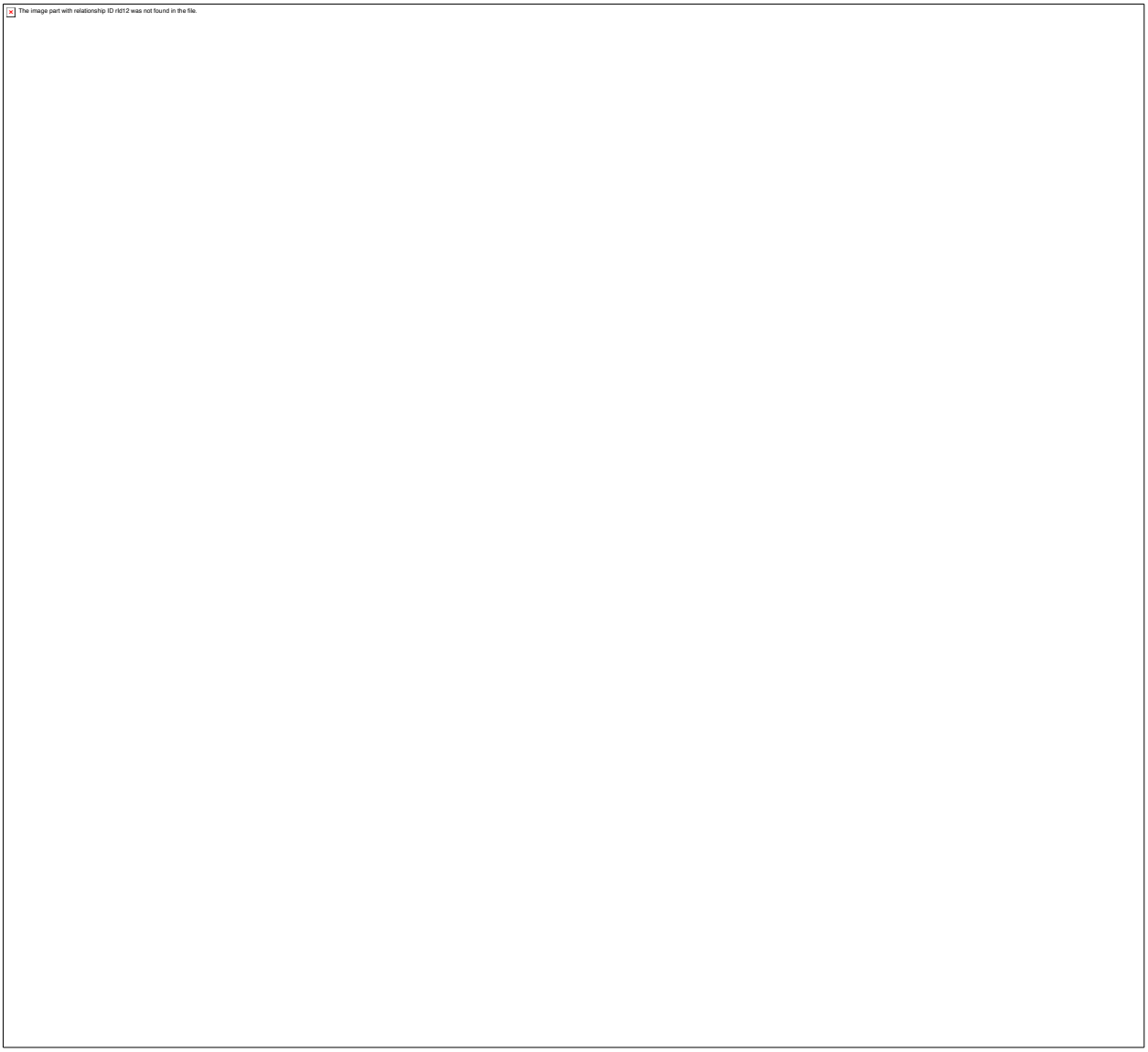

Figure 2.1. Pharmacologic RNA splicing modulation impairs tumor growth in a manner dependent on immune recognition.

(A) Schema of drug treatment and washout.

(B) Western blot of RBM39 in B16-F10 cells after 24 h of indisulam treatment. IC_{50}, half-maximal inhibitory concentration.

(C) As (B), but with 4 days of 1 μM indisulam, then drug washout and continued culture *in vitro*.

(D) Cell growth following 4 days of DMSO or indisulam 1 μM, and drug washout (day 0) *in vitro*. Mean ± SD.

(E) *In vivo* tumor volumes of cells from (D). Each line is an individual tumor (n = 10/group, tumors on both flanks).

(F) Box-and-whisker plots of tumor volumes from final day of measurement in (E). For box and whiskers plots throughout, bar indicates median, box edges first and third quartiles, and whiskers minimum and maximum. p from Wilcoxon rank-sum test.

(G) Schema of drug treatment and engraftment in mice with immune perturbations.

(H) Individual B16-F10 tumor volumes following DMSO or indisulam treatment and engraftment in mice with control versus T cell depletion. Each line is one tumor (n = 10/group).

(I) Tumor volumes from (H) at day 19; p from Wilcoxon rank-sum test: $^{***}p = 0.000379$; not significant (n.s.), $p > 0.05$.

(J) H-$2K^b$/D^b expression of control versus *B2m* KO B16-F10 cells ± IFN-γ.

(K) Schema to evaluate requirement of β_2M for tumor control *in vivo*.

(L) Individual tumor volumes at day 30 from (K); p from Wilcoxon rank-sum test: $^{***}p = 0.009$; n.s., $p > 0.05$.

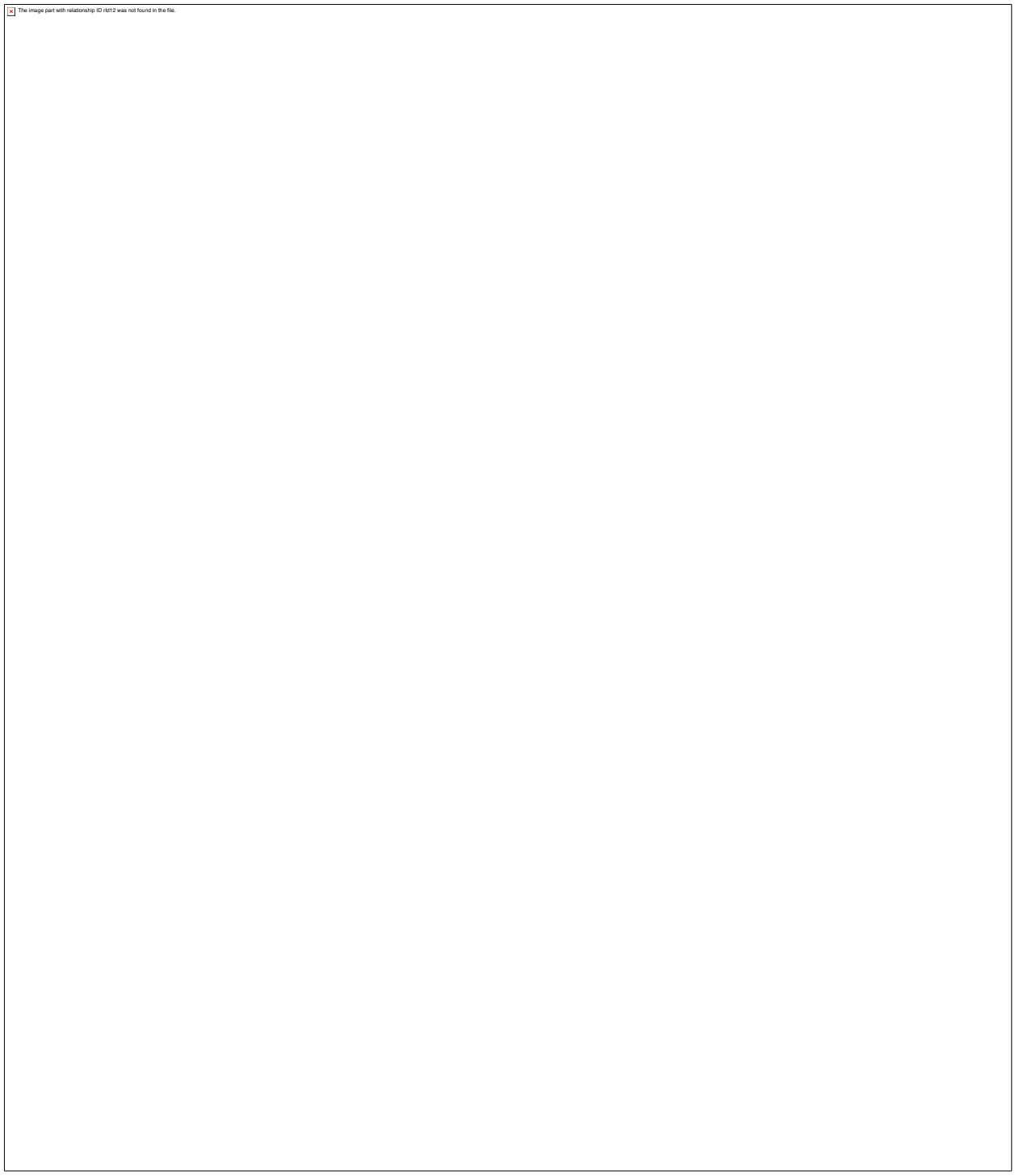

Figure 2.2. Pharmacologic splicing modulation promotes T cell reactivity without T cell toxicity *in vivo.*

(A) *In vitro* growth of MC38 cells following treatment with DMSO or MS-023 for 96 h and drug washout. Mean ± SD shown.

(B) *In vivo* growth of cells from (A) in C57BL/6 mice; individual tumor volumes shown (n = 10/group).

(C) Tumor volumes at day 21 from (B). p from Wilcoxon rank-sum test.

(D) Percentage of live donor $CD8^{+}CFSE^{lo}$ T cells on day 5 of a mixed leukocyte reaction with BMDC from wild-type or *B2m* KO C57BL/6 mice. Each dot is a technical replicate. Bar represents median. "No lysates": T cells cultured with BMDC and without lysate. p from Wilcoxon rank-sum test. For wild-type BMDCs, DMSO-versus-Ova p = 0.019, versus indisulam p = 0.001, versus MS-032 p = 0.032.

(E) Representative histograms of CFSE dilution from (D).

(F) CFSE-labeled naive splenic T cells from C57BL/6 mice stimulated with anti-CD3 and CD28 for 3 days.

(G) Wild-type or ovalbumin-expressing B16-F10 cells were cultured alone or with primed OT-1 T cells for 18 h and viable tumor cells enumerated.

(H) CFSE dilution of donor $CD45.1^{+}$ T cells adoptively transferred into irradiated BALB/c recipients treated with the indicated compounds. Donor splenic $CD4^{+}$ T cells on day 3.

(I) As (H), but in LP/J recipients; donor splenic T cells on day 5.

Figure 2.3. Splicing modulation enhances checkpoint immunotherapy.

(A) Treatment schema.

(B) Western blot of RBM39 in B16-F10 and immune organs of mice treated with vehicle versus indisulam for 10 days.

(C) B16-F10 tumor volumes in mice treated with vehicle, indisulam, anti-PD1, or both (n = 10/group). Mean ± SEM. Termination of line before day 28 indicates all animals had reached endpoints.

(D) Data from (C) at day 26; p from Wilcoxon rank-sum test versus PBS; *p = 0.002; **p = 0.000581. p indisulam versus ± PD1 = 0.004.

(E) As (C), but for MC38 tumor-bearing mice (n = 10/group).

(F) Data from (E) at day 31; p as above. *p = 0.004; **p = 0.0000682; ***p = 0.000000101. p indisulam versus ± PD1 = 0.04.

(G) As (C), but for LLC tumor-bearing mice (n = 10/group).

(H) Data from (G) at day 26. p as above. *p = 0.048; **p = 0.004. p indisulam versus ± PD1 = 0.125.

(I) Tumor volumes of B16-F10 tumor-bearing mice treated with vehicle, MS-023, anti-PD1, or both (n = 10/group). Mean ± SEM.

(J) Data from (I) at day 28; p as above. *p = 0.023; **p = 0.013; ***p = 0.0000153. p MS-023 versus ± PD1 = 0.056.

(K) As (I), but for MC38 tumor-bearing mice.

(L) Data from (I) at day 31; p as above. *p = 0.001; **p = 0.000342; ***p = 0.00000821. p MS-023 versus ± PD1 = 0.101.

(M) Kaplan-Meier survival from (I). All survivors past day 60 were tumor-free. p from log-rank test versus vehicle.

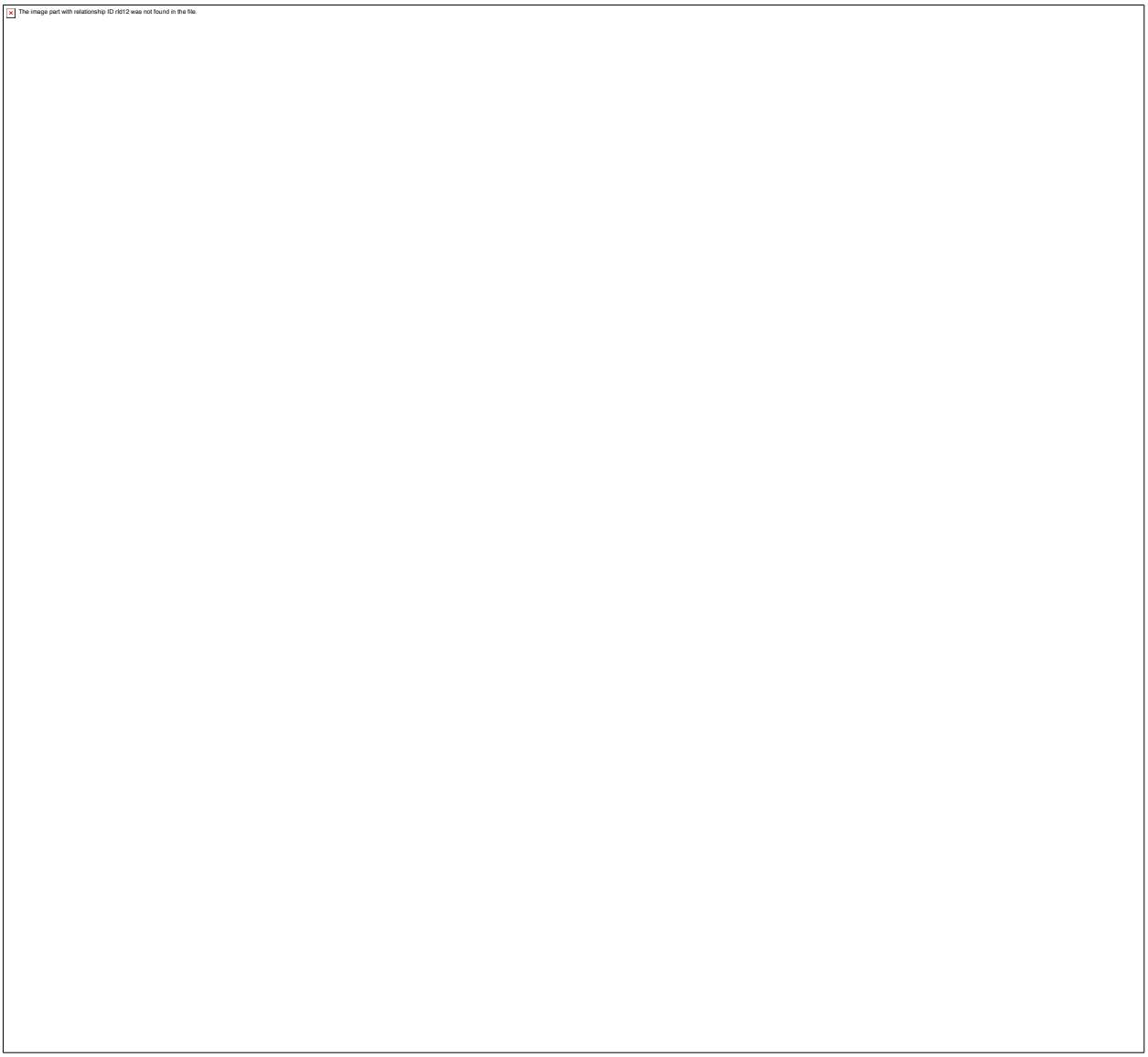

Figure 2.4. Splicing modulation induces widespread potential neoepitope production.

(A and B) RNA-seq read coverage illustrating shared intron retention (left), cassette exon exclusion (middle), and competing 3′ splice site selection (right) induced by indisulam in mouse (A) and human cancer cell lines (B). Conditions as in Figure 1A.

(C) Left: stacked bar graph illustrating numbers of differentially retained introns following indisulam treatment. Blue/green, increased/decreased intron retention in indisulam versus DMSO;

percentages shown for blue. Right: heatmap illustrating quantitative extent of intron retention for introns significantly mis-spliced in at least one sample.

(D) As (C), but for cassette exons.

(E) Bar graph of poly(AT) motif enrichment in introns preferentially retained versus unaffected upon indisulam treatment. Motif enrichment computed relative to a randomly selected group of unaffected introns. Error bars, 95% confidence intervals estimated by bootstrapping.

(F) Metagene plot of poly(AT) enrichment across introns that were preferentially retained or unaffected following indisulam treatment. Shading, 95% confidence intervals estimated by bootstrapping.

(G) Left: RNA-seq read coverage illustrating *Prpf40b* intron retention in the cytoplasmic fraction following indisulam treatment of B16-F10. Right: quantification of *Prpf40b* intron retention in total, nuclear (nuc.), and cytoplasmic (cyto.) fractions. p from unpaired t test.

(H) Predicted 9-mer peptides arising from indisulam-induced *Prp40b* intron retention. Black/blue, exon/intron-derived amino acids.

(I) Filtering strategy to predict potential indisulam-induced, MHC I-bound epitopes. Numbers of unique peptides present at each step are shown for representative MHC I alleles following DMSO or indisulam treatment of B16-F10 and 501-MEL cells.

(J) Bar graph illustrating numbers of predicted indisulam-induced 8- to 14-mer peptides arising from different splicing events following DMSO or indisulam treatment of B16-F10 cells. All analyses performed for n = 3 biological replicates for each cell line and treatment unless specified otherwise.

Figure 2.5. Indisulam-induced neopeptides are presented by MHC I.

(A) Workflow overview.

(B) Schematic for RNA isoform and proteome database creation.

(C) Histogram of predicted NetMHCpan binding rank of all peptides identified from the H-2D^b immunoprecipitation (IP) and full-length proteome. Peptides with rank <2 are predicted binders. Peptides identified in DMSO-treated (gray, left) and indisulam-treated (red, right) samples are overlaid on a random sample of 1,000 sequences from the full-length proteome (black) for comparison.

(D) Sequence logo for 9-mers identified from the H-2D^b IP and full-length proteome.

(E) Bar plot of numbers of peptides identified from the H-2D^b IP using each proteome in (B).

(F) Bar plot of numbers of predicted binders and non-binders identified from H-2D^b IP using the spiked non-binders proteome, which consists of predicted binders (rank <2) composing 90% of this proteome, and non-binders (rank >90), added to constitute 10% of the proteome.

(G) Density plots of parent gene expression for peptides identified from the H-2D^b IP from DMSO-treated (gray, left) and indisulam-treated (red, right) samples, each compared to the expression of all genes (black) following treatment with DMSO or indisulam, respectively, using the predicted binders proteome. TPM, transcripts per million.

(H) Heatmap illustrating each peptide identified in at least one replicate (rows) using the predicted binders proteome. Columns are peptides.

(I) Bar plot illustrating percentages of indisulam-specific, isoform-specific identified peptides arising from different types of alternative splicing.

(J–M) RNA-seq coverage plots of representative indisulam-induced, candidate splicing-derived neoepitopes generated by intron retention in (J) *Hus1* and (K) *Zfp512*, (L) competing 3′ splice sites in *D14*Abb1e, and (M) cassette exon skipping in *Poldip3*. Indisulam-promoted peptide shown in bold, underlined text.

(N–Q) Median fluorescence intensities (MFIs) of H-2D^b and/or H-2K^b on RMA-S cells following incubation with increasing doses of (N) Hus1, (O) Zfp512, (P) D14Abb1e, and (Q) Poldip3 candidate neoantigenic peptides from (J)–(M). Mean ± SD shown. For (N)–(Q), gray lines indicate negative control peptides randomly selected from the predicted non-binder, "spike-in" peptides used in (B). All analyses performed for n = 3 biological replicates for each treatment for (A)–(M) and n = 4 biological replicates for (N)–(Q). For (C), (D), and (G), data collated across n = 3 replicates per treatment.

Figure 2.6. Splicing-derived neoepitopes are immunogenic *in vivo.*

(A) Heatmap representing mean MFI of H-2K^{b} from RMA-S assay. Green, immunogenic controls.

(B) Immunization schema.

(C) Representative IFN-γ ELISpot from $CD8^+$ T cells upon stimulation with syngeneic peptide-loaded splenocytes. Each row is a peptide used for *in vivo* immunization. Columns, T cells reacted with the indicated stimuli. PMA, phorbol 12-myristate 13-acetate; Iono, ionomycin.

(D) Spots per 10^5 $CD8^+$ T cells from IFN-γ ELISpot for peptides identified as immunogenic. Bar indicates median. SIINFEKL, positive control. Each dot is one technical replicate.

(E) Representative IFN-γ ELISpot of $CD8^+$ T cells from immunized mice, following stimulation with syngeneic peptide-loaded splenocytes. Each row is one dose. Columns, T cells reacted with the indicated stimuli. Plots on right quantify numbers of dots per well; each dot is one technical replicate.

(F) Comparisons of predicted MHC I binding for immunogenic (IFN-γ ELISpot-positive) versus nonimmunogenic peptides.

(G) As (F), but with RMA-S MFIs. For (F) and (G), p from two-sided Wilcoxon rank-sum test.

Figure 2.7. Splicing-derived neoantigens trigger an endogenous T cell response.

(A) Schema of co-culture of $CD8^+$ T cells from peptide-immunized C57BL/6 mice with peptide-loaded B16-F10 cells for cytotoxicity.

(B) Bar plot of live B16-F10 cells from (A). Each dot is a technical replicate. p from Wilcoxon rank-sum test.

(C) Schema of $CD8^+$ T cells from peptide-immunized C57BL/6 mice, stimulated with B16-F10 cells treated with DMSO or indisulam for IFN-γ ELISpot.

(D) Representative IFN-γ ELISpot from $CD8^+$ T cells following stimulation with DMSO or indisulam-treated B16-F10 cells, or B16-F10 cells overexpressing ovalbumin. Rows, peptides used for immunization.

(E) Bubble plot of data from (C) and (D); size of bubble indicates number of spots. p from Wilcoxon rank-sum test.

(F–H) Box-and-whisker plots for representative peptides from (E). Each dot is one technical replicate. p from Wilcoxon rank-sum test.

(I) RNA-seq coverage plots demonstrating mis-splicing of *Eif4g3* (left) and *Stat2* (right) upon indisulam exposure and the resulting neoantigenic peptides.

(J) Representative plots of peptide:MHC I tetramer staining of $CD8^+$ T cells from tumor-draining lymph nodes of B16-F10 tumor-bearing mice treated with vehicle, anti-PD1, indisulam, or the combination and analyzed at day 14, gated on $CD3^+$ T cells. Each row is one neoantigenic peptide, and columns indicate treatment condition.

(K) Quantification of (J); each dot is one mouse. p from Kruskal-Wallis ANOVA.

2.6 SUPPLEMENTAL FIGURES


The image part with relationship ID rId12 was not found in the file.

Figure 2.8. Supplementary 1. Pharmacologic perturbation of RNA splicing impairs tumor growth *in vivo*, in a dose-dependent fashion dependent on adaptive immunity, related to Figure 1.

(A) Left, western blot of RBM39 after *in vitro* exposure to the indicated concentrations of indisulam for 24 hours in MC38 and CT26 cells. Right, half-maximal inhibitory concentration (IC_{50}, computed using the Hill equation) values for cell growth inhibition and RBM39 degradation. (B) Dose-response curves for RBM39 abundance (normalized to β-actin) across the indicated concentrations of indisulam treatment as measured by densitometry. IC_{50} values are shown. (C) Western blot of RBM39 after MC38 or CT26 cells were exposed to 1 μM indisulam for 96 hours, drug was washed off, and RBM39 levels were allowed to recover. (D) Annexin-V and DAPI analysis of MC38, B16-F10, CT26, and MB49 cells after *in vitro* treatment with indisulam 1 μM or DMSO for 96 hours. (E) Heatmap of MFI values above isotype control of cell surface levels of H-2K/H-2D, I-A/I-E (MHC II), or PD-L1 after 96 hours of treatment with DMSO, indisulam 1 μM, MS-023 5 μM, or EPZ015666 1 μM, or the same drugs in the presence of mouse IFNγ 10U/mL. CRISPR-mediated β_2-microglobulin knockout cells served as biologic control for H-2K/H-2D staining. B16-F10 cells shown on top (blue). CT26 cells on bottom (red). Representative histograms of B16-F10 data are shown on right. (F) Cell surface levels of cytokine and death receptors in B16-F10 cells after treatment with conditions identical to (D). (G) Sample photos of B16-F10 (top), MC38 (middle), CT26 (bottom) bearing mice treated with indisulam or DMSO and engrafted into syngeneic animals. (H) Experimental schema. MC38 or CT26 cells were treated with DMSO or indisulam at the indicated concentrations for 96 hours in technical triplicate; these were then subjected to RNA-seq analyses or used for biological experiments as in (L-O). (I) numbers of constitutive U2-type introns retained in MC38 cells treated with the indicated doses of indisulam compared with DMSO. (J) Total number of splicing alterations in CT26 and MC38 tumors exposed to the indicated doses of indisulam, as compared with DMSO. (K) RNA-seq coverage plot depicting two representative intron retention events in Agxt2l2 and Hmgxb4 with

increasing doses of indisulam. (L) experimental schema showing the engraftment of CT26 tumors treated with indisulam *in vitro* into syngeneic BALB/c mice. (M) tumor volumes of CT26 bearing mice from (L) over time (n = 15 mice/group; tumors engrafted on bilateral flanks of mice). Mean ± sem. (N) tumor volumes from (M) at day 24. P values were calculated for the indicated group compared to DMSO control using the Wilcoxon rank-sum test: $^{*}p = 0.048$; $^{***}p = 0.000798$; $^{****}p = 0.000363$. (O) Kaplan-Meier survival curve of animals from (L). (P) Individual tumor growth curves for DMSO-treated and indisulam-treated B16-F10 cells in Rag2 knockout mice. n = 10 mice per group; tumors engrafted on bilateral flanks. (Q) Box-and-whisker plots of day 28 individual tumor volumes from (P). (R) Schema of CD4 & CD8 T cell depletion or NK cell depletion versus control. (S) Representative flow cytometry confirmation of T cell depletion using anti-CD4 and anti-CD8 antibodies, gated for CD3ε in the spleens of animals sacrificed at day 19 post-tumor challenge. Remaining double-negative population are $NK1.1^{+}$ NKT cells (not shown). (T) Representative flow cytometry confirmation of NK cell depletion via NKp46 antibody; peripheral blood on day 14 after tumor challenge. (U-V) Box-and-whisker plot quantification of (S) and (T). Each dot represents an individual animal. (W) Sample photos of tumor-bearing animals treated with CD4/CD8 T cell depletion and challenged with B16-F10 cells pre-treated with indisulam or control. (X) Individual tumor growth curves for NK1.1 depletion experiment. n = 10 per group; tumors engrafted on bilateral flanks. (Y) Box-and-whisker plots of day 21 tumor volumes for B16-F10 treated as in Figure 1A, with or without NK cell depletion. $^{*}p < 0.05$; $^{**}p < 0.01$. ANOVA calculated using the Kruskal-Wallis test and multiple comparisons versus DMSO alone calculated using the Dunn's test.

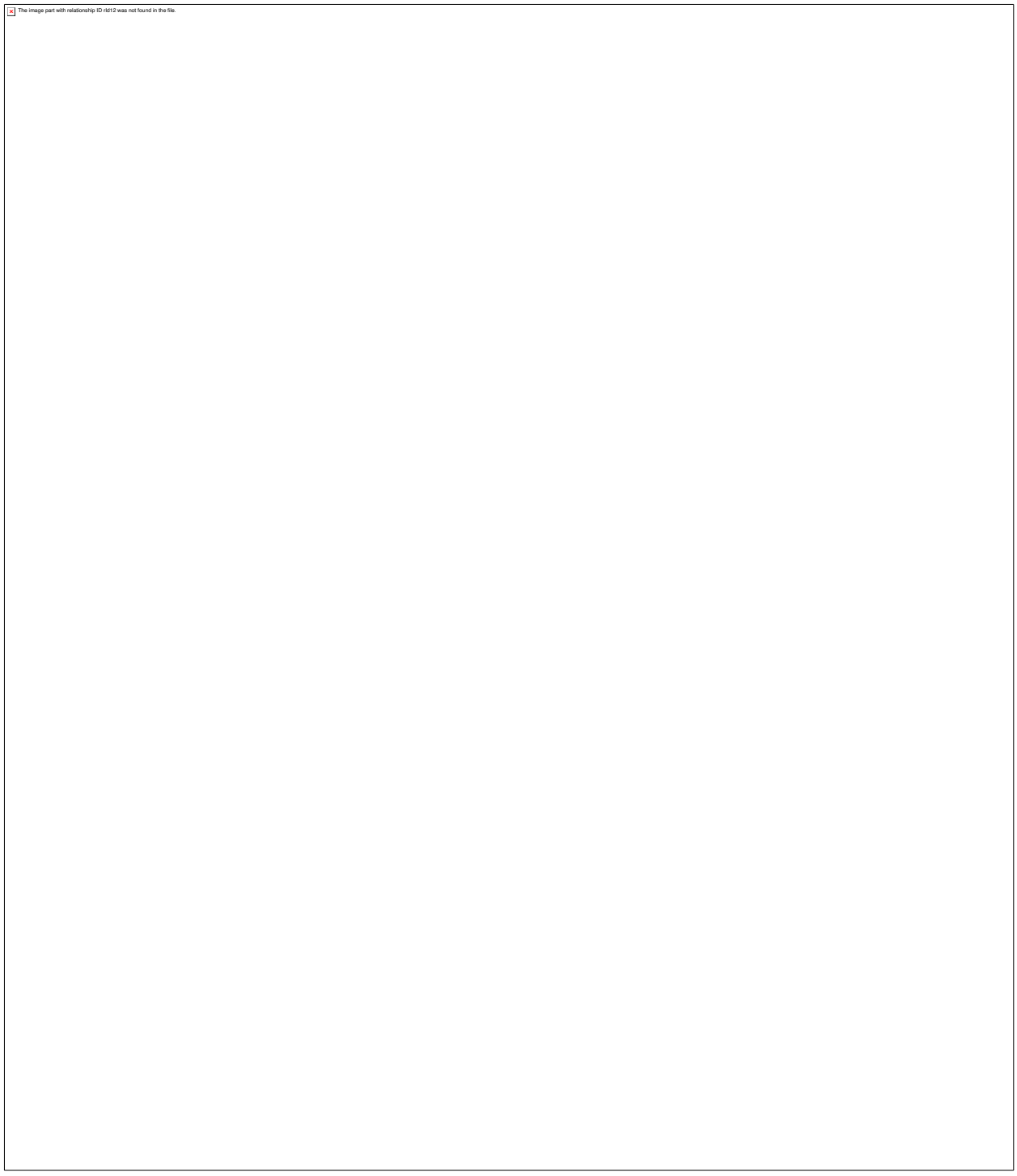
The image part with relationship ID rId12 was not found in the file.


The image part with relationship ID rId12 was not found in the file.

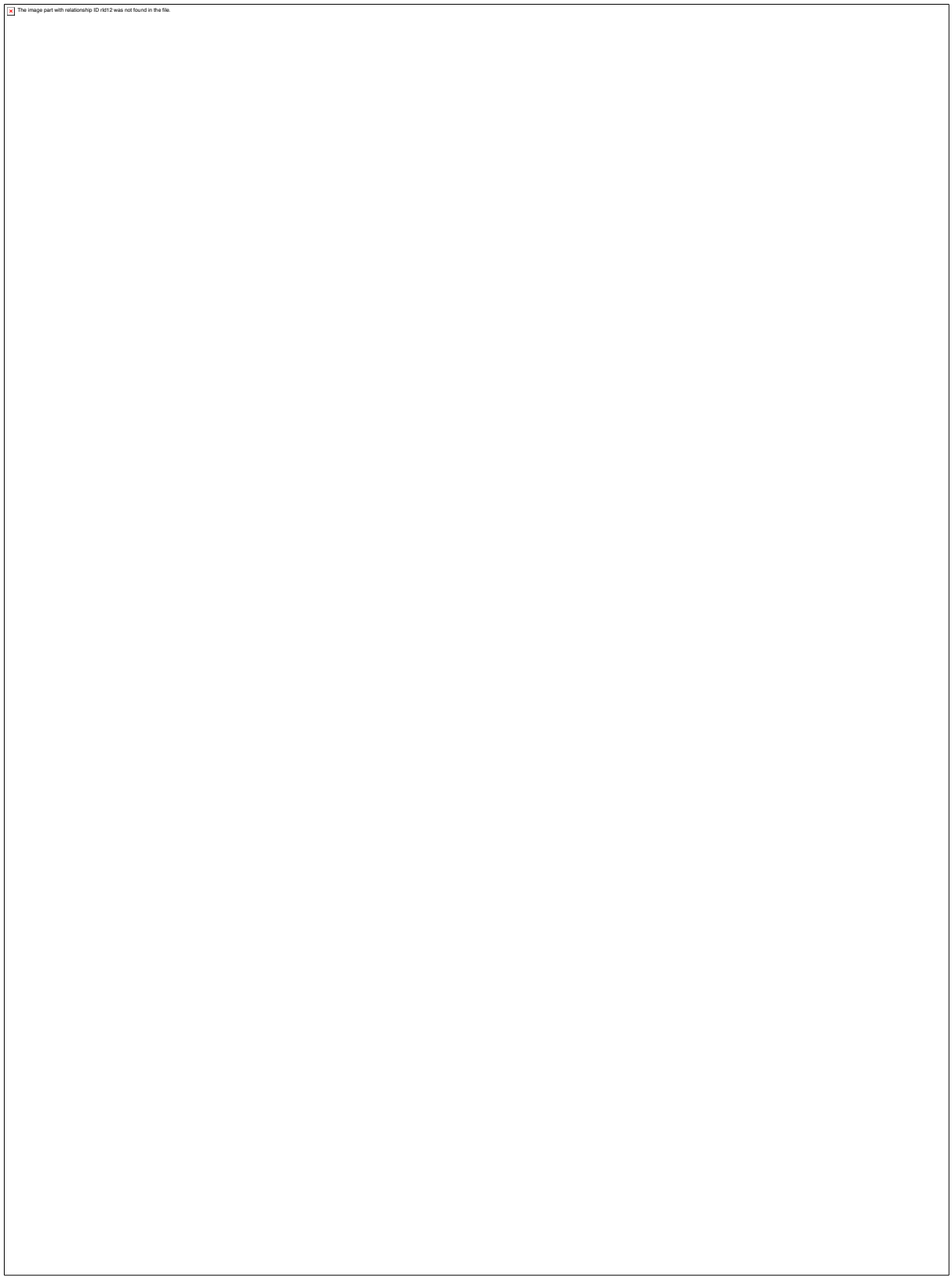
The image part with relationship ID rId12 was not found in the file.

Figure 2.9. Supplementary 2. Class-specific effects of splicing modulator drugs on hematopoiesis, T cell gene expression, and function *in vitro* and *in vivo*, related to Figure 2.

(A) Left, western blot showing dose-dependent reduction in asymmetric dimethyl arginine (ADMA) with MS-023 treatment in MC38 tumor cells; right, corresponding flow cytometry analysis for intracellular ADMA. (B) Schema for the mixed leukocyte reaction, depicting generation of tumor lysates, generation of bone marrow derived dendritic cells, process of pulsing dendritic cells with lysates and lipopolysaccharide (LPS) for maturation and antigen presentation, and mixed leukocyte reaction with congenic CD45.1 CFSE-labeled naive splenic T cells. (C) Schema depicting purification of splenic T cells, CFSE labeling, and *in vitro* stimulation with plate-bound anti-CD3 and anti-CD28 antibody in the presence of splicing drugs. (D) Full dose range of splicing drugs tested in (C) demonstrating dose-dependent inhibition of CFSE dye dilution and T cell proliferations at higher drug concentrations; representative histogram from N = 8 technical replicates each. (E) absolute numbers of CD4 (left) and CD8 (right) T cells from experiment in (C) for each drug and concentration were quantified to calculate IC_{50} for cell proliferation (table). Each dot is the average from 3-8 technical replicates. Curves and IC_{50} values for the activation markers CD25 and PD1 are shown (bottom panels), and EC_{50} for induction of apoptosis as measured by annexin-V staining is shown (middle panel). (F) OT-1 killing assay against wild-type or ovalbumin-expressing MC38 tumors; experiment performed as in Figure 2G. (G) representative contour plots showing the staining of OT-1 cells for TNFα and IFNγ or isotype control, after exposure to DMSO (left) or PMA/Iono (Phorbol 12-myristate 13-acetate and Iono: ionomycin, right). Percentage of positive cells are quantified in the associated bar plots. Each dot is one technical replicate. (H) As in (G) but OT-1 cells were stimulated with PMA/Iono (top) or incubated with MC38 cells overexpressing ovalbumin at a 1:1 ratio (bottom), at the indicated

concentrations of indisulam or MS-023 on the x axis. Graph shows mean ± sem. N = 4 technical replicates per condition. (I) Experimental schema demonstrating normal intracellular localization of the LAMP1 protein on cytotoxic granules in resting cytotoxic T cells, and appearance of LAMP1 on the plasma membrane upon T cell degranulation, rendering the protein stainable for flow cytometry. Bar plots at right show LAMP1 MFI of OT-1 cells remaining unstimulated, exposed to PMA/ionomycin, or incubated at a 1:1 ratio with MC38 overexpressing ovalbumin. Each dot indicates a technical replicate. P values were calculated using the Wilcoxon rank-sum test. (J) experiment as in (I) except in the presence of the indicated doses of indisulam or MS-023 on the x axis. N = 4 technical replicates per condition. Graph shows mean ± SD. P values were calculated using the Kruskal-Wallis non-parametric ANOVA test. (K) experimental design: naive C56BL/6 splenic T cells were isolated and cultured *ex vivo* for 96 hours in media with IL-2 50U/mL. Cells were either left unstimulated, or activated with plate-bound anti-CD3 + CD28 antibody in the presence of DMSO or the indicated splicing compounds: indisulam 1 μM, MS-023 1 μM, EPZ015666 5 μM, or pladienolide B 2nM. At the end of 96 hours, cells were subjected to RNA-seq. N = 3 replicates for each condition. (L) Differential gene expression from (K) of unstimulated T cells versus those stimulated in the presence of DMSO. (M) Boxplots of fold changes of the top 100 upregulated genes in T cells undergoing activation from (K) in the presence of the indicated drugs. Each dot is one replicate. (N) Schema of adoptive transfer of C57BL/6 CD45.1 CFSE labeled T cells into syngeneic, minor antigen mismatched, or major antigen mismatched lethally irradiated recipients to assess T cell activation and expansion. (O) Histograms of CFSE dilution of donor adoptively transferred CD45.1$^+$ CD8$^+$ T cells into BALB/c mice on day 3 to assess for alloreactivity. (P) Representative flow cytometry plots of T cell activation and death markers in adoptively transferred donor CFSE-labeled CD45.1 splenic CD4$^+$ or CD8$^+$ T cells into

lethally irradiated BALB/c recipients with or without daily indisulam (25 mg/kg) treatment. Spleens were analyzed on day 3. Two animals from each condition are shown. (Q) as in (P) but with daily MS-023 treatment, 50mg/kg daily. (R-S) Histograms of CFSE dilution in donor adoptively transferred CD45.1^{+} T cells into syngeneic C57BL/6 mice to assess for homeostatic proliferation. Cells in the spleen on day 7 after transfer are shown. (T) Numbers of colonies in M3434 methylcellulose media on day 7. 25,000 red blood cell-lysed bone marrow hematopoietic stem and precursor cells (HSPC) from C57BL/6 mice were grown in methylcellulose with continuous exposure to splicing compounds at the indicated concentrations.

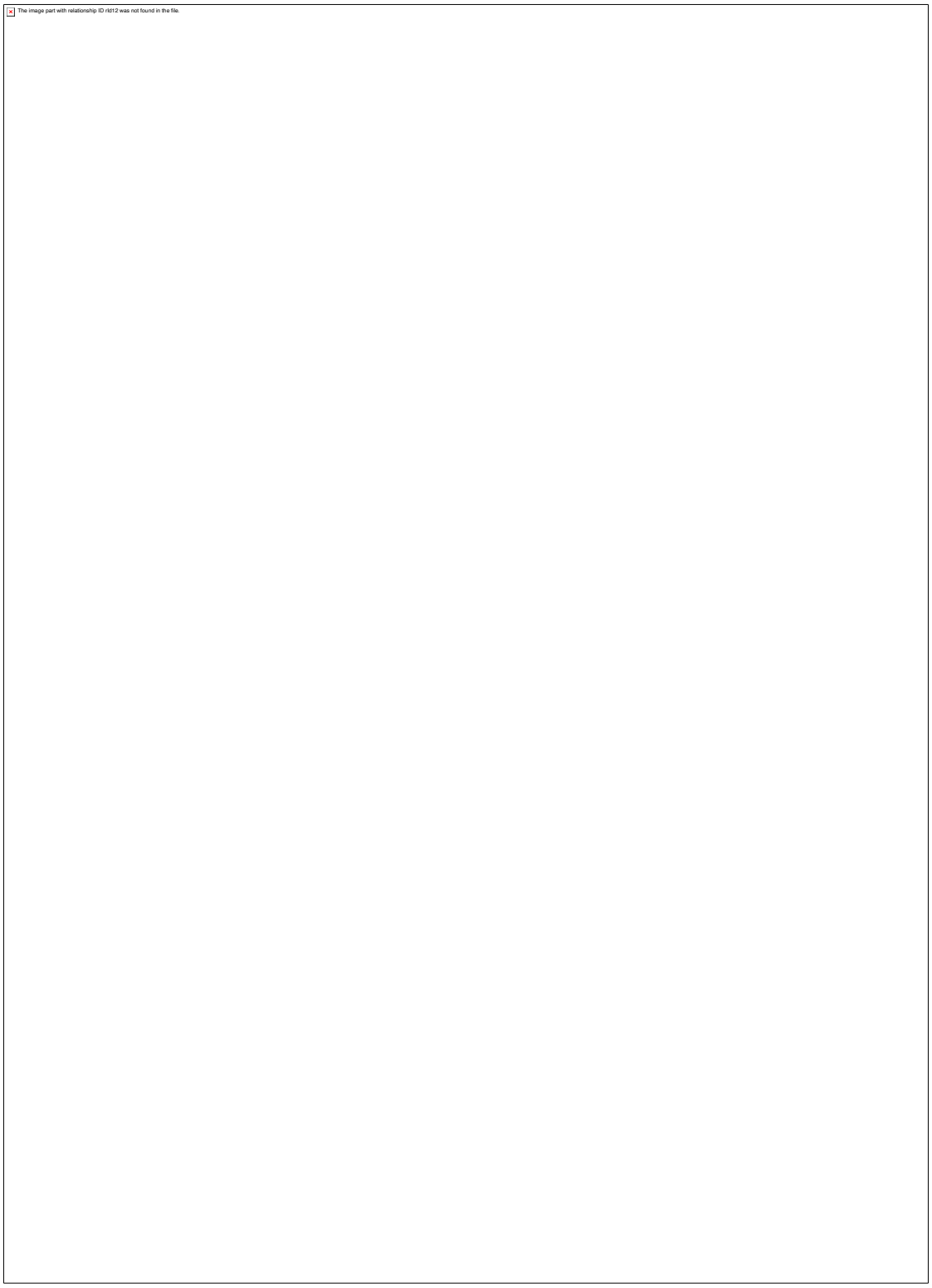

Figure 2.10. Supplementary 3. Treatment of tumor-bearing animals with splicing modulator compounds *in vivo* enhances tumor control and can elicit memory, related to Figure 3.

(A) Growth curves of individual B16-F10 tumors from C57BL/6 mice exposed to the indicated treatment, as summarized in Figure 3C. Each line represents one tumor; termination of lines prior to the end of the experiment indicates animal mortality or euthanasia according to predetermined endpoints, as described in the Methods section. (B) Experimental design: MC38 cells were treated with DMSO or MS-023 *in vitro* for 96 hours, and then 10^6 cells engrafted onto the bilateral flanks of either naive C57BL/6 mice, or animals which had successfully rejected MC38 tumors previously after treatment with anti-PD1 and MS-023 *in vivo* (from Figures 3K–3M). (C) Growth curves of individual tumors from (B). Pink and purple arrows indicate tumors which were implanted but rejected. (D) Line graphs summarizing growth curves from (C), showing mean ± sem. (E) Violin plots showing tumor volumes at day 28. P values (calculated using the Wilcoxon rank-sum test) for the "DMSO survivor" -versus "DMSO naïve" and "MS-023 survivor" -versus- "MS-023 naïve" comparisons are 0.044 and 0.011, respectively. (F) Representative animals from (E).


The image part with relationship ID rId12 was not found in the file.

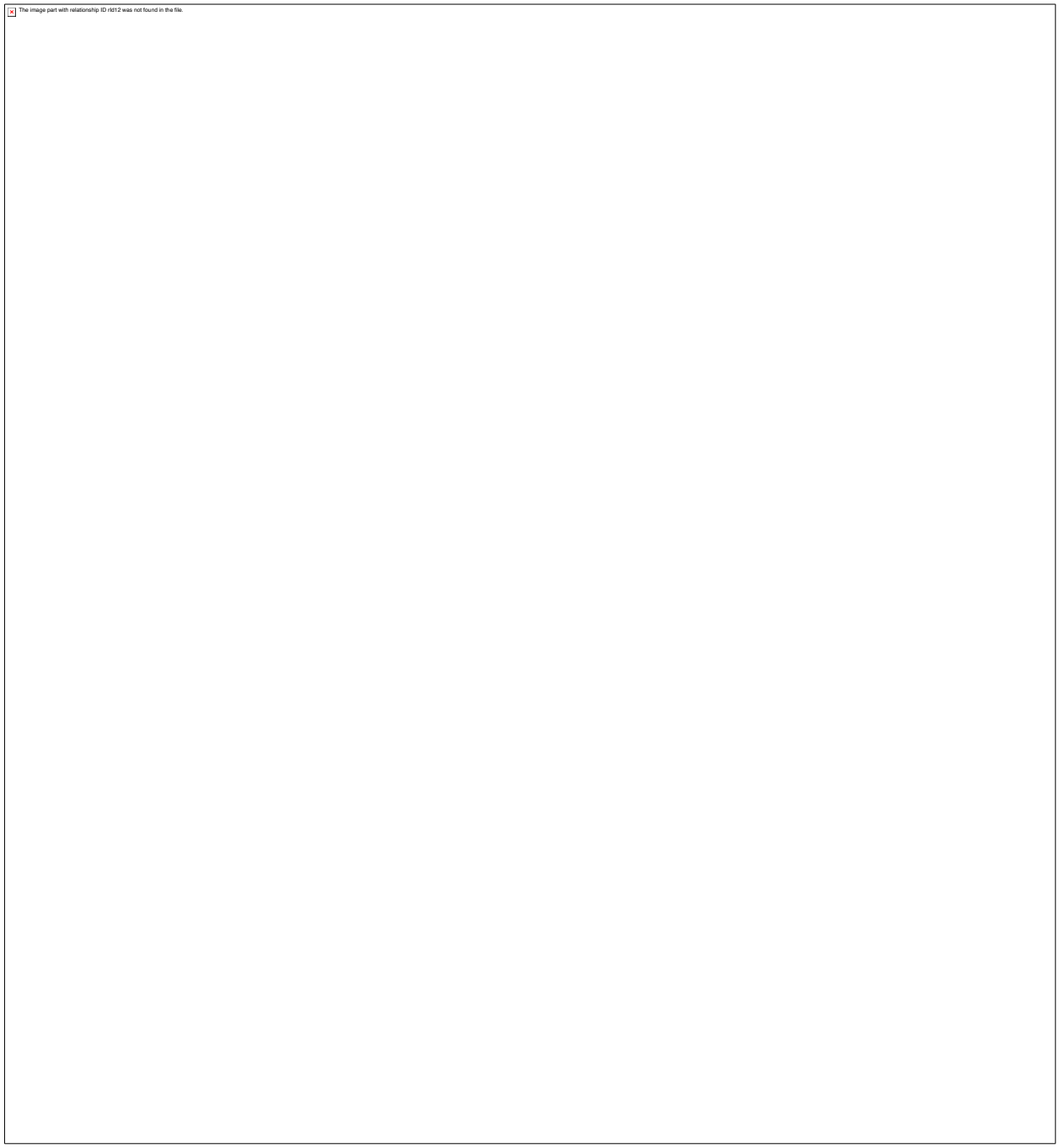
The image part with relationship ID rId12 was not found in the file.

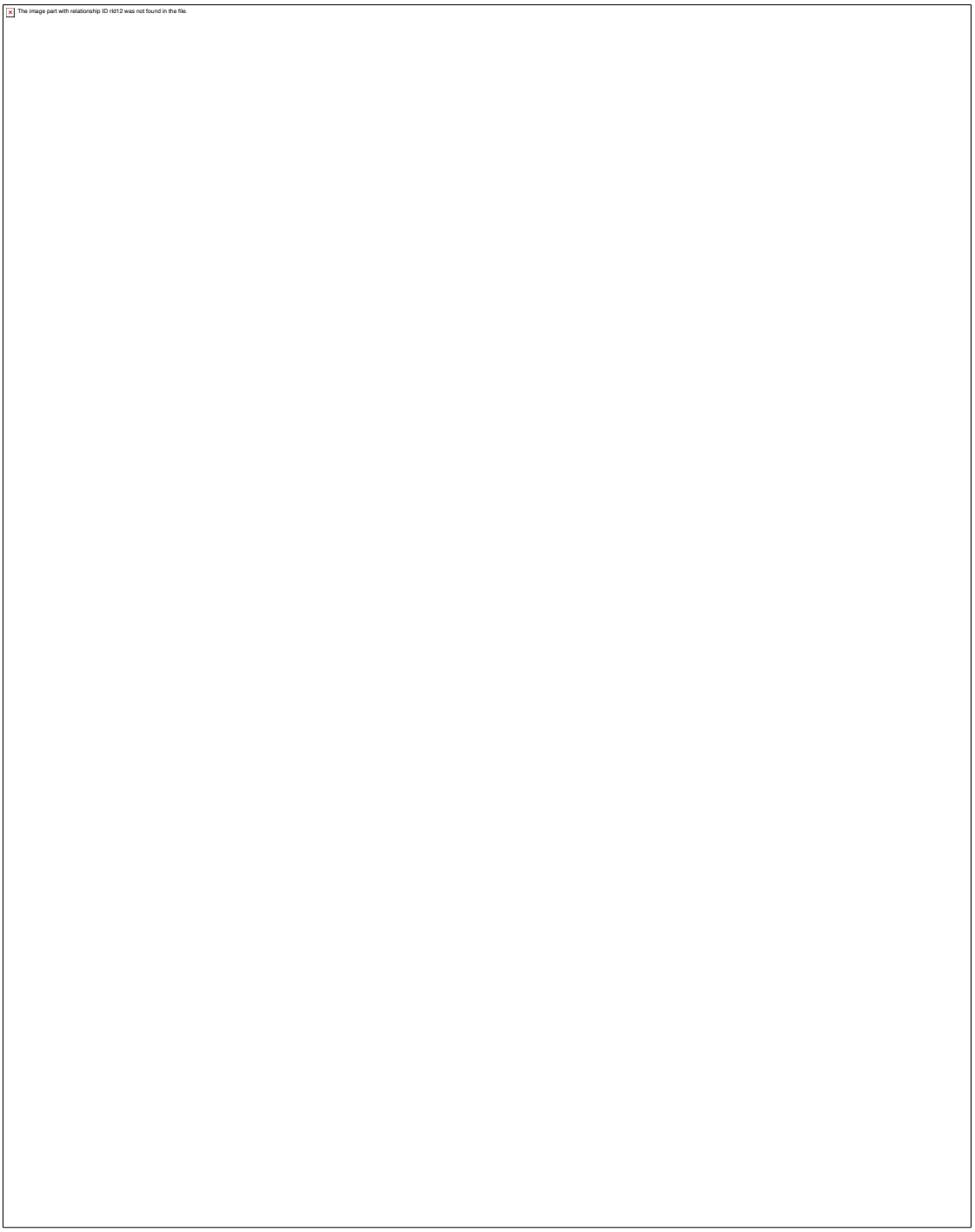

Figure 2.11. Supplementary 4. Lack of toxicity and absence of inflammatory signatures or increased $CD8^+$ T cell infiltrates into healthy, non-tumor tissues in animals treated with splicing modulator compounds with or without anti-PD1, related to Figure 3.

(A) Peripheral blood counts of tumor-bearing mice treated for 3 weeks with vehicle, anti-PD1 (250 μg flat dose), indisulam (25 mg/kg), MS-023 (50 mg/kg), or combined anti-PD1 with MS-023 or indisulam. ALC: absolute lymphocyte count; ANC: absolute neutrophil count; Hgb: hemoglobin; Plt: platelet count; WBC: white blood cell count. (B) Percentage of $CD8^+$ cells among $CD45^+$ cells (left) and proportion of $CD8^+/CD11b^+$ cells (right) in tumors at day 21 following treatment of animals bearing MC38 tumors with the treatments indicated on the x axis. n = 10 mice/group. ANOVA calculated using the Kruskal-Wallis test. (C) H&E stained tissue sections from mice treated with indisulam, MS-023, anti-PD1, or combination at day 21. N = 5 animals per treatment group per tissue were assessed. Review of the necropsy tissues shows no overt evidence of toxicity, and the tongue shows typical squamous epithelium overlying bundles of skeletal muscle. The lung demonstrates typical alveolar spaces, alveolar septa, and bronchioles with respiratory epithelium. The large intestine shows typical colonic mucosa, submucosa, and muscularis propria. The skin from the ear demonstrates typical epidermis, dermis, and subcutaneous tissues overlying cartilage. The liver shows typical portal tracts and hepatocytes, and the small intestine demonstrates normal villi with typical mucosa, submucosa, and muscularis propria. Representative micrographs of the findings are depicted. (H&E; Magnification 400x; Scale bar: 50 microns). (D) Liver and pancreas enzymes and markers in the blood from these same animals at the time of sacrifice (n = 3 mice/group). ALT: alanine aminotransferase. AST: aspartate aminotransferase. Mean ± sd shown. (E) B16-F10-tumor bearing C57BL/6 mice received the indicated treatment; tissues were collected on day 21. Paraformaldehyde-fixed and paraffin-embedded tissues were sectioned and stained for CD8 by immunohistochemistry. Representative sections of the tongue (muscle), liver, ear (skin), small and large bowel and lung are shown. 20x magnification. Scale bar: 100 microns. (F) Violin plots depicting the automated enumeration of

$CD8^+$ T cell infiltrates in the corresponding organs are shown. N = 3 mice per tissue per treatment were analyzed, and N = 5 fields per mouse were analyzed. Fold-change in $CD8^+$ T cell infiltrates versus the vehicle condition are shown. p values were calculated using the Wilcoxon rank-sum test. (G) Experimental design: C57BL/6 mice were engrafted with 10^6 MC38 tumor cells on each flank and subjected to treatment with vehicle, indisulam 25mg/kg beginning day +3, anti-PD1 250 μg twice weekly beginning day +7, or the combination. Lung, colon, and splenic T cells were obtained on day 14 after tumor challenge for RNA-seq. (H) Stacked bar graphs indicating the absolute number and type of splicing alterations in the lungs, colon and T cells of animals receiving the indicated therapy. Splicing alterations were defined as a 5% change in splicing with a p value threshold of 0.05 (I-K) Scatterplots indicating constitutive intron retention in tissues of animals treated with indisulam versus vehicle. (L-N) Scatterplots indicating differentially expressed genes in the colon, lung and T cells of animals treated with vehicle versus combination of indisulam and anti-PD1. (O) Pathway analyses of differential gene expression from (L-M) in the colon and lung. No significantly enriched gene ontology pathways were identified in the T cell RNA-seq dataset.


The image part with relationship ID rId12 was not found in the file.

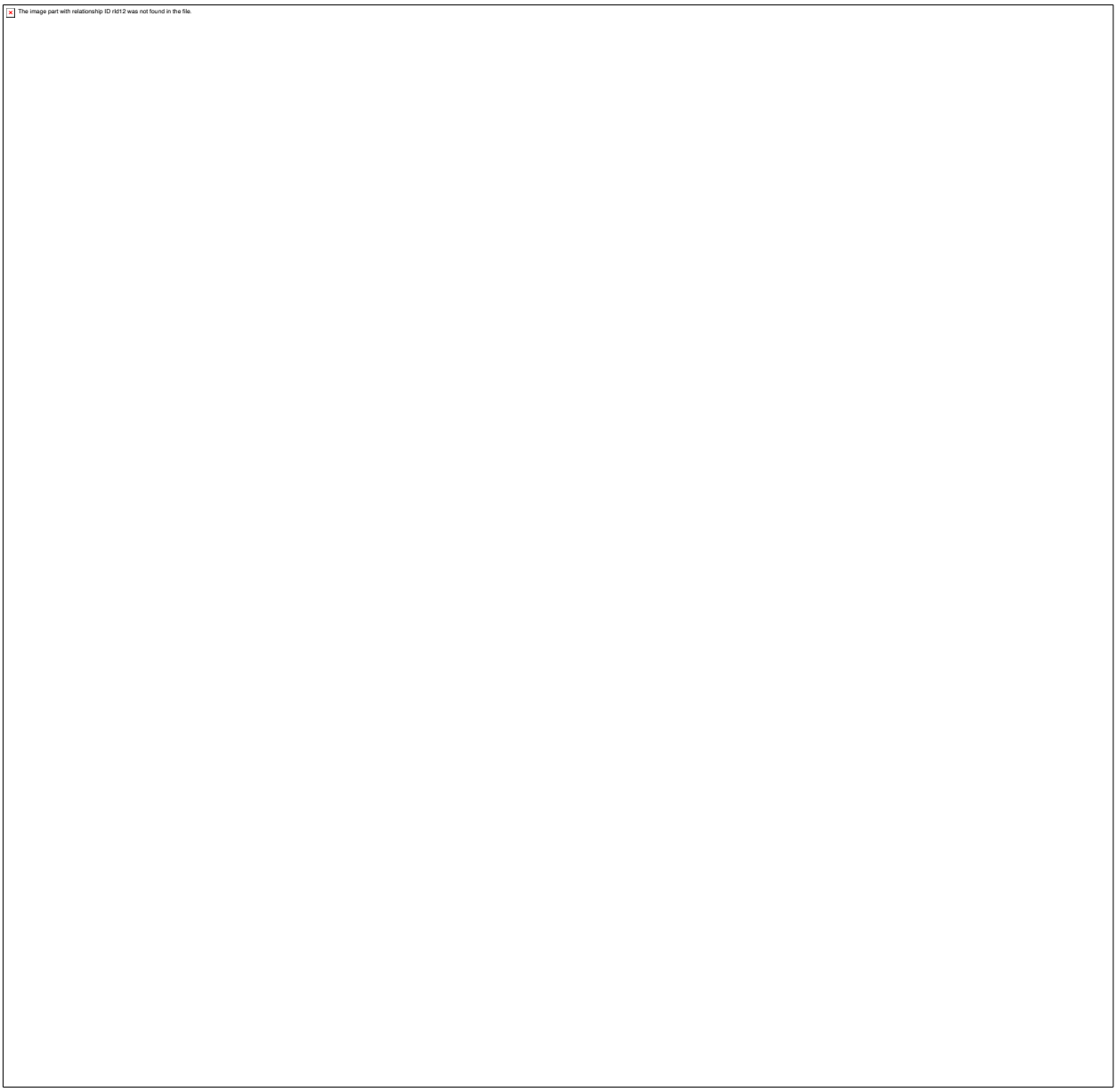

Figure 2.12. Supplementary 5. Splicing alterations generated by MS-023 and indisulam treatment, related to Figure 4.

(A) Left, scatterplot comparing constitutive intron splicing in DMSO- versus MS-023-treated B16-F10 cells. Right, RNA-seq read coverage illustrating increased intron retention following MS-023 treatment. (B) As (A), but for cassette exons. (C) Bar graphs representing numbers of differentially spliced events of each indicated type in DMSO- versus MS-023-treated B16-F10 cells. Blue/green,

mis-splicing events indicative of reduced/increased splicing efficiency (for example, decreased/increased cassette exon inclusion). (D) As (A), but for human SK-MEL-239 cells. (E) As (D), but for cassette exons. (F) As (C), but for human SK-MEL-239 cells. (G) representative example of a 5′ alternative splice site event induced with indisulam treatment in all of the murine cell lines studied. (H-I) two representative examples of intron retention events observed in all murine cell line studied. (J) Venn diagram depicting the number of genes mis-spliced in common across mouse versus human cell lines analyzed, upon exposure to either indisulam or MS-023. (K) Left, heatmap illustrating Pearson correlations for all retained introns, constitutive introns, and cassette exons that are differentially spliced following indisulam or MS-023 treatment in at least one sample from the indicated mouse cell lines. Pearson correlations computed using the absolute isoform expression values (0%–100%) for each splicing event. Right, identical analysis, but for human data. Dendrograms, unsupervised clustering by the Euclidean distance method. (L) Venn diagrams depicting shared mis-splicing events upon exposure to indisulam or MS-023 in the indicated murine cell lines. (M) as for (L) but for the indicated human cell lines studied. (N) Bar graph of *Malat1* RNA levels in the cytoplasmic (cyto.) and nuclear (nuc.) fractions of DMSO-treated B16-F10 cells. As *Malat1* RNA is restricted to the nucleus (Hutchinson et al., 2007), these data confirm the specificity of our fractionation. (O) RNA-seq read coverage illustrating that increased *Prpf40b* intron retention following indisulam treatment of B16-F10 cells is evident in total (left), nuclear (middle), and cytoplasmic (right) fractions. Gray, DMSO treatment; red, indisulam treatment. (P) Scatterplot comparing constitutive intron splicing in the cytoplasmic fractions of DMSO- versus indisulam-treated B16-F10 cells. Increased intron retention is readily evident in the cytoplasm. (Q) Venn diagram indicating shared and unique predicted neoantigens among mouse and human cell lines, treated with either indisulam or MS-023. (R) Shared and

unique predicted neoantigens, across mouse and human cell lines upon treatment with splicing modulator compounds.

Figure 2.13. Supplementary 6. Analysis of mass spectrometry results for H-2D^b and H-2K^b immunoprecipitations, related to Figure 5.

(A) As Figure 5A, but for H-2K^b immunoprecipitation. (B) As Figure 5D, but for H-2K^b immunoprecipitation. (C) Histogram of lengths of identified peptides using the predicted binders proteome. The majority of identified peptides are 8-9-mers, as expected. (D) As Figure 5E, but for H-2K^b immunoprecipitation. (E) As Figure 5F, but for H-2K^b immunoprecipitation. (F) As Figure 5G, but for H-2K^b immunoprecipitation. (G) Table showing selected candidate neoantigenic peptides induced by indisulam exposure and shared across MC38, B16-F10, CT26 and MB49 mouse tumor cell lines, which were subjected to experimental analysis by TiterMax immunization of C57BL/6 mice followed by evaluation of reactive CD8$^+$ T cells by IFNγ ELISpot.


The image part with relationship ID rId12 was not found in the file.

Figure 2.14. Supplementary 7. Functional evaluation of candidate splicing-derived, neoantigenic peptides, related to Figures 6 and 7.

(A) Schema of MHC I peptide stabilization assay on TAP-deficient RMA-S cells. (B) Heatmap of mean MFI values of H-2D^{b} levels from RMA-S peptide stabilization experiments across 30

peptides identified as binding to H-2D^b in the RMA-S assay. Green text indicates control known immunogenic peptide with H-2D^b binding (gp100). (C) Number of spots per 10^5 CD8$^+$ T cells from IFNγ ELISpot quantified across 70 peptides derived from mass spectrometry analyses and tested *in vivo* which did not elicit an immune response. Bar indicates median. Each dot represents a technical replicate. (D) Diagram of experiment immunizing C57BL/6 mice with graded doses of candidate peptides at 0.1, 1, 10, or 100 μg followed by analysis of CD8$^+$ T cells in IFNγ ELISpot. (E) Results from experiment described in (D), with graded doses of the indicated peptide on the x axis. Each dot indicates one technical replicate. (F) As (B), but for H-2K^b and H-2D^b expression levels from the RMA-S assay for candidate splicing-derived neoantigenic peptides induced by indisulam that were identified based on RNA-seq data and MHC I binding predictions alone. Some peptides appear twice as they bind to both H-2K^b and H-2D^b. (G) As (C), but for the 39 candidate splicing-derived neoantigenic peptides induced by indisulam identified based on RNA-seq data and MHC I binding predictions alone. (H) RNA-seq coverage plots of representative indisulam-induced, candidate splicing-derived neoantigens generated by intron retention events in *Kdm4b* and *H2-Ke6*, cassette exon inclusion in *Mon2*, and competing 3′ splice sites in *Zpf637*. Indisulam-promoted peptide shown in bold, underlined text. (I) Median fluorescence intensities (MFIs) of H-2D^b and/or H-2K^b on RMA-S cells following incubation with increasing doses of candidate nonantigenic peptide from (H). Mean ± sd shown. (J) Representative ELISpot images for the peptides from (H). (K) Schema of peptide:MHC I tetramer studies. B16-F10 tumor-bearing animals were treated with vehicle, anti-PD1, indisulam or the combination and were sacrificed at day 14 post-tumor challenge. Tumor-draining lymph nodes were analyzed for the frequency of tetramer-positive CD8$^+$ T cells.

2.7 METHODS

2.7.1 *Data and code availability*

RNA-seq data generated as part of this study were deposited at the Gene Expression Omnibus (accession GSE162818). Software RRIDs (also available in the Key Resources Table) are: Bowtie RRID: SCR_005476, RSEM RRID: SCR_013027, TopHat RRID: SCR_013035, MISO RRID: SCR_003124, Samtools RRID: SCR_002105, Bioconductor RRID: SCR_006442, dplyr RRID: SCR016708, ggplot2 RRID: SCR_014601, Proteome Discoverer RRID: SCR_014477.

2.7.2 *Experimental model and subject details*

2.7.2.1 *Mice*

All *in vivo* experiments were approved by the Institutional Animal Care and Use Committees (IACUC) of Memorial Sloan Kettering Cancer Center and/or Fred Hutchinson Cancer Research Center and conducted in accordance with ARRIVE guidelines. All animals were housed in the respective specific pathogen-free (SPF) barrier facilities and maintained under standard husbandry conditions. B6(Cg)-Rag2tm1.1Cgn/J (RAG2 KO) mice, C57BL/6-Tg (TcraTcrb)1100Mjb/J (OT-1) mice and B6.129P2-B2mtm1Unc/DcrJ (B2M KO) mice were obtained from Jackson Laboratories (Cat. 008440, 003831, 002087 respectively). C57BL/6 mice, congenic B6.SJL-*Ptprc*^{a} *Pepc*^{b}/BoyJ (CD45.1) mice, BALB/c and LP/J mice were also obtained from Jackson Laboratories (Cat. 000664, 002014, 000651 and 000676). CD45.1, RAG2 KO, B2M KO, and OT-1 mice are all fully backcrossed onto the C57BL/6 genetic background. Unless otherwise noted in the text, females from 6-8 weeks old were used for all experiments. Animals within each genotype and treatment condition were randomly allocated to experimental groups; we did not exclude any allocated animals from our analyses. We minimized nuisance variables associated with the

vivarium by checking on each cage of animals at least daily, and randomizing the location of cages when animals were placed back in their housing. Multiple authors (S.X.L., D.C., H.C., M.S., C.E.) were assigned to each experiment to minimize bias due to animal handling techniques. Blinding was not feasible for animal tumor challenge, drug treatment, or tumor measurements as the same authors performed all of the above. Animal group sample sizes (indicated in Figure Legends) were determined based on prior published literature on the same tumor models, with differences in tumor growth as the primary outcome measure. Individual study designs, outcome measures and corresponding statistical tests for animal experiments and *ex vivo* analyses of primary murine tissues are otherwise described in the text and figure legends.

2.7.2.2 *Cell lines*

B16-F10, CT26.WT (CT26), and LLC cells were obtained from ATCC (Cat. CRL-6475, CRL-2638, and CRL-1642 respectively). MB49 cells were obtained from MilliporeSigma (Cat. SCC148, Burlington, MA); MC38 cells were obtained from Kerafast (Cat. ENH204-FP, Boston, MA). B16-F10 and MC38 cells expressing chicken ovalbumin (B16ova and MC38ova) were a kind gift of Jeff Ravetch (Rockefeller University, New York, NY). To generate β_2 microglobulin-deficient cell lines for *in vitro* experiments, four candidate sgRNAs for mouse β_2 microglobulin (#1 AGTATACTCACGCCACCCACCGG, #2 TCACGCCACCCACCGGAGAATGG, #3 GGCGTATGTATCAGTCTCAGTGG, #4 TCGGCTTCCCATTCTCCGGTGGG) or non-targeting control (GGAGCGCACCATCTTCTTCA) were cloned into pSpCas9(BB)-2A-Puro (PX459) as previously described (Ran et al., 2013) and used to engineer deficient MC38, B16-F10, and CT26 cell lines via transfection using XtremeGene 9 reagent as per manufacturer's instructions (MilliporeSigma Cat. 6365809001) followed by puromycin selection at 10 μg/mL for three days. Polyclonal cell populations were obtained by flow sorting for H-2K^b/D^b and β_2

microglobulin double-negative cells, and gene knockout further confirmed by stimulating a culture of these sorted cells for 48 hours with 10U/mL mouse IFNγ and analyzing for the same markers. For *in vivo* experiments, lentiCas9-Blast was used to generate Cas9-expressing B16-F10 cells. *B2m* gRNAs (GAGGGGTTTCTGAGGGCCAC, AGTATACTCACGCCACCCAC) and non-targeting control gRNAs (AAAAAGTCCGCGATTACGTC, ACCCATCCCCGCGTCCGAGA) were cloned into lentiGuide-Puro and introduced into Cas9-expressing B16-F10 cells via lentiviral transduction as previously described (Thomas et al., 2020) and underwent similar selection. PX459, lentiCas9-blast, and lentiGuide-Puro were kind gifts of Feng Zhang (Addgene Cat. 62988, 52962, 52963).

2.7.3 *Method details*

2.7.3.1 Pretreatment with splicing inhibitors

Unless otherwise specified, cell lines were treated with splicing inhibitors at the indicated concentrations for 96 hours *in vitro*, harvested and washed three times with PBS in excess to remove all drug, and then used for downstream analyses and/or subsequent studies, including phenotyping, RNA-seq analyses, continued growth *in vitro*, or tumor challenge *in vivo* into syngeneic animals.

2.7.3.2 In vivo tumor challenge

Unless otherwise specified, syngeneic B6 or BALB/c mice were engrafted subcutaneously on bilateral flanks with MC38, B16-F10, CT26 or LLC tumor cells at the following doses: MC38 10^6 cells, B16-F10 $0.5x10^6$ cells, CT26 $0.25x10^6$ cells, LLC $0.25x10^6$ cells. Tumors were measured serially twice or three times weekly and tumor volumes were estimated by length x width x height. Animals were monitored daily for survival and weighed twice weekly. Experimental endpoints

mandating euthanasia were approved by the IACUC and included: animal lethargy, severe kyphosis or evidence of pain, difficulty with ambulation or feeding, tumor ulceration > 1 cm or bleeding tumor, evidence of infected tumor, tumor volumes exceeding 2.5 cm^3, or animal total body weight loss > 10% from baseline.

2.7.3.3 Determination of cell growth, Annexin V, and activation marker IC_{50} values

Cell lines were grown with half-log_{10} concentrations of the indicated drug in 4 to 8 technical replicates under standard conditions until the control condition (DMSO or vehicle) was confluent by microscopy. For tumor cell lines, viable cells were quantified via the CellTiter-Glo® assay (Promega Cat. G7573) as per manufacturer instructions. For the *ex vivo* proliferation of T cells, viable cells were instead quantified via flow cytometry using counting beads. The percentage or number of viable cells with drug treatment was calculated relative to DMSO control (as 100%). These data were log_{10} transformed and a three-parameter nonlinear fit of log(inhibitor) versus response was performed in GraphPad Prism v9.0 (GraphPad Software, San Diego, CA) to determine IC_{50} values. For absolute cell number, Annexin V+, CD25+, and PD1+ flow cytometry data presented in Figure S4, dose-response models and IC_{50} values were computed using the R language's drc package (Ritz et al., 2015).

2.7.3.4 OT-1 cytotoxicity assay

Bulk splenocytes from OT-1 animals were cultured for three days with 100 U/mL murine IL-2 and 100 μg/mL SIINFEKL peptide to activate CD8+ T cells. Cultures were subsequently washed thoroughly to remove ova peptide and rested for at least 24 hours prior to use. OT-1 cells were passaged in T cell media with 50 U/mL IL-2 for no more than seven days from animal sacrifice

prior to use. For the cytotoxicity assay, tumor cells alone or OT-1 + tumor cells (1:1 ratio) were incubated in T cell media for 18 hours under standard conditions with the indicated concentrations of splicing drugs and analyzed by flow cytometry to quantify killing. OT-1 cells and other hematopoietic cells were excluded with the use of CD45, CD3, and CD8 staining. Tumor cell viability was measured using DAPI.

2.7.3.5 LAMP-1 T cell degranulation assay

OT-1 cells were generated as described for the cytotoxicity assay and incubated with ovalbumin-expressing tumor cell lines (pre-treated overnight with IFNγ 100U/mL to upregulate cell-surface MHC I) in the presence of DMSO or varying concentrations of splicing modulator drugs as indicated, in the presence of LAMP-1 antibody for 5-6 hours under standard incubator conditions. After the first hour of incubation, BD GolgiPlug (brefeldin A) and BD GolgiStop (monensin) was added at 1:1,1000 + 1:1,500 respectively into cells. At the end of incubation, cells were washed and stained for cell surface markers prior to standard flow cytometry.

2.7.3.6 Generation and use of peptide:H-2K^{b} tetramers

Peptide:MHC I tetramers with neoantigenic peptides and murine H-2K^{b} were generated using the QuickSwitch Quant Tetramer Kit-PE (Cat. TB-7400-K1, MBL International) per manufacturer instructions. Briefly, 10 μg of peptide together with 50 μL of the tetramer reagent and 1 μL of peptide exchange factor were incubated at room temperature for 5-6 hours and used to stain cell populations of interest. Clone KT15 of an anti-CD8 antibody (Cat. D271-A64, MBL International) was used to identify CD8^{+} T cells of interest as this clone does not interfere with tetramer binding.

2.7.3.7 Intracellular cytokine staining

OT-1 cells were prepared and incubated with ovalbumin-expressing tumors as described above in the LAMP-1 assay. For some experiments OT-1 cells were instead left unstimulated (DMSO) or treated with PMA 1 μg/mL + ionomycin 1 μM as a supraphysiologic stimulus. In all cases, T cells underwent a 5-6 hour incubation period in the presence of DMSO or splicing modulators at the indicated concentrations, and with brefeldin A and monensin present for the entire duration. Cells were subsequently washed, stained for surface markers, and then fixed/permeabilized for intracellular staining of the indicated cytokines according to manufacturer instructions (BD Biosciences).

2.7.3.8 Western blotting

Western blotting was performed as per standard techniques. Anti-RBM39 (Atlas Antibodies, Cat. HPA001591 or Bethyl laboratories, Cat. A300-291A) were used to detect RBM39 degradation. ADMA and SDMA levels were determined using antibodies from Cell Signaling Technologies (Cat. 13222S and Cat. 13522S). Actin antibody (clone AC-15) was obtained from MilliporeSigma (Cat. A5441-.2ML). Densitometry of RBM39 and actin loading control was performed using ImageJ software in order to calculate RBM39 degradation IC_{50} values.

2.7.3.9 Therapeutic treatment with splicing compounds and anti-PD1

Animals were subcutaneously engrafted on bilateral flanks with tumor cells (MC38 $1x10^6$, B16-F10 $0.5x10^6$ and LLC $0.25x10^6$ cells unless otherwise specified) on day 0, and treated continuously with splicing inhibitors (MS-023 50 mg/kg i.p., indisulam 25 mg/kg i.v. or vehicle) daily for 5 of 7 weekly days starting from day +3 of tumor challenge. Indisulam was obtained from MilliporeSigma (Cat. SML1225-25MG) and MS-023 in sufficient quantities for *in vivo* studies was synthesized by the authors as previously described (Eram et al., 2016). For *in vivo* formulation,

indisulam was dissolved in sterile DMSO at 50 mg/mL and this was combined in a 1:20 ratio with 15% 2-Hydroxypropyl-β-cyclodextrin (Sigma. Cat. H107-100G) in sterile water (w/v) and filtered through a 0.45 μM filter to yield a final solution of 2.5 mg/mL. For *in vivo* formulation, 62.5 mg of MS-023 was dissolved in 563 μl of 1-methyl-2-pyrrolidinone (NMP, Sigma. 328634-1L), diluted with 2.257 mL of 20% Captisol in sterile water (w/v, SelleckChem Cat. S4592) and further combined with 2.257 mg of polyethylene glycol 400 (PEG-400, Sigma Cat. PX1286B-2), and 6.21 mL of PBS, mixed by vortexing and sterile filtered to yield a solution of 5.5 mg/mL. Mice were weighed weekly for weight-based drug dosing. Animals were treated with 250 μg of anti-PD1 flat dose (clone RMP1-14, BioXCell Cat. BE0146) or PBS i.p. starting on day +7 and twice weekly thereafter for a total of five doses.

2.7.3.10 In vivo T cell or NK cell depletion

For depleting T cells, mice were treated with simultaneous anti-CD4 (clone GK1.5, BioXCell Cat. BE0003-1) together with anti-CD8 (clone 2.43, BioXCell Cat. BE0061) versus PBS control, at days −7, −4, +4, and +7 relative to tumor challenge on day 0. Each depleting antibody was administered i.p. at 0.5 mg per dose. $0.5x10^6$ B16-F10 which were treated *in vitro* with indisulam at 1 μM or DMSO for 96 hours were engrafted subcutaneously on the flanks of animals receiving T cell depletion or PBS control. For NK cell depletion, an identical experimental schedule and dose using clone PK136 (BioXCell Cat. BE0036) was utilized. To verify T cell depletion, CD4 clone H129.19 (Biolegend Cat. 130310), CD8 clone 53-5.8 (Biolegend Cat. 140410) were used. NKp46 (Biolegend Cat. 137608) was used to verify NK cell depletion.

2.7.3.11 CFSE adoptive T cell transfer and splicing modulator treatment

Splenic T cells were obtained from naive B6 or CD45.1 donors by CD5 positive selection (Miltenyi Biotec, Cat. 130-049-301), labeled with CellTrace CFSE (ThermoFisher Cat. C34570) at 10 μM, and adoptively transferred by tail vein injection into lethally irradiated B6, BALB/c, or LP/J recipients, with 10^7 labeled donor T cells transferred per recipient. All recipients were irradiated on day −1 prior to adoptive T cell transfer with 7 Gy as a single fraction and continuously received splicing inhibitor drugs or vehicle control at the indicated doses, from day −1 until day of sacrifice, with the initial dose of drug at least 4 hours after lethal irradiation. Recipients were treated with each splicing modulatory compound at doses used in prior studies that result in target engagement *in vivo* (Fong et al., 2019;Wang et al., 2019). Indisulam and MS-023 were solubilized for *in vivo* administration and animals were treated daily as above. Pladienolide B (Tocris, Cat. 6070) and GEX1A (Cayman Chemicals, Cat. 25136) were both dissolved in vehicle (10% ethanol and 4% Tween-80 in sterile PBS) and administered i.p., with pladienolide B dosed at 10 mg/kg every other day, and GEX1A dosed at 1.25 mg/kg every four days. For *in vivo* use, EPZ015666 was dissolved in DMSO and solubilized in 0.5% methylcellulose in water to 20 mg/mL; animals were treated daily with 200mg/kg by oral gavage.

2.7.3.12 Anti-CD3/CD28 T cell activation

Plates were coated with 10 μg/mL anti-CD3 (clone 145-2C11, Biolegend Cat. 100302) and 2 μg/mL anti-CD28 (clone 37.51, Biolegend Cat. 102102) in PBS overnight at 4°C and washed twice with cold PBS prior to use. CFSE-labeled CD5-selected splenic T cells from naive C57BL/6J mice were obtained identically as for adoptive cell transfer, and $5x10^4$ cells incubated with coated plates in the presence of splicing inhibitor drugs at the indicated concentrations, followed by analysis by standard flow cytometry on day 3. Of note, for RNA-seq analyses, T cells were not labeled with CFSE, and underwent activation for 4 days (96 hours) in the presence of various splicing modulator

drugs to harmonize experimental conditions with RNA-seq analyses of tumors treated with splicing inhibitors. For the RNA-seq experiments only, T cells in all conditions were also incubated with IL-2 at 50U/mL to maximize viability and yield.

2.7.3.13 Mixed leukocyte reaction

RBC lysed bone marrow obtained from the femurs and tibias of C57BL/6 or β_2 microglobulin deficient mice (Jackson Laboratories Cat. 2087) were cultured with mouse IL-3 (PeproTech Cat. 213-13) and mouse FLT3 ligand (PeproTech Cat. 250-31L) both at 10 ng/mL each in RPMI + 10% FCS for 7 days to generate bone marrow derived dendritic cells. Separately, 10^7 MC38 treated with splicing inhibitors versus DMSO or expressing chicken ovalbumin were harvested, washed and resuspended in sterile PBS, and subjected to five cycles of rapid freeze-thaw (alternating between 37°C and dry ice/acetone) to generate a cell lysate. After brief centrifugation at 100xg, the soluble fraction in PBS was added to bone marrow derived DCs and left to incubate overnight for antigen phagocytosis in the presence of LPS (ThermoFisher Cat. 00-4976-93). DCs were subsequently washed three times to remove cell-free lysates and LPS and incubated in a 1:1 ratio with CFSE-labeled B6 splenic T cells (10^5 stimulators with 10^5 responders) as described above. The MLR was analyzed at day 5 by flow cytometry.

2.7.3.14 M3434 methylcellulose colony assay

25,000 red blood cell-lysed bone marrow mononuclear cells from C57BL/6 mice were plated in duplicates or triplicates in each well of a non tissue-culture treated 6 well plate with M3434 methylcellulose media in the presence of splicing drugs at the indicated concentrations as per manufacturer's instructions (StemCell Technologies, Cat. 03434) and incubated for seven days prior to quantification of colonies by manual microscopy.

2.7.3.15 Intracellular flow cytometry

Cells were fixed with 2.1% formaldehyde in PBS for 10 minutes at 37°C, washed and permeabilized with ice-cold 90% methanol for 30 minutes, and washed prior to staining. If required, cell surface staining was performed after fixation but prior to permeabilization. For some experiments, intracellular staining was performed using the eBioscience Foxp3 transcription factor staining buffer set (ThermoFisher Cat. 00-5523-00) or reagents for intracellular cytokine staining (BD Cytofix/Cytoperm, Cat. 554714, and BD Perm/Wash, Cat. 554723) as per manufacturer's instructions.

2.7.3.16 Histology

Animal tissues were fixed in 4% paraformaldehyde, decalcified (for bone), dehydrated and paraffin embedded. Blocks were sectioned and stained with hematoxylin and eosin or anti-CD8. Images were acquired using an Axio Observer A1 microscope (Carl Zeiss, Oberkochen, Germany) or scanned using an Aperio AT slide scanner (Leica Biosystems, Buffalo Grove, IL). Automated quantification of infiltrating $CD8^+$ T cells was performed using HALO software (Indica labs, Albuquerque, NM). Pathologic evaluation of immune-related tissue toxicities was performed in a blinded fashion by one of the authors who is a trained pathologist (Ben Durham, MD).

2.7.3.17 Cellular fractionation for RNA sequencing

Nuclear and cytoplasmic cellular fractions were isolated from B16-F10 cells using reagents from Active Motif (Cat. 25501) as per manufacturers' instructions, with the exception of RNA isolation and purification from each fraction using the QIAgen RNeasy Mini kit.

2.7.3.18 RNA sequencing

Bulk lung and colon were homogenized using a QIAGEN TissueRuptor. For all tissues and cell types, RNA was extracted using an RNeasy kit (QIAGEN, Frederick, MD) and quantified using a NanoDrop 8000 (ThermoFisher Scientific). A minimum of 500 ng of high-quality RNA (as determined by Agilent Bioanalyzer) per sample or replicate was used for library preparation. Poly(A)-selected, strand-specific (dUTP method) Illumina libraries were prepared with a modified TruSeq protocol and sequenced on the Illumina HiSeq 2000 (~100M 2x101 bp paired-end reads per sample or replicate).

2.7.3.19 RNA-seq data analysis

RNA-seq analysis was performed as previously described (Dvinge et al., 2014). Briefly, FASTQ files were mapped using RSEM version 1.2.4 (Li and Dewey, 2011) (modified to call Bowtie) (Langmead et al., 2009) with option '-v 2′) to mouse or human transcriptome annotations built using transcript information from Ensembl v71.1 (Flicek et al., 2013), UCSC knownGene (Meyer et al., 2013), and MISO v2.0 (Katz et al., 2010). Reads that did not align at this step were then mapped using TopHat version 2.0.8b (Trapnell et al., 2009) to the mouse (GRCm38/mm10) or human (GRCh37/hg19) genome assemblies, as well as to a database of annotated splice junctions as well as all possible new junctions consisting of linkage between each co-linear annotated 5′ and 3′ splice sites within individual genes. Aligned reads from these two mapping steps were merged to generate final BAM files for all subsequent analyses.

Gene expression estimates were computed using RSEM (performed concordantly with the RNA-seq read mapping procedure described above). Significantly differentially expressed genes were defined as those meeting the follow criteria: minimum expression of 1 transcript per million

(TPM); minimum fold-change of 1.5 (log_2 scale); $p \leq 0.05$ (computed using an unpaired, two-sided t test comparing replicate groups for a given treatment and cell line) or a minimum Bayes factor of 100 (computed using Wagenmakers's Bayesian framework (Wagenmakers et al., 2010) for the median of gene expression and associated read counts over replicates for a given treatment and cell line). Splice junction-spanning reads were filtered to require a minimum overhang of 6 nt. MISO v2.0 was used to quantify all expression of isoforms arising from exon skipping (cassette exons), competing 5′ splice site selection, competing 3′ splice site selection, and annotated intron retention. Quantification of constitutive intron retention, where constitutive introns were defined as those whose 5′ and 3′ splice sites were never joined to other splice sites in the knownGene annotation, was calculated as previously described (Hubert et al., 2013) using reads with a minimum of 6 nt overhang in both the exon and intron. Events were considered significantly differentially spliced if they met the following criteria: a minimum of 20 identifying reads (reads which align only to one, but not both, isoforms constituting a given splicing event) in each sample; a minimum of 10% change (absolute scale) in isoform ratio or minimum fold-change of 2 (log_2 scale) in absolute isoform ratio; $p \leq 0.05$ (computed using an unpaired, two-sided t test comparing replicate groups for a given treatment and cell line) or a minimum Bayes factor of 5 (computed using Wagenmakers's Bayesian framework) (Wagenmakers et al., 2010) for the median of isoform ratios and distinguishing read counts over replicates for a given treatment and cell line). All data parsing, statistical analyses, and data visualization were performed using the R programming environment with Bioconductor (Huber et al., 2015).

2.7.3.20 MHC I immunoprecipitation, peptide purification, and mass spectrometry

Peptide-MHC complexes were isolated as previously described (Abelin et al., 2017), with the following modifications: anti-mouse H-2D^b (clone B22-249.R1, CedarLane laboratories, Cat. CL9001AP) or H-2K^b (clone Y-3, BioXCell Cat. BE0172) non-covalently linked to GammaBind Plus Sepharose beads were co-incubated with soluble lysates overnight. After washing with lysis buffer twice, 10mM Tris pH 8 twice, and dH_2O twice, the peptides were desalted on C18 StaGE tips (Ishihama et al., 2006) (Pierce, Cat. 87784) and eluted using a 20%–35%-50% acetonitrile stepwise gradient. Eluted fractions were dried using a SpeedVac vacuum concentrator and stored until mass spectrometry. For B16-F10, cells in all experimental conditions were treated with 10U/mL mouse IFNγ (PeproTech Cat. 315-05) for 48 hours prior to cell harvest and immunoprecipitation to upregulate surface MHC I expression.

2.7.3.21 Mass spectrometry

Desalted, dried samples enriched for MHC peptides were resolubilized in 8uL 0.1% TFA and 3uL were loaded onto a packed-in-emitter 12cm/75um ID/3um C18 particles column (Nikkyo Technos Co., Ltd. Japan). Peptides were eluted using a gradient delivered at 300nL/min increasing from 2% Buffer B (0.1% formic acid in 80% acetonitrile) / 99% Buffer A (0.1% formic acid) to 30% Buffer B / 70% Buffer A, over 70 minutes (EasyLC 1200, Thermo Scientific). All solvents were LCMS grade (Optima, Fisher Scientific). MS and MS/MS (HCD type fragmentation) experiments were performed in data dependent mode with lock mass (m/z 445.12003) using Fusion Lumos (Thermo Scientific). Precursor mass spectra were recorded from m/z 300-1500 m/z range at 60,000 resolution. 1, 2 and 3 positive charges were selected for fragmentation experiments. MS/MS spectra were recorded at 30,000 resolution and lowest mass set at m/z 110. For MS/MS acquisition, injection time was set to maximum 100 ms with an Auto Gain Control setting of 5e4. Normalized collision energy was set to 30. All experiments were recorded in FT-mode.

2.7.3.22 Proteome creation

Gene and isoform annotations were created as described in RNA-seq data analysis. This merged transcript annotation, as well as the RefSeq annotations of the human and mouse genomes, was used to create the four distinct proteomes described in the main text as follows.

Isoforms were computationally translated into proteins and digested into unique 8-14-mers. Isoforms were translated into proteins "conservatively," in the sense that the translation was performed assuming that the annotated start codons were used and no stop codon readthrough or internal translation initiation occurred (e.g., generally only the first portion of a retained intron would be translated until an in-frame premature termination codon was encountered, after which translation was assumed to halt). The binding affinity for each resulting peptide to the relevant MHC alleles was then predicted using NetMHCpan v4.0 (Jurtz et al., 2017). Each peptide was annotated with relevant information about its encoding transcript, including parent gene, parent isoform(s), differential gene and/or isoform expression (if relevant), position within parent transcript, unique assignment to one versus two or more isoforms of the originating splicing event (if relevant), etc.

Four distinct, custom proteomes for subsequent spectra mapping were created (illustrated in Figure 5B). (1) "full-length proteome," created using peptides arising from all unique full-length isoforms. (2) "predicted binders," created by further restricting to unique 8-14-mers that had a NetMHCpan 4.0 percentile rank < 2 (the recommended cutoff for binders from NetMHCpan 4.0). Two versions of this proteome were created, one including only those isoforms derived from differentially retained constitutive introns based on the RNA-seq data, and one including all isoforms derived from constitutive intron retention (constituting an increase in unique 8-14-mers of ~28%). Analyses used the complete (latter) proteome unless otherwise indicated. (3) "predicted

binders + spiked non-binders," created by augmenting the "predicted binders" proteome with peptides that were predicted to not bind the relevant MHC alleles with high-confidence, defined as having NetMHCpan percentile rank > 90, with the number of such non-binders chosen such that they comprised 10% of the final proteome after adding to the "predicted binders" proteome. (4) "filtered predicted binders," created by further filtering the "predicted binders" proteome by restricting to peptides arising from genes that were significantly differentially expressed or isoforms that were significantly differentially spliced in indisulam-treated versus DMSO-treated samples, defined based on the RNA-seq analysis for the corresponding cell lines.

2.7.3.23 Peptide identification from mass spectrometry data

Mass spectra from all MHC immunoprecipitations were analyzed using Proteome Discoverer v2.4.1.15, with the following workflow. Spectra from each replicate were searched against each distinct proteome (described above) as follows. For each proteome, searches were performed with no enzyme specificity, precursor mass tolerance of 10 ppm, and fragment mass tolerance of 0.6 Da. Oxidation (+15.995 Da), phosphorylation (+79.966 Da), and deamidated (+0.984 Da) dynamic modifications were included, in addition to N-terminal glutamate to pyro-glutamate (−17.027 Da). False discovery rate (FDR) estimation was performed computationally using the Percolator software. Peptides reaching the 5% FDR threshold were retained for downstream analyses. For the "full-length" proteome, identified peptides were further restricted to those of length 8-14 amino acids before being used as input for subsequent analyses. For the "predicted binders," "predicted binders + spiked non-binders," and "filtered predicted binders" proteomes, peptides corresponding to subsequences of the sequences in the input proteomes were removed before the identified peptides were used for subsequent analyses.

2.7.3.24 Candidate neoepitope identification

As described in the main text, two distinct groups of candidate neoepitopes were selected for subsequent immunization experiments. The first group was based on the intersection between mass spectrometry analyses and RNA-seq analyses. Peptides were first identified using the mass spectrometry analysis described above. These peptides were then restricted to the set of indisulam-specific peptides, where an indisulam-specific peptide was defined as a peptide that was identified in one or more indisulam-treated samples, but not recovered in any DMSO-treated samples. These indisulam-specific peptides were then filtered to retain only those peptides arising from alternative isoforms that were significantly differentially spliced in indisulam-treated versus DMSO-treated cells, and subsequently additionally filtered to require (1) isoform specificity and (2) appropriate direction of differential splicing, with those two criteria defined as follows. (1) An isoform-specific peptide was defined as a peptide which arose exclusively from one isoform associated with a given splicing event (e.g., a peptide from a retained intron event is isoform-specific if it arises from translation of the intronic portion of the unspliced mRNA, or if it arises from translation of the exon-exon junction within the spliced mRNA). This definition means that differential splicing of a given event is predicted to alter levels of the isoform encoding an isoform-specific peptide, and therefore likely similarly alter abundance of the isoform-specific peptide itself. (2) Peptides that exhibit appropriate direction of differential splicing are those isoform-specific peptides which are specifically encoded by differentially spliced isoforms that are promoted by indisulam treatment (e.g., the encoding isoform is present at higher levels in indisulam-treated versus DMSO-treated cells). Isoform-specific peptides were only used for subsequent immunization experiments if their parent isoform was more prevalent in the indisulam treatment, signifying that the peptide is

expected to be more abundant in indisulam-treated cells. These criteria yielded 72 peptides, which were subsequently tested in immunization experiments.

The second group of peptides used for immunization experiments was derived by combining evidence from RNA-seq analyses and MHC I binding predictions. This set of peptides was defined using the same criteria described above for the first set (derived by intersecting predictions from mass spectrometry analyses as well as RNA-seq analyses), but without the requirement that peptides be detected as indisulam-specific epitopes via MHC I mass spectrometry. To compensate for the fact that direct protein-level detection was not required, a stringent predicted MHC I binding threshold of rank < 0.5 (the NetMHCpan recommended threshold for strong binders) for one or more relevant alleles was applied (versus the more lenient threshold of rank < 2 used for other, mass spectrometry-based predictions and analyses). Peptides were additionally restricted to those of lengths between 8 and 11 amino acids, as such lengths are preferred by the studied alleles. The final set of peptides used for subsequent immunization experiments was then derived by additionally requiring that peptides be isoform-specific; arise from genes with expression > 5 TPM in corresponding indisulam-treated samples (in order to favor peptides from relatively highly expressed genes); and have a difference in isoform ratio > 20% in indisulam-treated versus DMSO-treated samples, and isoform ratio < 25% in DMSO-treated samples (in order to restrict to peptides that were associated with more dramatic splicing changes). These criteria yielded 39 peptides, which were subsequently tested in immunization experiments.

2.7.3.25 Peptide synthesis

Experimental peptides were individually custom synthesized via the solid-phase method by GenScript (Piscataway, NJ), with standard removal of trifluoracetic acid and replacement with

hydrochloride, purified to > 98% by HPLC, and lyophilized for storage. Peptides were reconstituted in DMSO at 10 mg/mL and frozen at −80C until use.

2.7.3.26 RMA-S peptide H-2 stabilization assay

RMA-S cells were maintained under standard conditions in RPMI + 7.5% FCS for expansion. H-2 stabilization experiments were performed as previously described (Ross et al., 2012). Briefly, RMA-S were exposed to 31°C and 5% CO_2 conditions overnight, incubated with peptides of interest for 30 minutes at 31°C, and then returned to 37°C and 5% CO2 for three hours prior to cell surface staining for H-2K^b (clone AF6-88.5) and H-2D^b molecules (clone KH95) and standard flow cytometry analysis. For Figures 5N–5Q, spike-in negative control peptides were as follows for each experimental peptide – Hus1: PPSGRALLW; Zpf512: QKPKGSQRG; D14Abb1e: LKPQAKRSK; Poldip3: GESWQEKER

2.7.3.27 TiterMax immunization

Unless otherwise specified, 10 μg of peptide was emulsified with TiterMax Classic (TiterMax Corp., Norcross, GA) and injected into the hocks of anesthetized animals. On day +7 after challenge, draining lymph nodes were collected and CD8$^+$ T cells purified by magnetic selection (Miltenyi Biotec, Cat. 130-117-044).

2.7.3.28 IFNγ ELISpot

CD8$^+$ T cells from TiterMax immunized animals were cultured overnight with 20 U/mL mouse IL-2 (PeproTech, Cat. 212-12) and plated at 10^5 per well in combination with $3x10^5$ T cell depleted syngeneic splenocytes which had been loaded with 100 μg/mL of peptides of interest for 18 hours. PMA 1 μg/mL + ionomycin 500 ng/mL stimulation of T cells served as positive control.

In some experiments, in lieu of peptide-loaded splenocytes, instead ovalbumin-expressing B16-F10 cells or B16-F10 cells treated with DMSO or indisulam 1 μM for 96 hours were stimulated overnight with IFNγ 100U/mL for the last 24 hours of cell culture. Such cells were then non-enzymatically harvested, washed repeatedly to remove IFNγ, and irradiated to 60 Gy from a ^{60}Co source to inhibit growth and further upregulate MHC I. Tumor cells thus generated were counted and incubated with $CD8^+$ T cells at identical ratios as for splenocytes (10^5 $CD8^+$ T cells + $3x10^5$ melanoma cells). IFNγ ELISpot was performed as per manufacturer's instructions (BD Biosciences, Cat. 551083). Spots were imaged and quantified on an Immunospot® analyzer (Cellular Technology Limited, Cleveland, OH).

2.7.3.29 B16-F10 co-culture cytotoxicity assay

B16-F10 cells were harvested, counted, and plated at 10^4 per well in the presence of 100U/mL IFNγ overnight to upregulate MHC I. After washing, peptides were loaded onto tumor cells at 100 μg/mL, and 10^6 $CD8^+$ T cells from TiterMax immunized animals were added to the tumor cells. 50 U/mL mouse IL-2 was added to this co-culture of tumor cells + $CD8^+$ T cells, which was incubated for three days. After washing to remove free (detached) B16-F10 and T cells, viable B16-F10 were harvested, stained (to exclude T and other hematopoietic cells) and absolute cell numbers enumerated via flow cytometry using counting beads according to the manufacturers' instructions (ThermoFisher Cat. C36950).

2.7.3.30 Quantification and statistical analysis

All data summarization, visualization, and statistical analysis were performed using GraphPad Prism v9.0 (GraphPad Software, San Diego, CA) or in the R programming language. Details for statistical procedures, including statistical test used, number of replicates, definition of center, and

definition of error bars are found within the figure legends. Unless otherwise noted in the text, n represents biological replicates of the sample type (e.g., individual tumors, independent cell cultures, etc.) indicated in the figure legend. The normality of data was assessed using a Shapiro-Wilk test. If data were normally distributed, a parametric test (e.g., unpaired, two-sided t test) was used to test for significant differences between groups; otherwise, a non-parametric test (e.g., Wilcoxon rank-sum test) was used, as indicated in the figure legends. Differences between groups were considered significant if p was less than 0.05. No methods were used for sample randomization or sample size estimation and no data were excluded from analysis.

2.8 ACKNOWLEDGEMENTS

We thank Phil Gafken and Lisa Jones for mass spectrometry advice. S.X.L. is supported by a Parker Institute for Cancer Immunotherapy (PICI) Bridge Scholar award, the NIH/NCI (K08 CA245242-01), and the Leukemia & Lymphoma Society (5492-20). E.D.N. was supported in part by the NIH/NCI (T32 CA009657). J.D.T. is a Washington Research Foundation postdoctoral fellow. J.D.W. is funded through NIH/NCI Cancer Center (P30 CA008748), Ludwig Collaborative and Swim Across America Laboratory, and PICI. O.A.-W. and R.K.B. were supported by the Edward P. Evans Foundation, NIH/NCI (R01 CA251138), and NIH/NHLBI (R01 HL128239). O.A.-W. is supported in part by the NIH/NCI (R01 CA242020) and Henry and Marilyn Taub Foundation for MDS Research. R.K.B. was supported in part by the NIH/NIDDK (R01 DK103854) and NIH/NHLBI (R01 HL151651). R.K.B. is a scholar of the Leukemia and Lymphoma Society (1344-18). R.E.T. is supported by the NIH/NIGMS (R01 GM123741) and the Walther Cancer Foundation through the Harper Cancer Research Institute at Notre Dame.

Computational studies were supported by FHCRC's Scientific Computing Infrastructure (ORIP S10 OD028685).

2.9 Author Contributions

S.X.L., E.D.N., J.D.T., O.A.-W., and R.K.B. designed the study. A.X., C.E., D. Cui, M.S., and H.C. performed drug treatments. E.D.N. and J.D.T. performed proteomic and RNA-seq analyses. S.X.L. and J.D.T. performed analyses of biological data. S.X.L., M.G., D. Cui, C.E., M.S., and H.C. performed peptide immunizations. S.X.L., E.S., and H.M. performed mass spectrometry. S.X.L. and A.X. performed in vitro drug studies. Y.S., J.L., J.J., M.C.R., and R.E.T. generated chemicals. S.X.L., J.D.T., and A.M.G. generated B2m KO cells. B.H.D. and J.D.T. analyzed histology. B.R., M.G., D.A.K., B.G., Y.E., S.J.H., A.C., A.G., D.Z., E.W., B.L., H.S., D. Chowell, J.W., T.M., and L.A.D. provided critical reagents and technical advice. S.X.L., E.D.N., J.D.T., O.A.-W., and R.K.B. wrote the manuscript, with input from all authors.

2.10 Declaration of interests

O.A.-W. has served as a consultant for H3B Biomedicine, Foundation Medicine, Merck, Prelude Therapeutics, and Janssen, and is on the scientific advisory board of Envisagenics, Pfizer Boulder, and AIChemy. O.A.-W. has received prior research funding from Loxo Oncology and H3 Biomedicine unrelated to this work. S.X.L. has served as a consultant (uncompensated) for PTC Therapeutics. B.R. has served as a consultant for Bayer and Roche. D.Z. reports clinical research support to his institution from Astra Zeneca, Plexxikon, and Genentech and personal/consultancy fees from Merck, Synlogic Therapeutics, Tesaro, Bristol Myers Squibb (BMS), Genentech, Xencor, Memgen, Calidi Biotherapeutics, and Agenus. L.A.D. is a member of the board of directors of Personal Genome Diagnostics (PGDx) and Jounce Therapeutics. L.A.D. is a

compensated consultant to PGDx, 4Paws (PetDx), Innovatus CP, Se'er, Delfi, Kinnate, and Neophore. L.A.D. is an uncompensated consultant for, but has received clinical trial support from, Merck. L.A.D. holds equity in PGDx, Jounce, Se'er, Delfi, Kinnate, and Neophore and divested equity in Thrive Earlier Detection in 2021. His spouse holds equity in Amgen. J.D.W. is a consultant for Amgen, Apricity, Arsenal IO, Ascentage Pharma, AstraZeneca, Astellas, Boehringer Ingelheim, BMS, Chugai, Dragonfly, F Star, Eli Lilly, Georgiamune, IMVAQ, Merck, Polynoma, Psioxus, Recepta, Trieza, Truvax, Sellas, and Werewolf Therapeutics. J.D.W. has grant/research support from BMS and Sephora. J.D.W. reports equity in Tizona Pharmaceuticals, Imvaq, Beigene, Linneaus, Apricity, Arsenal IO, and Georgiamune. T.M. is an inventor on patents involving the use of anti-PD-1 antibodies. T.M. is a consultant for Immunos Therapeutics and Pfizer. T.M. is a cofounder of and equity holder in IMVAQ. T.M. receives research funding from BMS, Surface Oncology, Kyn Therapeutics, Infinity Pharmaceuticals, Peregrine Pharmaceuticals, Adaptive Biotechnologies, Leap Therapeutics, and Aprea Therapeutics. S.X.L., O.A.-W., and R.K.B. are inventors on a patent application submitted by FHCRC related to this work.

Chapter 3. IMMUNE PROFILING AND NEOANTIGEN IDENTIFICATION IN CANCERS WITH SF3B1 MUTATIONS

This research is unpublished. K562 cell line engineering, MHC-pulldowns, and mass spectrometry were performed by Won Jun Kim and Erich Sabio. Heeju Ryu assisted with T cell expansions and Laura Islas assisted with the mass cytometry panel design and development. Patient samples were acquired by Omar Abdel-Wahab. Study design and data analysis were supervised by Evan Newell and Robert Bradley. The remaining work described here, including study design, T cell expansion, flow and mass cytometry experiments, and analysis of RNA-seq, mass spectrometry, flow cytometry, and mass cytometry data represent my contribution to the work.

3.1 INTRODUCTION

Splicing factors are recurrently mutated in many types of cancer, including both hematopoietic diseases and solid tumors, such as uveal melanoma and breast cancer (Dvinge et al., 2016). Mutations in splicing factors are often gain-of-function mutations that lead to characteristic patterns of mis-splicing and in turn, the introduction of novel protein isoforms. Although some individual mis-spliced isoforms have been implicated in the development and progression of cancer (Inoue et al., 2019, Lieu et al., 2022, Choudhary et al., 2022), the overall effect of the widespread mis-splicing caused by these mutations on the immune response is still not well understood. However, as demonstrated by the work in Chapter 2, cytotoxic T cells can recognize and respond to neoantigens arising from novel splicing changes. This knowledge suggests that splicing factor mutations may introduce numerous neoantigens that would make these cancers a prime target for immune recognition and destruction, yet the frequency and nature of these mutations instead imply that these are driver mutations in cancer. Here we aim to understand the nature of this paradox by studying the immune response and neoantigen load of the most frequently mutated splicing factor, SF3B1, in myelodysplastic syndromes (MDS) and acute myeloid leukemia (AML).

SF3B1 is mutated in 20-34% of patients with MDS (Haferlach et al., 2014; Bacher et al., 2015), 2-5% of patients with AML (van der Werf et al., 2021; Malcovati et al., 2011), and 15-20% of patients with uveal melanoma (Dvinge et al., 2016), among other cancers. *SF3B1* mutations alter splicing patterns in a characteristic manner by using cryptic 3’ splice sites, and introduced isoforms are frequently subject to nonsense-mediated decay (Alsafadi et al., 2016). Although studies of immune impacts of these mutations are still limited, these mutations have recently been shown to increase innate immune signaling in MDS and AML through overexpression of an

IRAK4 isoform (Choudhary et al., 2022), which may contribute to the disease progression and abnormal inflammatory response. Additionally, a study using a similar approach identified shared neoantigens in SF3B1-mutant uveal melanoma (Bigot et al., 2021), a promising sign for our study, which focuses instead on their impact in MDS and AML.

Many patients with MDS progress to AML, as these disorders are related in their disruption of myeloid progenitor cells. AML is known to evade the immune system in numerous ways, including the loss of MHC (Jan et al., 2019) and the upregulation of checkpoint inhibition signals such as PD-L1 (Toffalori et al., 2019). Additionally, characterization of T cells in AML patients has revealed increased T cell exhaustion and apoptosis, in addition to the expansion of regulatory T cells (Curdi et al., 2007; Le Dieu et al., 2009). AML also increases signals affecting the innate immune system by upregulating CD47, an inhibitory signal for macrophages (Majeti et al., 2009). These characteristic signs of immune evasion suggest that as in many other cancers, AML blasts must evolve ways to evade killing from the immune system and suggest that it could be a good target for immunotherapies. To date, there have been various studies exploring the potential of CAR T cells targeting cell surface antigens and the efficacy of immune checkpoint inhibitors, although most are still in pre-clinical or early clinical stages (Vishwasrao et al., 2022; Gómez-Llobell et.al, 2022). Despite work characterizing the immune landscape of AML/MDS as a disease, there has not been a comprehensive characterization of the differences in the immune phenotypes due to *SF3B1* genotype.

The present study begins to address these questions using PBMCs from a cohort of 20 patients diagnosed with AML or MDS. Of these patients, 15 have *SF3B1* K700E mutations while 5 are wild-type (WT) controls. PBMCs from two healthy donors are additionally included as non-dysplastic controls. We developed a mass cytometry panel that profiles 120 MHC-peptide

tetramers and 39 relevant markers of immune-cell phenotype and function in order to extensively characterize these patient samples. Using this cohort, in addition to publicly available RNA-seq and *in vitro* mass spectrometry data, we will address the question of whether splicing changes in cancers with *SF3B1* mutations can be recognized by cytotoxic T cells and how these mutations alter the immune landscape of MDS and AML.

3.2 RESULTS

3.2.1 *SF3B1 mutations incur shared splicing changes encoding predicted neoantigens*

In order to develop a list of top candidate splicing-derived neoantigens, we began by using RNA-seq data from 7 publicly available AML and/or MDS patient cohorts (Tyner et al, 2018; Kim et al., 2015, Pellagatti et al., 2018, Schinke et al., 2015, Ramsey et al., 2013, TCGA). We first identified the nature and magnitude of splicing differences between patients with and without *SF3B1* mutations within each dataset (Figures 1A and 1B). We then translated the RNA isoforms *in silico*, digested the protein sequences using an 8-11 amino acid sliding window, and predicted binding efficiency of each sequence to two common MHC alleles, HLA-A*02:01 and HLA-A*24:02, using NetMHCPan4.0 (Jurtz et al., 2017) (Figure 1C). In the interest of identifying peptides from events that represent shared targets, we filtered to only include events that were differentially spliced in more than one cohort, had a median dpsi of >0.05, and promoted a peptide that was specific to one isoform of a splicing event. In order to increase the likelihood that the events would give rise to bona fide neoantigens, we additionally restricted to splicing events from genes expressed at least 10 TPM, and restricted to events that were minimally or never expressed (<0.1 TPM) in normal tissues from the Illumina body map dataset (Gene Expression Omnibus accession code GSE30611) or in normal bone marrow samples from Madan et al. 2015 (Figure 1D). This resulted in 36 and 59 candidate splicing-derived peptides per allele, respectively. The

majority of these peptides came from alternative 3' splice site selection events (Figure 1E), in concordance with previous studies (Alsafadi et al., 2016). We additionally performed translation and binding affinity prediction for peptides deriving from common *SF3B1* mutations. This resulted in the inclusion of 2 additional epitopes predicted to bind to HLA-A*02:01 arising from the most frequently observed *SF3B1* mutation in AML/MDS, K700E.

3.2.2 *Mass spectrometry identifies MHC-peptides in isogenic, mono-allelic K562 cells*

We were then interested in whether any of the peptide candidates could be identified endogenously using mass spectrometry. Using isogenic wild WT and *SF3B1*-K700E K562 cells, an erythroleukemic cell line that does not endogenously express MHC, we stably introduced HLA-A*02:01 and HLA-A24*02 and then purified and eluted MHC peptides for analysis via LC-MS/MS, a method developed by Abelin et al. 2017 (Figure 2A). We performed spectra searches using a custom proteome developed to include alternative splicing sequences but restricted to predicted binders as described in Chapter 2. We identified 1,891 and 1,114 unique predicted binders in the HLA-A*02:01 and HLA-A*24:02 samples, respectively (Figure 2B). These peptides largely came from moderate to highly expressed genes (Figure 2C). Of these peptides, 230 and 169 peptides were only identified in the *SF3B1*-mutant cells, while the largest group of identified peptides were found in both WT and mutant samples (Figure 2D). Of the peptides identified via mass spectrometry, two were among the top candidates identified by RNA-seq analysis, although neither were identified exclusively in mutant samples (Figure 2E).

3.2.3 *Combinatorial tetramer staining to search for antigen-specific T cells recognizing splicing-derived neoepitopes*

Beyond identifying these peptides as endogenously expressed and presented on MHC, we were interested in whether they could then be recognized and bound by cytotoxic $CD8^+$ T cells. We used a mass cytometry-based combinatorial tetramer staining approach as previously described (Newell et al. 2013) with 10 metal-streptavidin conjugates to allow for the screening of up to 120 peptide-tetramers at once. In addition to the 95 candidate splicing-derived peptides and 2 mutation-derived peptides, 23 known viral neoantigens were included from Epstein-Barr virus (EBV), influenza virus (FLU), herpes simplex virus (HSV), and human cytolomegalovirus (hCMV) as positive controls. This group of 120 peptide-MHCs were assigned to a triple metal coding scheme (Table S2) to create a tetramer cocktail, which we then tested on a healthy donor. We identified populations of antigen-specific T cells recognizing viral neoantigens, including one from hCMV (Figure 3A and Figure S1). We further tested our ability to identify rare populations by using a tetramer enrichment strategy, which improved the yield of antigen-specific cells relative to the pre-enriched sample (Figure 3B).

3.2.4 *Mass cytometry allows for deep immune profiling of patient samples*

In combination with the tetramer cocktail detailed above, we developed an antibody panel to profile PBMCs from patients. This panel includes 39 markers, and was designed to include major lineage markers, known AML/MDS markers, and other phenotypic markers, with an emphasis on those relevant to T cells (Table 3.1). This panel will allow us to profile and compare whole PBMCs from healthy donors to our AML and MDS patient cohort with and without *SF3B1* mutations. In addition to a general understanding of the immune environment of the cancers, this approach also allows for the simultaneous collection of further information about antigen-specific T cells

identified by our tetramer approach. For example, using the healthy donor screened in section 3.2.3, we can further determine that the T cells that responded to the A02-HCMV-2 peptide primarily have central- and effector-memory phenotypes, indicating a prior infection (Figure 3C).

3.2.5 *T cell expansion can help to identify rare antigen-specific T cells populations*

As antigen-specific T cells are often rare, we were interested in our ability to expand the populations in order to obtain TCR sequences. As a proof of concept, we expanded antigen-specific T cells from our healthy donor. We peptide-pulsed our peptides of interest on monocyte-derived dendritic cells and co-cultured with lymphocytes, followed by expansion of lymphocyte populations for two weeks (Figure 4A and S2A). This resulted in the expansion of T cells recognizing peptides in the pool. In an initial test, we used the hCMV peptide that had been identified in Figure 3A as binding a population of $CD8^+$ T cells. After culturing for two weeks, we increased the frequency of these antigen-specific T cells from ~0.1% of $CD8^+$ T cells to 46.1% of $CD8^+$ T cells (Figure 4B). We then tested a pooled stimulation using the control viral antigens, which greatly increased our ability to identify rare antigen-specific cell populations compared to the whole PBMC staining, even prior to any enrichment. In addition to identifying the populations we had seen previously, some new antigen-specific populations, such as A24-EBV-4, were identified in this manner (Figure 4C). We finally tested an expansion using a pool of the SF3B1 splicing-derived peptides and identified a few small populations of antigen-specific cells, which could indicate the potential for expansion of naïve T cells (Figure 4D and S2B). Expanding rare populations in this manner would allow us to sort these cells using fluorescent tetramers, which could enable the identification of specific T cell receptors using TCR sequencing approaches.

3.3 DISCUSSION

Although results are still preliminary, there is an opportunity to further explore the potential for therapeutic approaches targeting transcriptomic changes. Given that we have shown that splicing changes can trigger immune responses in Chapter 2, targeting splicing alterations that are frequently found in cancer may provide a source of targets generalizable to many patients, rather than focusing on a patient's individual mutational landscape. This is particularly valuable in the case of cancers like AML, which has a low mutational burden relative to other cancers. We show here that despite this, patients with *SF3B1* mutations do show stereotyped changes in splicing patterns that are not present in normal tissues and could be a rich source of potential therapeutic targets. This contrast is exemplified in the fact that there were only two predicted binders from the K700E mutation in *SF3B1* itself, while we needed to filter down to only the 95 most promising splicing-derived candidates due to limitations of our tetramer screen size. Additionally, since these downstream splicing effects are caused by driver mutations, they are not subject to the same patient-to-patient variability that accumulated passenger mutations in a cancer can be and should be specific to diseased cells.

Despite evidence that the splicing-derived candidates should be favored in mutant cell lines, only two candidates were identified by mass spectrometry and neither were found exclusively in the mutant samples. Although MHC-peptide mass spectrometry can be useful for identifying true MHC-binding peptides, it is limited by coverage and likely represents an undersampling of the full immunopeptidome. These results indicate that these two peptides are not in fact mutant-specific, but it does not necessarily indicate that they are not useful targets. As our assay is not designed to be quantitative, it is difficult to determine the level of expression of these peptides. It is possible that these could be tumor-associated antigens, where expression is elevated

in cancer tissues but not exclusive to them, such as the well-studied melanoma antigen MART-1. It is also possible that since the cell lines used here are leukemic themselves, that they could be tumor-specific antigens but not exclusive to patients with *SF3B1* mutations, despite elevated mRNA levels. Further investigation using other approaches is warranted. Of additional note, both identified peptides arise from isoforms predicted to be subject to nonsense-mediated decay (NMD), which suggests that even peptides from isoforms predicted to be lowly translated can be presented by MHC and potentially useful targets.

Although the immune landscape of AML has been studied, our cohort of patients with and without *SF3B1* mutations will allow for a closer look at whether there are extracellular immune signatures associated with these mutations. Focusing on T cell markers could illuminate how these cancers escape immune recognition and whether there are distinct mechanisms induced by the splicing alterations themselves. Further, targeting specific splicing-induced neoantigens using tetramers may help determine whether any immune changes are caused by splicing-induced neoantigens or whether they could be the result of other downstream effects of widespread transcriptomic dysregulation. We demonstrated the utility of our method in finding antigen-specific T cells, and we showed that it is possible to further help identify rare populations using antigen-specific expansion. If we are able to find T cells targeting splicing-derived neoantigens, this could be used to inform and develop therapeutics targeting *SF3B1*-mutant cancers, such as peptide vaccination or engineered TCR therapies.

3.4 FIGURES

Figure 3.1. *SF3B1* mutations disrupt splicing and introduce potential neoantigens.

(A) RNA-seq coverage plot illustrating a differential 3' splice site selection event in cancers with (n=325) and without (n=21) *SF3B1* mutations in the BeatAML cohort.

(B) RNA-seq coverage plot illustrating a differential cassette exon inclusion event in cancers with (n=325) and without (n=21) *SF3B1* mutations in the BeatAML cohort.

(C) Schematic depicting *in silico* neoantigen prediction workflow. Blue/red is canonical/novel isoform sequence.

(D) Heat map illustrating the percent spliced in (psi) of the isoform each peptide target is derived from. Each column is a candidate peptide target and each row is a dataset, with status indicated by red (*SF3B1* mutant cancers), blue (*SF3B1* WT cancers), or black (non-cancer tissue).

(E) Bar graph depicting the number of targets selected from different types of mis-splicing events.

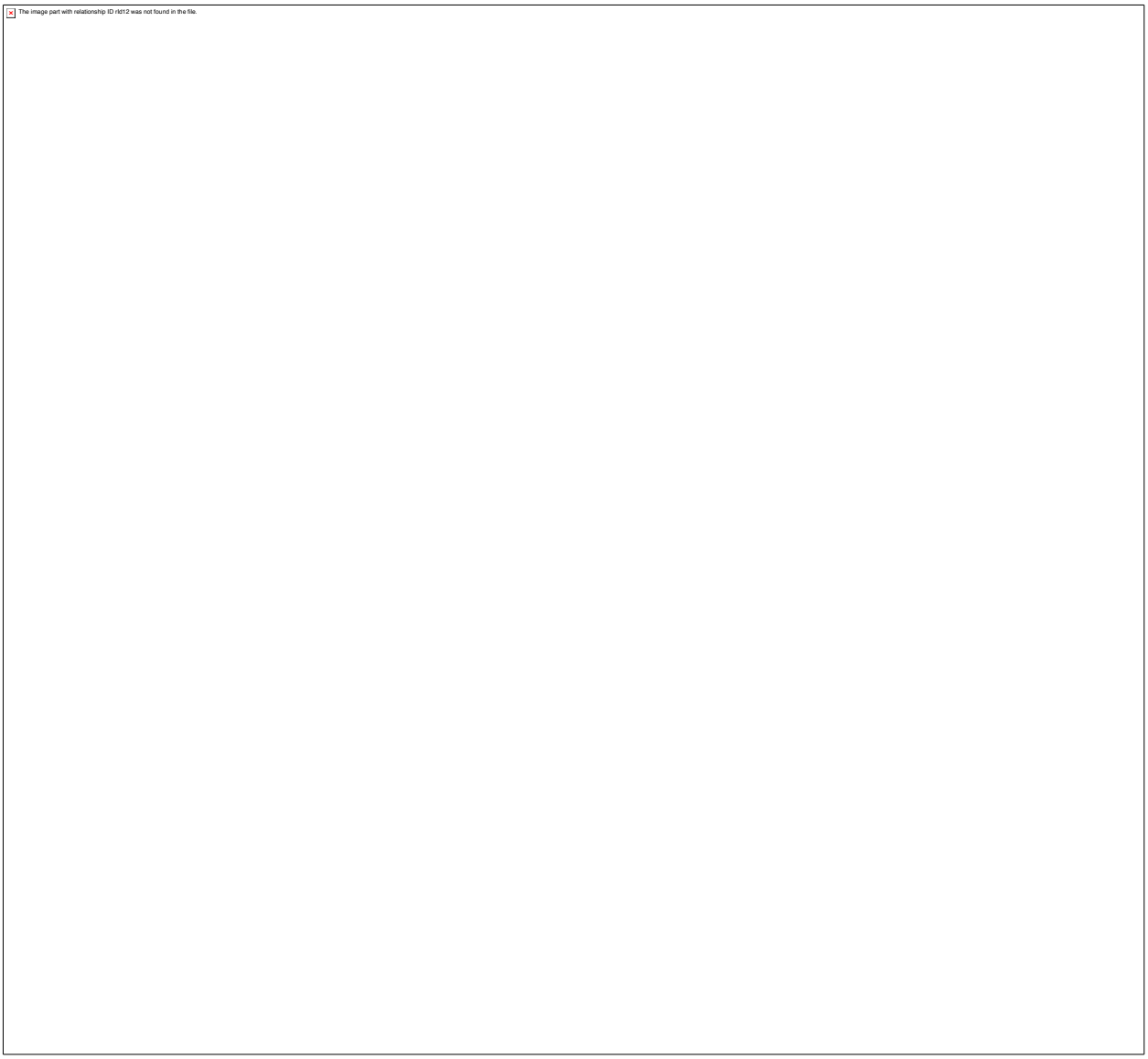

Figure 3.2. MHC-peptides are identified by mass spectrometry.

(A) Schematic of MHC-peptide identification in mono-allelic, isogenic K562 cells by LC-MS/MS.

(B) Bar plot indicating number of peptides identified in mutant *SF3B1* (red) and WT (blue) MHC purifications using a custom proteome of predicted binders. Each dot is a replicate.

(C) Density plots of parent gene expression (in transcripts per million, TPM) for peptides identified from mutant (red, left) and WT (blue, right), compared to the expression of all genes (gray). Identifications from both HLA alleles were merged.

(D) Venn diagrams showing overlap of peptide identifications between WT (blue) and mutant (red) MHC purifications.

(E) Table showing the peptide sequences (left) of the 95 top hits selected in Fig.1 that were identified in any MHC-peptide sample (right).

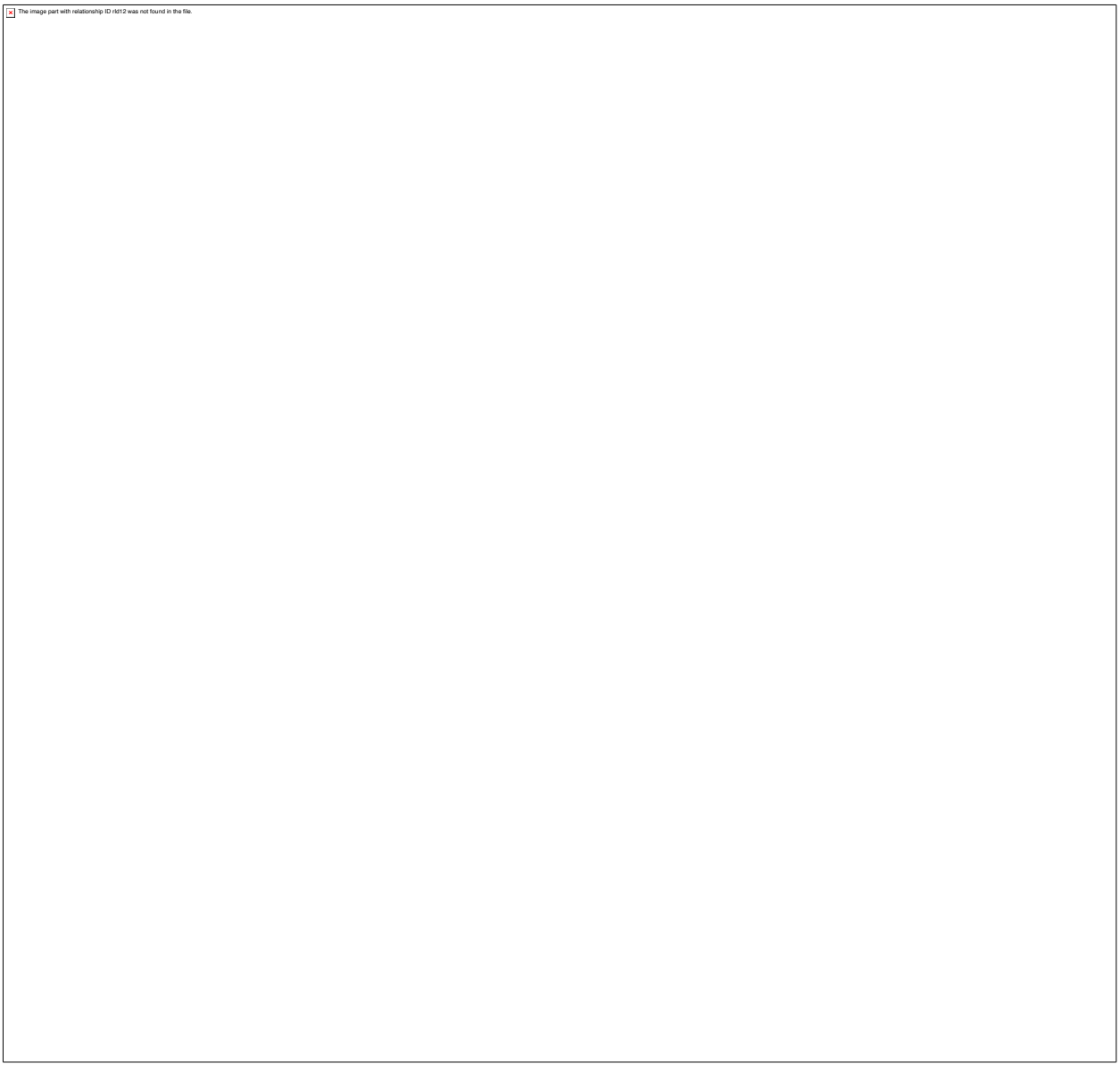

Figure 3.3. Antigen-specific cells can be identified and characterized by mass cytometry.

(A) A02-HCMV-2 tetramer-positive (red) cells overlaid on $CD3^{+}CD8^{+}$ (gray) cells. Channels are metal-tagged streptavidin, depicting triple coding tetramer scheme (157-161-173).

(B) Bar graphs depicting percentage of $CD3^{+}CD8^{+}$ cells identified as tetramer-positive after tetramer deconvolution in pre-enriched, anti-c-myc magnetic bead enrichment, and flow-through samples from a healthy donor.

(C) $CD3^+CD8^+$ cells gated on CCR7 and CD45RA for effector, naïve, effector-memory (EM) and central-memory (CM) phenotypes. Top, all $CD3^+CD8^+$ cells; bottom, A02-HCMV-2 tetramer-positive (red) cells overlaid on all $CD3^+CD8^+$ (gray) cells.

Figure 3.4. Peptide stimulation using monocyte-derived dendritic cells increases the frequency of rare antigen-specific T cells.

(A) Overview of antigen-specific T cell expansion method.

(B) $CD3^+CD8^+$ T cells from A02-HCMV-2 peptide stimulated expansion in same healthy donor as Fig. 3. Gating indicates cells positive and negative for A02-HCMV-2 tetramer (labeled with 159-tagged streptavidin).

(C) Bar graphs depicting percentage of $CD3^+CD8^+$ cells identified as tetramer-positive after tetramer deconvolution in pre-enriched, anti-c-myc magnetic bead enrichment, and flow-through samples from a donor expansion using a pool of all viral control peptides.

(D) A02-ABCB7-076 tetramer-positive (red) cells identified following expansion using a pool of SF3B1 peptides overlaid on total $CD3^+CD8^+$ (gray) cells. Channels are metal-tagged streptavidin, depicting triple coding tetramer scheme (157-163-164).

3.5 SUPPLEMENTAL FIGURES

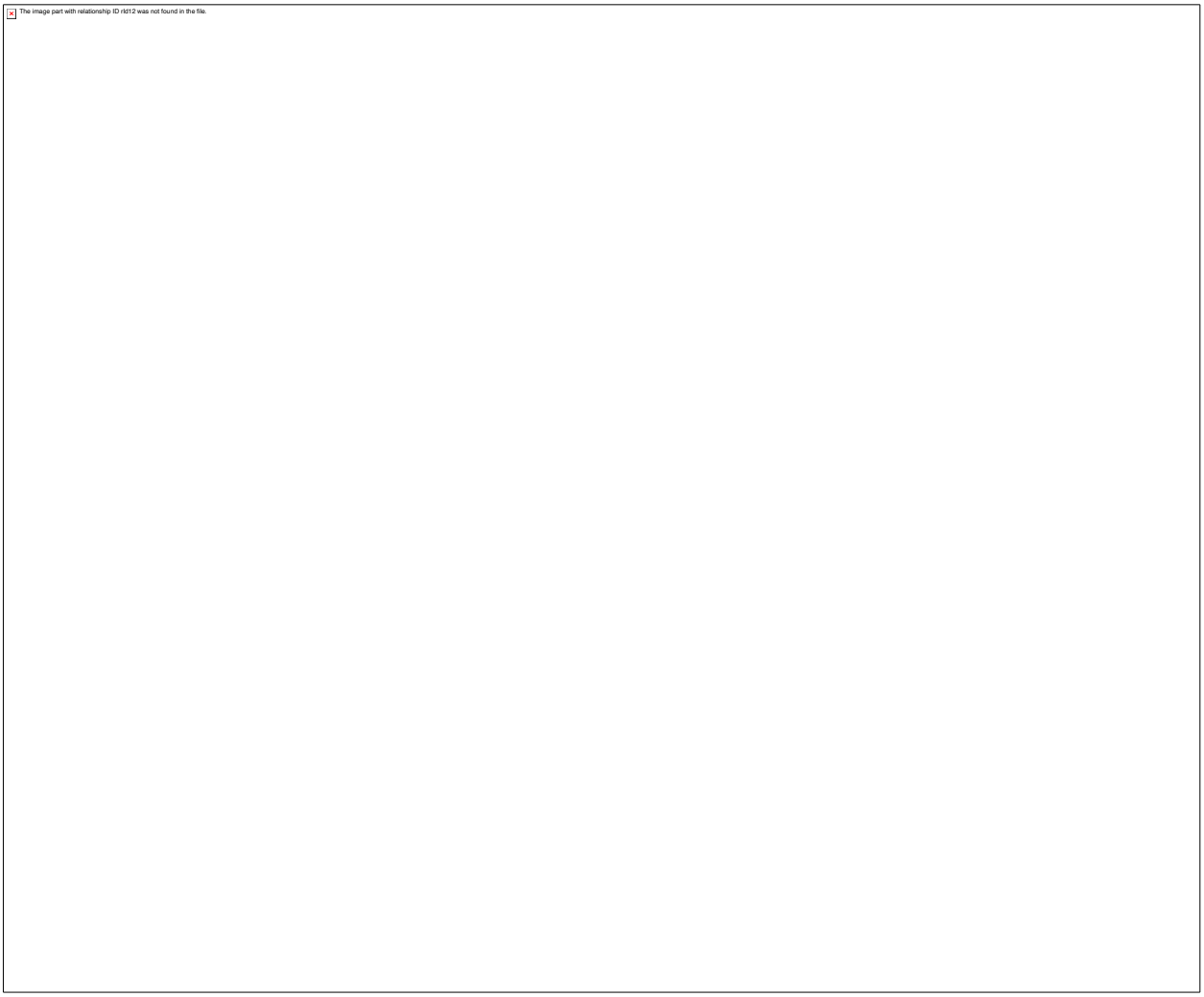

Figure 3.5. Supplementary 1. Gating strategy for $CD3^+CD8^+$ T cells, related to Figure 3.

(A) Gating strategy showing filters used to identify $CD3^+CD8^+$ T cells.

Figure 3.6. Supplementary 2. Antigen-specific expansion, related to Figure 4.

(A) Flow cytometry analysis confirming separation of lymphocytes (left) and differentiation of dendritic cells (right).

(B) Bar graphs depicting percentage of $CD3^{+}CD8^{+}$ cells identified as tetramer-positive after tetramer deconvolution in pre-enriched, anti-c-myc magnetic bead enrichment, and flow-through samples from a donor expansion using all candidate SF3B1 peptides.

3.6 SUPPLEMENTARY TABLES

Table 3.1. Supplementary 1. Metal channel assignment for tetramer and antibody mass cytometry experiment.

Element	Metal	Antibody	Note
Cd	110	CD4	
Cd	111	CD8a	pre-stain
Cd	112	CD14	
Cd	113	CD19	
Cd	114	CD56	
Cd	116	CD33	
Y	89	CD45	
In	115	CD57	
Ce	140	CD34	
Pr	141	CLA	
Nd	142	HLA-DR	
Nd	143	ITB7	
Nd	144	TIGIT	
Nd	145	Granzyme K	intracellular
Nd	146	TCRgd	
Sm	147	CD69	
Nd	148	CD45RO	
Sm	149	CD161	
Nd	150	KLRG1	
Eu	151	CD27	
Sm	152	2B4	
Eu	153	CD103	
Sm	154	CD3	
Gd	155	SAV-1	
Gd	156	CD90	
Gd	157	SAV-2	
Gd	158	CXCR3	pre-stain
Tb	159	SAV-3	
Gd	160	PD-1	pre-stain
Dy	161	SAV-4	
Dy	162	TIM3	
Dy	163	SAV-5	
Dy	164	SAV-6	
Ho	165	CXCR5	pre-stain
Er	166	CD71	
Er	167	SAV-7	
Er	168	CCR7	pre-stain
Tm	169	CD45RA	

Er	170	SAV-8	
Yb	171	CCR5	pre-stain
Yb	172	CD39	
Yb	173	SAV-9	
Yb	174	SAV-10	
Lu	175	Perforin	intracellular
Yb	176	CD38	
Bi	209	CD16	
Ir	191/193	DNA	
Pt	194	CD123	
Pt	195	Cisplatin	
Pt	196	CD99	
Pt	198	CD47	

Table 3.2. Supplementary 2. Peptide-streptavidin codes for combinatorial tetramer staining.

name	code_1	code_2	code_3
A24-DPH5-001	1	2	9
A24-MICAL1-002	1	3	5
A24-OXA1L-003	3	6	8
A24-ARIH1-004	1	6	9
A24-ARIH1-005	5	7	8
A24-ARIH1-006	1	4	5
A24-ARIH1-007	3	7	9
A24-ARIH1-008	4	5	9
A24-ARIH1-009	4	7	9
A24-ARIH1-010	4	6	7
A24-CASD1-011	1	6	8
A24-ERGIC3-012	1	3	4
A24-WRAP73-013	1	2	4
A24-BUB1B-014	3	5	9
A24-GPR108-015	7	8	9
A24-GPR108-016	1	4	10
A24-HSPG2-017	5	6	7
A24-MED13L-018	3	4	8
A24-MED13L-019	5	8	10
A24-MED13L-020	1	5	9
A24-MED13L-021	3	4	6
A24-MED13L-022	2	5	9
A24-MED13L-023	1	3	9
A24-HRSP12-024	7	8	10
A24-HRSP12-025	2	8	10
A24-HRSP12-026	6	7	9
A24-HRSP12-027	7	9	10
A24-HRSP12-028	4	7	8

A24-HRSP12-029	1	5	6
A24-EI24-030	1	5	8
A24-ABCB7-031	2	5	6
A24-ABCB7-032	3	4	9
A24-ABCB7-033	6	9	10
A24-ABCB7-034	2	6	7
A24-HSPG2-035	3	8	10
A24-HSPG2-036	2	3	7
A24-HSPG2-037	3	4	5
A24-HSPG2-038	1	6	7
A24-HSPG2-039	1	4	9
A24-HSPG2-040	2	5	7
A24-HSPG2-041	4	5	7
A24-SHKBP1-042	3	6	10
A24-SHKBP1-043	8	9	10
A24-SHKBP1-044	1	7	8
A24-SHKBP1-045	2	4	6
A24-CAAP1-046	2	3	5
A24-CAAP1-047	1	8	10
A24-CAAP1-048	1	3	8
A24-CAAP1-049	3	4	10
A24-CAAP1-050	1	7	10
A24-ARFGAP2-051	1	3	7
A24-HSPG2-052	2	6	10
A24-CHTF18-053	4	6	9
A24-CHTF18-054	2	7	10
A24-CHTF18-055	3	5	10
A24-CHTF18-056	2	4	5
A24-CSNK1E-057	5	6	8
A24-CSNK1E-058	1	6	10
A24-CSNK1E-059	3	6	7
A02-DPH5-060	4	5	6
A02-MICAL1-061	2	4	8
A02-MICAL1-062	1	9	10
A02-OXA1L-063	1	3	10
A02-OXA1L-064	1	8	9
A02-ARIH1-065	1	4	6
A02-ERGIC3-066	2	3	8
A02-BUB1B-067	3	5	7
A02-HSPG2-068	5	6	10

A02-HSPG2-069	2	3	10
A02-HSPG2-070	5	9	10
A02-HRSP12-071	6	8	9
A02-EI24-072	1	2	10
A02-ABCB7-073	4	9	10
A02-ABCB7-074	6	7	10
A02-ABCB7-075	2	3	6
A02-ABCB7-076	1	7	9
A02-ABCB7-077	4	7	10
A02-ABCB7-078	5	8	9
A02-ABCB7-079	3	7	10
A02-HSPG2-080	1	2	3
A02-HSPG2-081	5	6	9
A02-HSPG2-082	1	3	6
A02-HSPG2-083	2	4	10
A02-HSPG2-084	1	2	7
A02-HSPG2-085	3	6	9
A02-HSPG2-086	2	6	8
A02-HSPG2-087	3	5	8
A02-SHKBP1-088	4	6	10
A02-SHKBP1-089	2	4	7
A02-SHKBP1-090	1	2	8
A02-SHKBP1-091	3	7	8
A02-SHKBP1-092	4	5	10
A02-CAAP1-093	2	8	9
A02-CSNK1E-094	2	5	8
A02-CSNK1E-095	1	2	5
A02-EBV-5	4	8	10
A02-EBV-11	2	9	10
A02-EBV-8	5	7	9
A02-EBV-4	1	5	7
A02-FLU-22	2	5	10
A02-HCMV-2	2	4	9
A02-HCMV-59	4	6	8
A02-HCMV-13	2	3	4
A02-HCMV-15	1	5	10
A02-HSV-2	4	8	9
A02-HSV-3	3	5	6
A02-HSV-4	6	7	8
A24-EBV-64	1	2	6

A24-EBV-2	1	4	7
A24-EBV-3	3	9	10
A24-EBV-4	2	3	9
A24-FLU-11	2	7	8
A24-FLU-7	3	8	9
A24-HCMV-14	5	7	10
A24-HCMV-15	1	4	8
A24-HCMV-16	6	8	10
A02-K700E-1	2	6	9
A24-HSV-4	4	5	8
A24-HSV-5	3	4	7
A02-K700E-2	2	7	9

Table 3.3. Supplementary 3. Antibody information for flow cytometry analysis of lymphocytes and moDCs.

Marker	Fluorophore	Channel	Ab Clone	Ab manufacturer	Lineage
CD11c	Pacific Blue	BV-421 A	3.9	Biolegend	DCs
CD14	APC/Fire 750	APC-Cy7-A	M5E2	Biolegend	Monocytes, macrophages, some DCs
CD20	Brilliant Violet 510	BV-510 A	2H7	Biolegend	B cells
CD3	Brilliant Violet 650	BV-650 A	UCHT1	Biolegend	T cells
CD8	PE	BYG 584-A	SK1	Biolegend	Cytotoxic T cells
CD4	Alexa Fluor 700	APC-R700-A	RPA-T4	Biolegend	Helper T cells
CD56	FITC	BB515-A	HCD56	Biolegend	NK cells

3.7 METHODS

3.7.1 *Method details*

3.7.1.1 RNA-seq data analysis

RNA-seq analysis was performed as described in Chapter 2.7.3.19 (Lu et al., 2021): Briefly, FASTQ files were mapped using RSEM version 1.2.4 (Li and Dewey, 2011) (modified to call Bowtie) (Langmead et al., 2009) with option '-v 2′) to transcriptome annotations built using transcript information from Ensembl v71.1 (Flicek et al., 2013), UCSC knownGene (Meyer et al., 2013), and MISO v2.0 (Katz et al., 2010). Reads that did not align at this step were then mapped

using TopHat version 2.0.8b (Trapnell et al., 2009) to the human (GRCh37/hg19) genome assemblies, as well as to a database of annotated splice junctions as well as all possible new junctions consisting of linkage between each co-linear annotated 5′ and 3′ splice sites within individual genes. Aligned reads from these two mapping steps were merged to generate final BAM files for all subsequent analyses.

Gene expression estimates were computed using RSEM (performed concordantly with the RNA-seq read mapping procedure described above). Significantly differentially expressed genes were defined as those meeting the follow criteria: minimum expression of 1 transcript per million (TPM); minimum fold-change of 1.5 ($\log_2$ scale); $p \leq 0.05$ (computed using an unpaired, two-sided t test comparing replicate groups for a given treatment and cell line) or a minimum Bayes factor of 100 (computed using Wagenmakers's Bayesian framework (Wagenmakers et al., 2010) for the median of gene expression and associated read counts over replicates for a given treatment and cell line). Splice junction-spanning reads were filtered to require a minimum overhang of 6 nt. MISO v2.0 was used to quantify all expression of isoforms arising from exon skipping (cassette exons), competing 5′ splice site selection, competing 3′ splice site selection, and annotated intron retention. Quantification of constitutive intron retention, where constitutive introns were defined as those whose 5′ and 3′ splice sites were never joined to other splice sites in the knownGene annotation, was calculated as previously described (Hubert et al., 2013) using reads with a minimum of 6 nt overhang in both the exon and intron. Events were considered significantly differentially spliced if they met the following criteria: a minimum of 20 identifying reads (reads which align only to one, but not both, isoforms constituting a given splicing event) in each sample; a minimum of 10% change (absolute scale) in isoform ratio or minimum fold-change of 2 ($\log_2$ scale) in absolute isoform ratio; $p \leq 0.05$ (computed using an unpaired, two-sided t test comparing

replicate groups for a given treatment and cell line) or a minimum Bayes factor of 5 (computed using Wagenmakers's Bayesian framework) (Wagenmakers et al., 2010) for the median of isoform ratios and distinguishing read counts over replicates for a given treatment and cell line). All data parsing, statistical analyses, and data visualization were performed using the R programming environment with Bioconductor (Huber et al., 2015).

3.7.1.2 Proteome creation

Two comprehensive alternative splicing proteomes restricted to only predicted binders were created as described in Chapter 1 (Lu et al., 2021). In brief, transcript annotations were combined with RefSeq annotations of the human genome. Isoforms were computationally translated into proteins and digested into unique 8-14mers. All 8-14mers were then analyzed using NetMHCpan v4.0 (Jurtz et al., 2017) to predict binding affinity to HLA-A*02:01 and HLA-A*24:02, and restricted to those with a binding affinity rank < 2.

3.7.1.3 Candidate neoepitope identification

Candidate neoepitopes were identified by combining predicted binders (rank < 2) with the splicing and gene expression information collected from the RNA-seq as described in the text. Using seven MDS and/or AML patient cohorts, a median dpsi was calculated (with removal of missing data). Peptides were required to be 1) less than 11 amino acids long, 2) from genes expressed > 10 TPM, 3) have a dpsi of at least 0.1 in at least one cohort, 4) have a median dpsi across cohorts of at least 0.05, and 5) be specific to the mutant-favored isoform. By additionally analyzing data from the Illumina Body Map and normal bone marrow samples (Madan et al. 2015), peptides were further required to be from an isoform with less than 0.1 psi in all healthy tissues.

3.7.1.4 MHC I immunoprecipitation, peptide purification, and mass spectrometry

Mono-allelic MHC-K562 cell lines were created and peptide-MHC complexes were isolated as previously described (Abelin et al., 2017). After washing with lysis buffer twice, 10mM Tris pH 8 twice, and dH_2O twice, the peptides were desalted on C18 StaGE tips (Ishihama et al., 2006) (Pierce, Cat. 87784) and eluted using a 20%–35%-50% acetonitrile stepwise gradient. Eluted fractions were dried using a SpeedVac vacuum concentrator and stored until mass spectrometry.

3.7.1.5 Mass spectrometry

Mass spectrometry was performed as described in Chapter 2.7.3.21 (Lu et al., 2021): Desalted, dried samples enriched for MHC peptides were resolubilized in 8uL 0.1% TFA and 3uL were loaded onto a packed-in-emitter 12cm/75um ID/3um C18 particles column (Nikkyo Technos Co., Ltd. Japan). Peptides were eluted using a gradient delivered at 300nL/min increasing from 2% Buffer B (0.1% formic acid in 80% acetonitrile) / 99% Buffer A (0.1% formic acid) to 30% Buffer B / 70% Buffer A, over 70 minutes (EasyLC 1200, Thermo Scientific). All solvents were LCMS grade (Optima, Fisher Scientific). MS and MS/MS (HCD type fragmentation) experiments were performed in data dependent mode with lock mass (m/z 445.12003) using Fusion Lumos (Thermo Scientific). Precursor mass spectra were recorded from m/z 300-1500 m/z range at 60,000 resolution. 1, 2 and 3 positive charges were selected for fragmentation experiments. MS/MS spectra were recorded at 30,000 resolution and lowest mass set at m/z 110. For MS/MS acquisition, injection time was set to maximum 100 ms with an Auto Gain Control setting of 5e4. Normalized collision energy was set to 30. All experiments were recorded in FT-mode.

3.7.1.6 Mass spectrometry analysis

Peptide identification was performed as described in Chapter 2.7.3.23 (Lu et al., 2021): Mass spectra from all MHC immunoprecipitations were analyzed using Proteome Discoverer v2.4.1.15, with the following workflow. Spectra from each replicate were searched against the corresponding allele-matched proteome. Searches were performed with no enzyme specificity, precursor mass tolerance of 10 ppm, and fragment mass tolerance of 0.6 Da. Oxidation (+15.995 Da), phosphorylation (+79.966 Da), and deamidated (+0.984 Da) dynamic modifications were included, in addition to N-terminal glutamate to pyro-glutamate (−17.027 Da). False discovery rate (FDR) estimation was performed computationally using the Percolator software. Peptides reaching the 5% FDR threshold were retained for downstream analyses. Peptides corresponding to subsequences of the sequences in the input proteomes were removed before the identified peptides were used for subsequent analyses.

3.7.1.7 Antibody cocktail preparation

Antibodies were conjugated to corresponding metals as in Supplementary Table 1 according to manufacturers' protocols using 100ug of antibody per reaction. MaxPar DN3 polymers were used for all but the cadmium and platinum metals, which instead use MaxPar MCP9 and no added polymer, respectively. Conjugations were tested and titrated prior to use. Once appropriate dilutions were determined, filtered antibodies were mixed to create "pre-stain" (annotated in Supplementary Table 1, stained alongside tetramers as described below) and standard cocktails and frozen at -80C into single use aliquots until use. Conjugated intracellular antibodies were kept at 4C. Monoisotopic cisplatin-195 was purchased and stored at -20C and used for live/dead staining, in addition to DNA intercalator (Ir-191/193).

3.7.1.8 Peptide synthesis

Peptides were individually custom synthesized by Mimotopes to > 85% purity. Peptides were reconstituted in DMSO at 10 mg/mL and frozen at -20C until use.

3.7.1.9 Tetramer cocktail preparation

The triple coding scheme and tetramer preparation were performed according to the method outlined in Simoni et al. 2019. In brief, biotinylated MHC monomers loaded with UV-cleavable peptides were diluted to 0.1 mg/mL, after which 100 uL of monomer was incubated with 5 uL of the corresponding 1 mM peptide, mixed, and exposed to UV light for 10 minutes to exchange the peptide. The peptide-monomer complex was stored overnight at 4C. Each of the 120 peptide-monomers were assigned three metal-tagged streptavidin (SAV) codes of 10 possible metal-tagged SAVs, conjugated according to manufacturer's protocol and diluted to 50 ug/mL (Supplementary Table 2). A Tecan liquid handling robot was used to prepare the SAV mixtures, and 10uL of each mixture was added to the appropriate peptide-monomer tube and incubated for 10 minutes at room temperature in order to tetramerize. This was repeated two additional times, for a total of 30uL added. Tetramers were then incubated with free biotin for 10 minutes at room temperature. All tetramers were then combined and concentrated to a final volume of 500 uL using a 50 kDa concentrator, and PBS-BSA 0.5% was added to a final volume of 1 mL. The tetramer cocktail was filtered using a 0.1 uM filter and frozen at -80C in individual 50 uL aliquots until use.

3.7.1.10 Staining for CyTOF

Staining was also performed as detailed in Simoni et al. 2019 with slight modifications as noted here. PBMCs were thawed, washed, and stained with the tetramer cocktail and pre-stain antibody cocktail for one hour at room temperature. At this stage, 10% of the sample was set aside as 'pre-enriched'. A Miltenyi anti-c-myc magnetic bead tetramer enrichment was performed according to

manufacturer specifications. Following enrichment, 25% of the collected 'flow-through' was added back to the magnetic-bead bound sample to ensure the sample was large enough for analysis, referred to here as the 'enriched' sample. The remaining 'flow-through' sample was analyzed as well to ensure effectiveness of the bead enrichment. Following further washes and buffer exchange, cells were then stained with monoisotopic cisplatin-195 for 10 minutes on ice. The samples were washed and stained with the surface antibody cocktail for 20 minutes on ice. Samples were washed again and then fixed with a 2% PFA solution overnight at 4C. Prior to collection on CyTOF, cells were washed with permeabilization buffer and stained with the intracellular antibodies diluted in permeabilization buffer for 30 minutes at room temperature. Cells were then washed and stained with 100 uL of 1:2000 DNA intercalator for 15 minutes on ice. After final washes, cells were suspended in Maxpar CAS buffer.

3.7.1.11 Mass cytometry data collection and analysis

Cells were diluted and normalization beads were added to 1% of final volume. Before running, cells were filtered through blue-capped 35um flow tubes. Data was acquired on a Fluidigm Helios CyTOF system using Fluidigm software to create FCS files, at a rate of ~100 cells per second. Files were normalized using Normalizer v0.3 software (Finck et al., 2013), followed by randomization as described previously (Newell et al., 2012) and compensation as described in Chevrier et al., 2018. Data was analyzed using FlowJo v10.8.1. $CD3^{+}CD8^{+}$ T cells were gated as shown in Figure S1 prior to tetramer deconvolution.

3.7.1.12 Antigen-specific T cell expansion

100M PBMCs were thawed in RPMI 10% FBS, 200mM L-glutamine, and 1% penicillin/streptomycin (CTL). Resuspend cells in AIM V media at 12M cells/mL and plated into

6-well plates. Cells were then incubated for 90 minutes at 37C to allow monocytes to settle. Lymphocytes were carefully removed from plates, spun down, counted, and diluted to 2M cells/mL. 10U/mL of IL-2 was added to the lymphocytes before incubating the cells at 37C. New AIM V media with 10 ng/mL of GMCSF and 10 ng/mL of IL-4 was then added to the 6-well plates containing monocytes to facilitate dendritic cell differentiation, and cells were incubated at 37C. After three-four days of incubation, moDCs and lymphocytes were collected. An aliquot of 0.6M lymphocytes and 0.35M moDCs were set aside for staining and confirmation via flow cytometry (see section 3.7.1.13, Figure S2A). moDCs were split into a 1:2:2 ratio and pulsed with 1uM of CMV peptide, viral peptides, or SF3B1 peptides, respectively, and incubated at 37C for at least 2 hours. moDCs were then irradiated at 3500 rad, spun down, and resuspended in fresh CTL. moDCs and lymphocytes were mixed at a 1:45 ratio with 10 ng/mL IL-12, plated in 96 well plates (200 uL per well), and incubated at 37C. 10 IU/mL IL-2 was added via partial media change every 3-4 days until day 10, when 10 ng/mL IL-15 was added. On day 13, cells were switched to media without cytokines to rest for one day before being analyzed on CyTOF on day 14 as described in 3.7.10 and 3.7.11.

3.7.1.13 Lymphocyte and moDC flow cytometry

Lymphocytes and moDCs set aside before co-culture were further split into two. One sample of each remained unstained as a control, and the other sample was stained with 3uL of each antibody (see Supplementary Table 3 for antibody clone and fluorophore information) and incubated covered in foil for 20 minutes at 4C. Following staining, cells were washed and resuspended in FACS buffer and stained with 3uL 7-AAD live/dead stain for a few minutes prior to collection. Data was collected on BD FACSCelesta 3 analyzer and analyzed in FlowJo v10.8.1.

3.8 ACKNOWLEDGEMENTS

I would like to thank Nandita Kumar, Amy Codd, Anthony Cessna, Heeju Ryu, David Glass, and other members of the Newell lab for sharing advice on mass cytometry staining and data analysis, as well as the members of the FHCC flow cytometry core for their assistance in using the CyTOF and flow cytometers. I would additionally like to thank Kyle Woodward for sharing his antigen-specific T cell expansion protocol. The results shown here are in whole or part based upon data generated by the TCGA Research Network: https://www.cancer.gov/tcga. I was supported in part by NIH/NCI (T32 CA009657) and by NHGRI (T32 HG000035).

Chapter 4. DISCUSSION AND FUTURE DIRECTIONS

Taken together, these studies demonstrate the promise of targeting transcriptomic dysregulation in cancer using immunotherapies. Establishing disrupted splicing as a source of neoantigens opens the door to various therapeutic approaches to treat cancers. We demonstrate a method for using clinical-grade splicing disruptors to increase the efficacy of PD-1 checkpoint blockade. Identifying specific neoantigens and/or antigen-specific T cells would also allow for more targeted peptide vaccination or engineered TCR-T cell approaches. Although CAR-T cells have not been used to explicitly target alternative splicing, there is a notable example of splicing as a mechanism of immune escape from anti-CD19 CAR-T cells, where cancers begin to select for an isoform that no longer presents this antigen on the surface of the cells (Sotillo et al., 2015). If by contrast cancer-specific splicing isoforms are presented on the cell surface, they could also be targeted. Although these features are not unique to splicing-derived targets, alternative splicing by nature includes larger stretches of sequences than point mutations, which provides a larger search space for potential targets while having a similar rate of immunogenic peptide discovery. I illustrate this in our analysis of splicing-derived candidates in patients with *SF3B1* mutations, and I hope to identify evidence of these in our ongoing SF3B1 patient phenotyping and tetramer screen.

Beyond the mis-splicing caused by the recurrent mutation of SF3B1 studied here, other forms of endogenous transcriptomic dysregulation are also commonly observed in cancer and could provide a useful source of targets as well. Other splicing factors, such as SRSF2*,* U2AF1, and ZRSR2 are recurrently mutated (Yoshida et al., 2011) in cancers and alter RNA splicing in their distinct manners which merit their own investigations. Additionally, because mutations in these splicing factors, like SF3B1, lead to characteristic disruptions in different types of cancers,

we again have potential for public neoantigens that would be appropriate for many patients. Increased intron retention is seen across cancer types (Dvinge & Bradley, 2015), regardless of mutational status, and intronic MHC peptides have been identified as a potential source for neoantigens previously (Smart et al., 2018). Our study using indisulam treatment to disrupt splicing demonstrates that intron retention errors can in fact be immunogenic and targetable by immunotherapies, which supports these proposals. Other forms of transcriptomic dysregulation, such as alternative polyadenylation (Ren et al., 2022) or posttranscriptional RNA editing (Zhang et al., 2018) are also frequently observed in cancer and could additionally present interesting cancer-specific therapeutic targets.

Finally, although the primary goal of my thesis was to investigate therapeutic approaches that take advantage of the adaptive immune system, splicing disruptions can be targeted by other forms of therapeutics. Antisense oligonucleotides that correct mis-splicing errors have shown promising results in the treatment of disease (Muth 2018), and recently SF3B1-mutation dependent synthetic introns have been designed for use with cancer gene therapy (North et al., 2022). These developments emphasize the utility of targeting splicing disruptions in treating disease, and further motivate understanding the effects of mis-splicing generally. Our work here, along with the rapid development of alternative approaches, furthers our understanding of the splicing disruptions in disease and shows a promising future for clinical translation of splicing-directed therapeutics.

BIBLIOGRAPHY

Abelin, J.G., Keskin, D.B., Sarkizova, S., Hartigan, C.R., Zhang, W., Sidney, J., Stevens, J., Lane, W., Zhang, G.L., Eisenhaure, T.M., et al. (2017). Mass Spectrometry Profiling of HLA-Associated Peptidomes in Mono-allelic Cells Enables More Accurate Epitope Prediction. Immunity *46*, 315–326.

Alsafadi, S., Houy, A., Battistella, A., Popova, T., Wassef, M., Henry, E., et al. (2016). Cancer-associated SF3B1 mutations affect alternative splicing by promoting alternative branchpoint usage. Nature Communications, 7(1), 10615.

Bacher, U., Kohlmann, A., & Haferlach, T. (2015). Mutational profiling in patients with MDS: Ready for every-day use in the clinic? Best Practice & Research Clinical Haematology, 28(1), 32–42.

Bertrand, F., Montfort, A., Marcheteau, E., Imbert, C., Gilhodes, J., Filleron, T., Rochaix, P., Andrieu-Abadie, N., Levade, T., Meyer, N., et al. (2017). TNFa blockade overcomes resistance to anti-PD-1 in experimental melanoma. Nat. Commun. *8*, 2256.

Chan-Penebre, E., Kuplast, K.G., Majer, C.R., Boriack-Sjodin, P.A., Wigle, T.J., Johnston, L.D., Rioux, N., Munchhof, M.J., Jin, L., Jacques, S.L., et al. (2015). A selective inhibitor of PRMT5 with in vivo and in vitro potency in MCL models. Nat. Chem. Biol. *11*, 432–437.

Chevrier, S., Crowell, H.L., Zanotelli, V.R.T., Engler, S., Robinson, M.D., Bodenmiller, B. (2018). Compensation of Signal Spillover in Suspension and Imaging Mass Cytometry. Cell Syst. 6(5):612-620.e5.

Choudhary, G., Pellagatti, A., Agianian, B., Smith, M., Bhagat, T., Gordon-Mitchell, S., et al. (2022) Activation of targetable inflammatory immune signaling is seen in myelodysplastic syndromes with SF3B1 mutations eLife 11:e78136.

Curti, A., Pandolfi, S., Valzasina, B., Aluigi, M., Isidori, A., Ferri, E., et al. (2007). Modulation of tryptophan catabolism by human leukemic cells results in the conversion of CD25 into CD25 T regulatory cells. Blood. 109:2871–7.

De Bruijn, M.L., Schumacher, T.N., Nieland, J.D., Ploegh, H.L., Kast, W.M., and Melief, C.J. (1991). Peptide loading of empty major histocompatibility complex molecules on RMA-S cells allows the induction of primary cytotoxic T lymphocyte responses. Eur. J. Immunol. *21*, 2963–2970.

De Silva, A.D., Boesteanu, A., Song, R., Nagy, N., Harhaj, E., Harding, C.V., and Joyce, S. (1999). Thermolabile H-2Kb molecules expressed by transporter associated with antigen processing-deficient RMA-S cells are occupied by low-affinity peptides. J. Immunol. *163*, 4413–4420.

Dvinge, H., Bradley, R.K. (2015). Widespread intron retention diversifies most cancer transcriptomes. Genome Med 7, 45.

Dvinge, H., Ries, R.E., Ilagan, J.O., Stirewalt, D.L., Meshinchi, S., and Bradley, R.K. (2014). Sample processing obscures cancer-specific alterations in leukemic transcriptomes. Proc. Natl. Acad. Sci. USA *111*, 16802–16807.

Dvinge, H., Kim, E., Abdel-Wahab, O., and Bradley, R.K. (2016). RNA splicing factors as oncoproteins and tumour suppressors. Nat. Rev. Cancer *16*, 413–430.

Eram, M.S., Shen, Y., Szewczyk, M., Wu, H., Senisterra, G., Li, F., Butler, K.V., Kaniskan, H.U., Speed, B.A., Dela Sen˜ a, C., et al. (2016). A Potent, Selective, and Cell-Active Inhibitor of Human Type I Protein Arginine Methyltransferases. ACS Chem. Biol. *11*, 772–781.

Fedoriw, A., Rajapurkar, S.R., O'Brien, S., Gerhart, S.V., Mitchell, L.H., Adams, N.D., Rioux, N., Lingaraj, T., Ribich, S.A., Pappalardi, M.B., et al. (2019). Anti- tumor Activity of the Type I PRMT Inhibitor, GSK3368715, Synergizes with PRMT5 Inhibition through MTAP Loss. Cancer Cell *36*, 100–114.e25.

Flicek, P., Ahmed, I., Amode, M.R., Barrell, D., Beal, K., Brent, S., Carvalho- Silva, D., Clapham, P., Coates, G., Fairley, S., et al. (2013). Ensembl 2013. Nucleic Acids Res. *41*, D48–D55.

Finck, R., Simonds, E.F., Jager, A., Krishnaswamy, S., Sachs, K., Fantl, W., et al. (2013). Normalization of mass cytometry data with bead standards. Cytometry, 83A: 483-494.

Fong, J.Y., Pignata, L., Goy, P.A., Kawabata, K.C., Lee, S.C., Koh, C.M., Musiani, D., Massignani, E., Kotini, A.G., Penson, A., et al. (2019). Therapeutic Targeting of RNA Splicing Catalysis through Inhibition of Protein Arginine Methylation. Cancer Cell *36*, 194–209.e9.

Gómez-Llobell, M., Peleteiro Raíndo, A., Climent Medina, J., Gómez Centurión, I., & Mosquera Orgueira, A. (2022). Immune Checkpoint Inhibitors in Acute Myeloid Leukemia: A Meta-Analysis. Frontiers in Oncology, 12, 1545.

Haferlach, T., Nagata, Y., Grossmann, V., Okuno, Y., Bacher, U., Nagae, G., et al. (2014). Landscape of genetic lesions in 944 patients with myelodysplastic syndromes. Leukemia, 28(2), 241–247.

Han, T., Goralski, M., Gaskill, N., Capota, E., Kim, J., Ting, T.C., Xie, Y., Williams, N.S., and Nijhawan, D. (2017). Anticancer sulfonamides target splicing by inducing RBM39 degradation via recruitment to DCAF15. Science *356*, eaal3755.

Huber, W., Carey, V.J., Gentleman, R., Anders, S., Carlson, M., Carvalho, B.S., Bravo, H.C., Davis, S., Gatto, L., Girke, T., et al. (2015). Orchestrating high- throughput genomic analysis with Bioconductor. Nat. Methods *12*, 115–121.

Hubert, C.G., Bradley, R.K., Ding, Y., Toledo, C.M., Herman, J., Skutt-Kakaria, K., Girard, E.J., Davison, J., Berndt, J., Corrin, P., et al. (2013). Genome-wide RNAi screens in human brain tumor isolates reveal a novel viability requirement for PHF5A. Genes Dev. *27*, 1032–1045.

Hutchinson, J.N., Ensminger, A.W., Clemson, C.M., Lynch, C.R., Lawrence, J.B., and Chess, A. (2007). A screen for nuclear transcripts identifies two linked noncoding RNAs associated with SC35 splicing domains. BMC Genomics *8*, 39.

Inoue, D., Chew, G.L., Liu, B., et al. (2019). Spliceosomal disruption of the non-canonical BAF complex in cancer. Nature *574*, 432–436.

Ishihama, Y., Rappsilber, J., and Mann, M. (2006). Modular stop and go extraction tips with stacked disks for parallel and multidimensional Peptide fractionation in proteomics. J. Proteome Res. *5*, 988–994.

Jan, M., Leventhal, M.J., Morgan, E.A., Wengrod, J.C., Nag, A., Drinan, S.D., et al. (2019). Recurrent genetic HLA loss in AML relapsed after matched unrelated allogeneic hematopoietic cell transplantation. Blood Adv. 23;3(14):2199-2204.

Jayasinghe, R.G., Cao, S., Gao, Q., Wendl, M.C., Vo, N.S., Reynolds, S.M., Zhao, Y., Climente-González, H., Chai, S., Wang, F., et al.; Cancer Genome Atlas Research Network (2018). Systematic Analysis of Splice-Site-Creating Mutations in Cancer. Cell Rep. *23*, 270–281.e3.

Jurtz, V., Paul, S., Andreatta, M., Marcatili, P., Peters, B., and Nielsen, M. (2017). NetMHCpan-4.0: Improved Peptide-MHC Class I Interaction Predictions Integrating Eluted Ligand and Peptide Binding Affinity Data. J. Immunol. *199*, 3360–3368.

Kahles, A., Lehmann, K.V., Toussaint, N.C., Hu¨ser, M., Stark, S.G., Sachsenberg, T., Stegle, O., Kohlbacher, O., Sander, C., and Ra¨tsch, G.; Cancer Genome Atlas Research Network (2018). Comprehensive Analysis of Alternative Splicing Across Tumors from 8,705 Patients. Cancer Cell *34*, 211–224.e6.

Katz, Y., Wang, E.T., Airoldi, E.M., and Burge, C.B. (2010). Analysis and design of RNA sequencing experiments for identifying isoform regulation. Nat. Methods *7*, 1009–1015.

Langmead, B., Trapnell, C., Pop, M., and Salzberg, S.L. (2009). Ultrafast and memory-efficient alignment of short DNA sequences to the human genome. Genome Biol. *10*, R25.

Le, D.T., Durham, J.N., Smith, K.N., Wang, H., Bartlett, B.R., Aulakh, L.K., Lu, S., Kemberling, H., Wilt, C., Luber, B.S., et al. (2017). Mismatch repair deficiency predicts response of solid tumors to PD-1 blockade. Science *357*, 409–413.

Le Dieu, R., Taussig, D.C., Ramsay, A.G., Mitter, R., Miraki-Moud, F., et al. (2009). Peripheral blood T cells in acute myeloid leukemia (AML) patients at diagnosis have abnormal phenotype and genotype and form defective immune synapses with AML blasts. Blood. 114(18):3909-16.

Lee, S.C., Dvinge, H., Kim, E., Cho, H., Micol, J.B., Chung, Y.R., Durham, B.H., Yoshimi, A., Kim, Y.J., Thomas, M., et al. (2016). Modulation of splicing catalysis for therapeutic targeting of leukemia with mutations in genes encoding spliceosomal proteins. Nat. Med. *22*, 672–678.

Lesterhuis, W.J., Salmons, J., Nowak, A.K., Rozali, E.N., Khong, A., Dick, I.M., Harken, J.A., Robinson, B.W., and Lake, R.A. (2013). Synergistic effect of CTLA-4 blockade and cancer chemotherapy in the induction of anti-tumor im- munity. PLoS ONE *8*, e61895.

Li, B., and Dewey, C.N. (2011). RSEM: accurate transcript quantification from RNA-Seq data with or without a reference genome. BMC Bioinformatics *12*, 323.

Li, H., Handsaker, B., Wysoker, A., Fennell, T., Ruan, J., Homer, N., Marth, G., Abecasis, G., and Durbin, R.; 1000 Genome Project Data Processing Subgroup (2009). The Sequence Alignment/Map format and SAMtools. BioInformatics *25*, 2078–2079. https://doi.org/10.1093/bioinformatics/btp352.

Lieu, Y.K., Liu, Z., Ali, A.M., Wei, X., Penson, A., Zhang, J., et al. (2022). Proc Natl Acad Sci USA. 119(1):e2111703119.

Lu, S.X., De Neef, E., Thomas, J.D., Sabio, E., Rousseau, B., Gigoux, M., et al. (2021). Pharmacologic modulation of RNA splicing enhances anti-tumor immunity. Cell. 184:15 4032-4047.

Madan, V., Kanojia, D., Li, J., Okamoto, R., Sato-Otsubo, A., Kohlmann, A., et al. (2015). Aberrant splicing of U12-type introns is the hallmark of ZRSR2 mutant myelodysplastic syndrome. Nat Commun. 6:6042.

Majeti, R., Chao, M.P., Alizadeh, A.A., Pang, W.W., Jaiswal, S., Gibbs, K.D., et al. (2009). CD47 is an adverse prognostic factor and therapeutic antibody target on human acute myeloid leukemia stem cells. Cell. 138:286–99.

Malcovati, L., Papaemmanuil, E., Bowen, D.T., Boultwood, J., Della Porta, M.G., Pascutto, C., et al. (2011). Clinical significance of SF3B1 mutations in myelodysplastic syndromes and myelodysplastic/myeloproliferative neoplasms. Blood. 118(24):6239-46.

Marabelle, A., Fakih, M., Lopez, J., Shah, M., Shapira-Frommer, R., Nakagawa, K., Chung, H.C., Kindler, H.L., Lopez-Martin, J.A., Miller, W.H., Jr., et al. (2020). Association of tumour mutational burden with outcomes in patients with advanced solid tumours treated with

pembrolizumab: prospective biomarker analysis of the multicohort, open-label, phase 2 KEYNOTE-158 study. Lancet Oncol. *21*, 1353–1365.

Meyer, L.R., Zweig, A.S., Hinrichs, A.S., Karolchik, D., Kuhn, R.M., Wong, M., Sloan, C.A., Rosenbloom, K.R., Roe, G., Rhead, B., et al. (2013). The UCSC Genome Browser database: extensions and updates 2013. Nucleic Acids Res. *41*, D64–D69.

Murphy, J.P., Konda, P., Kowalewski, D.J., Schuster, H., Clements, D., Kim, Y., Cohen, A.M., Sharif, T., Nielsen, M., Stevanovic, S., et al. (2017). MHC-I Ligand Discovery Using Targeted Database Searches of Mass Spectrometry Data: Implications for T-Cell Immunotherapies. J. Proteome Res. *16*, 1806–1816.

Musiani, D., Bok, J., Massignani, E., Wu, L., Tabaglio, T., Ippolito, M.R., Cuomo, A., Ozbek, U., Zorgati, H., Ghoshdastider, U., et al. (2019). Proteomics profiling of arginine methylation defines PRMT5 substrate specificity. Sci. Signal. *12*, eaat8388.

Muth CC. ASO Therapy: Hope for Genetic Neurological Diseases. *JAMA.* 2018;319(7):644–646.

Na, I.K., Lu, S.X., Yim, N.L., Goldberg, G.L., Tsai, J., Rao, U., Smith, O.M., King, C.G., Suh, D., Hirschhorn-Cymerman, D., et al. (2010). The cytolytic molecules Fas ligand and TRAIL are required for murine thymic graft-versus-host disease. J. Clin. Invest. *120*, 343–356.

Newell, E.W., Sigal, .N, Bendall, S.C. et al. (2012). Cytometry by time-of-flight shows combinatorial cytokine expression and virus-specific cell niches within a continuum of CD8+ T cell phenotypes. Immunity 36(1):142–152.

Newell, E.W., Sigal, N., Nair, N., Kidd, B.A., Greenberg, H.B., Davis, M.M. (2013). Combinatorial tetramer staining and mass cytometry analysis facilitate T-cell epitope mapping and characterization. Nat Biotechnol. 31(7):623-9.

North, K., Benbarche, S., Liu, B. et al. (2022). Synthetic introns enable splicing factor mutation-dependent targeting of cancer cells. Nat Biotechnol 40, 1103–1113.

O'Donnell, T.J., Rubinsteyn, A., Bonsack, M., Riemer, A.B., Laserson, U., and Hammerbacher, J. (2018). MHCflurry: Open-Source Class I MHC Binding Affinity Prediction. Cell Syst. *7*, 129–132.e4.

Oiseth SJ, Aziz MS. (2017). Cancer immunotherapy: a brief review of the history, possibilities, and challenges ahead. *J Cancer Metastasis Treat* 3:250-61.

Pellagatti, A., Armstrong, R.N., Steeples, V., Sharma, E., Repapi, E., Singh, S., et al. (2018). Impact of spliceosome mutations on RNA splicing in myelodysplasia: dysregulated genes/pathways and clinical associations. *Blood*. 132 (12): 1225–1240.

Ramsey, J.M., Kettyle, L.M.J., Sharpe, D.J., Mulgrew, N.M., Dickson, G.J., Bijl, J.J., et al. (2013). Entinostat Prevents Leukemia Maintenance in a Collaborating Oncogene-Dependent Model of Cytogenetically Normal Acute Myeloid Leukemia. *Stem Cells*. 31(7): 1434–1445.

Ran, F.A., Hsu, P.D., Wright, J., Agarwala, V., Scott, D.A., and Zhang, F. (2013). Genome engineering using the CRISPR-Cas9 system. Nat. Protoc. *8*, 2281–2308.

Ren, X., Zhang, B., Tan, K., Chen, W., & Yang, H. (2022). Pervasive Intronic Polyadenylation Serves as a Potential Source of Cancer Neoantigens. Pre-print. doi: 10.21203/rs.3.rs-1537870/v1.

Ritz, C., Baty, F., Streibig, J.C., and Gerhard, D. (2015). Dose-Response Analysis Using R. PLoS ONE *10*, e0146021.

Ross, P., Holmes, J.C., Gojanovich, G.S., and Hess, P.R. (2012). A cell-based MHC stabilization assay for the detection of peptide binding to the canine classical class I molecule, DLA-88. Vet. Immunol. Immunopathol. *150*, 206–212.

Schinke, C., Giricz, O., Li, W., Shastri, A., Gordon, S., Barreyro, L., et al. (2015). IL8-CXCR2 pathway inhibition as a therapeutic strategy against MDS and AML stem cells. *Blood.* 125 (20): 3144–3152.

Schuster, H., Shao, W., Weiss, T., Pedrioli, P.G.A., Roth, P., Weller, M., Camp- bell, D.S., Deutsch, E.W., Moritz, R.L., Planz, O., et al. (2018). A tissue-based draft map of the murine MHC class I immunopeptidome. Sci. Data *5*, 180157.

Scotti, M., Swanson, M. (2016). RNA mis-splicing in disease. *Nat Rev Genet* **17**, 19–32.

Seiler, M., Yoshimi, A., Darman, R., Chan, B., Keaney, G., Thomas, M., Agrawal, A.A., Caleb, B., Csibi, A., Sean, E., et al. (2018). H3B-8800, an orally available small-molecule splicing modulator, induces lethality in spliceosome- mutant cancers. Nat. Med. *24*, 497–504.

Sellin, M., Mack, R., Rhodes, M.C., Zhang, L., Wei, W., Breslin, P., Berg, S., Huang, S., Taylor, R., and Zhang, J. (2019). The Splicing Modulator GEX1A Exhibits Potent Anti-Leukemic Activity Both in Vitro and In Vivo through Inducing an MCL1 Splice-Switch in Pre-Clinical Models of Acute Myeloid Leukemia. Blood *134*, 2666.

Sha, D., Jin, Z., Budczies, J., Kluck, K., Stenzinger, A., and Sinicrope, F.A. (2020). Tumor Mutational Burden as a Predictive Biomarker in Solid Tumors. Cancer Discov. *10*, 1808–1825.

Simoni, Y., Fehlings, M., Newell, E.W. (2019). Multiplex MHC Class I Tetramer Combined with Intranuclear Staining by Mass Cytometry. Methods Mol Biol. 1989:147-158.

Smart, A.C., Margolis, C.A., Pimentel, H., He, M.X., Miao, D., Adeegbe, D., Fugmann, T., Wong, K.K., and Van Allen, E.M. (2018). Intron retention is a source of neoepitopes in cancer. Nat. Biotechnol. *36*, 1056–1058.

Sotillo, E., Barrett, D.M., Black, K.L., Bagashev, A., Oldridge, D., Wu, G., et al. (2015). Convergence of Acquired Mutations and Alternative Splicing of *CD19* Enables Resistance to CART-19 Immunotherapy. *Cancer Discov.* 5 (12): 1282–1295.

Thomas, J.D., Polaski, J.T., Feng, Q., De Neef, E.J., Hoppe, E.R., McSharry, M.V., Pangallo, J., Gabel, A.M., Belleville, A.E., Watson, J., et al. (2020). RNA isoform screens uncover the essentiality and tumor-suppressor activity of ultraconserved poison exons. Nat. Genet. *52*, 84–94.

Toffalori, C., Zito, L., Gambacorta, V., Riba, M., Oliveira, G., Bucci, G., et al. (2019). Immune signature drives leukemia escape and relapse after hematopoietic cell transplantation. Nat Med. 25(4):603-611.

Trapnell, C., Pachter, L., and Salzberg, S.L. (2009). TopHat: discovering splice junctions with RNA-Seq. Bioinformatics *25*, 1105–1111.

Tyner, J.W., Tognon, C.E., Bottomly, D., Wilmot, B., Kurtz, S.E., Savage, S.L., et al. (2018). Functional genomic landscape of acute myeloid leukaemia. Nature. 562(7728):526-531.

Wagenmakers, E.J., Lodewyckx, T., Kuriyal, H., and Grasman, R. (2010). Bayesian hypothesis testing for psychologists: a tutorial on the Savage-Dickey method. Cognit. Psychol. 60, 158–189.

Wang, E., Lu, S.X., Pastore, A., Chen, X., Imig, J., Chun-Wei Lee, S., Hockemeyer, K., Ghebrechristos, Y.E., Yoshimi, A., Inoue, D., et al. (2019). Targeting an RNA-Binding Protein Network in Acute Myeloid Leukemia. Cancer Cell *35*, 369–384.e7.

Wells, D.K., van Buuren, M.M., Dang, K.K., Hubbard-Lucey, V.M., Sheehan, K.C.F., Campbell, K.M., Lamb, A., Ward, J.P., Sidney, J., Blazquez, A.B., et al.; Tumor Neoantigen Selection Alliance (2020). Key Parameters of Tumor Epitope Immunogenicity Revealed Through a Consortium Approach Improve Neoantigen Prediction. Cell *183*, 818–834.e13.

van der Werf, I., Wojtuszkiewicz, A., Meggendorfer, M., Hutter, S., Baer, C., Heymans, M., et al. (2021). Splicing factor gene mutations in acute myeloid leukemia offer additive value if incorporated in current risk classification. Blood Adv. 5(17):3254-3265.

Wickham, H., Averick, M., Bryan, J., Chang, W., D'Agostino McGowan, L., Francois, R., Grolemund, G., Hayes, A., Henry, L., Hester, J., et al. (2019). Welcome to the Tidyverse. The Journal of Open Source Software. https:// doi.org/10.21105/joss.01686.

Yadav, M., Jhunjhunwala, S., Phung, Q.T., Lupardus, P., Tanguay, J., Bum- baca, S., Franci, C., Cheung, T.K., Fritsche, J., Weinschenk, T., et al. (2014). Predicting immunogenic tumour mutations by combining mass spectrometry and exome sequencing. Nature *515*, 572–576.

Yokoi, A., Kotake, Y., Takahashi, K., Kadowaki, T., Matsumoto, Y., Minoshima, Y., Sugi, N.H., Sagane, K., Hamaguchi, M., Iwata, M., and Mizui, Y. (2011). Biological validation that SF3b is a target of the antitumor macrolide pladienolide. FEBS J. *278*, 4870–4880.

Yoshida, K., Sanada, M., Shiraishi, Y., Nowak, D., Nagata, Y., Yamamoto, R., et al. (2011). Frequent pathway mutations of splicing machinery in myelodysplasia. Nature. 478(7367):64-9.

Zhang, M., Fritsche, J., Roszik, J. et al. (2018). RNA editing derived epitopes function as cancer antigens to elicit immune responses. Nat Commun 9, 3919.

Zhang, Y., Zhang, Z. (2020). The history and advances in cancer immunotherapy: understanding the characteristics of tumor-infiltrating immune cells and their therapeutic implications. *Cell Mol Immunol* **17**, 807–821.

Zhou, Z., Luo, M.J., Straesser, K., Katahira, J., Hurt, E., and Reed, R. (2000). The protein Aly links pre-messenger-RNA splicing to nuclear export in metazoans. Nature *407*, 401–405.